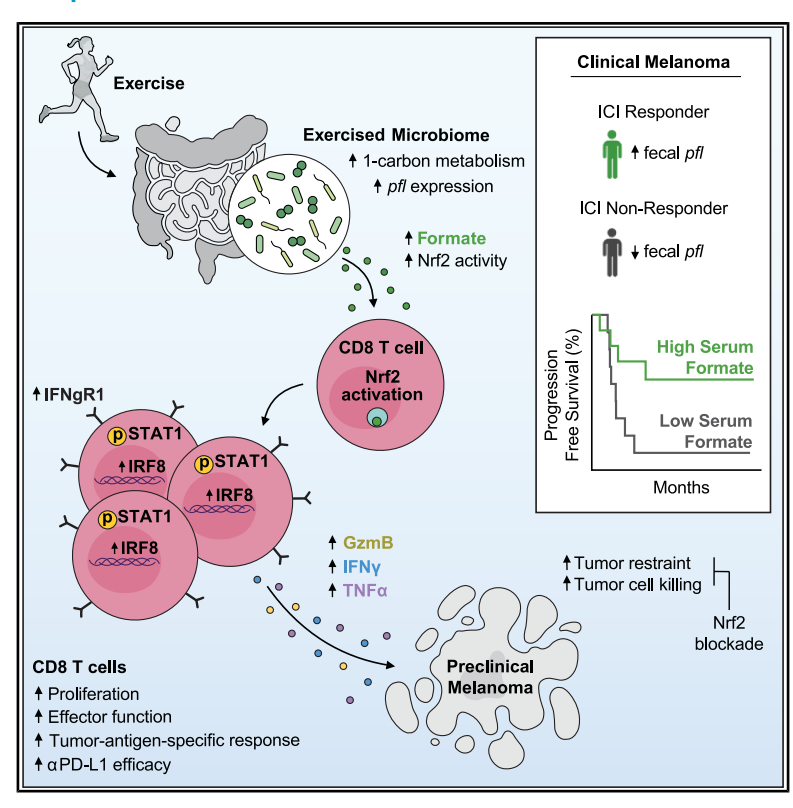


Exercise-induced microbiota metabolite enhances CD8 T cell antitumor immunity promoting immunotherapy efficacy

Graphical abstract



Authors

Catherine M. Phelps, Nathaniel B. Willis, Tingting Duan, ..., Joseph F. Pierre, Giorgio Trinchieri, Marlies Meisel

Correspondence

marlies@pitt.edu

In brief

Exercise enhances antitumor immunity and immunotherapy effectiveness by increasing microbiota-derived formate, which boosts CD8 T cell function and may serve as a biomarker of melanoma suppression.

Highlights

- Exercise-induced microbial formate enhances immune checkpoint inhibitor efficacy
- Microbiota-derived formate is essential for the exercisemediated antitumor effect
- Formate boosts antitumor immunity via nuclear factor erythroid 2-related factor-2
- High-formate-producing human gut microbiota enhances antitumor CD8 T cell immunity









Article

Exercise-induced microbiota metabolite enhances CD8 T cell antitumor immunity promoting immunotherapy efficacy

Catherine M. Phelps, ^{1,2} Nathaniel B. Willis, ³ Tingting Duan, ¹ Amanda H. Lee, ^{1,2} Yue Zhang, ^{1,4} Daphne M. Rodriguez J, ¹ Surya P. Pandey, ¹ Colin R. Laughlin, ¹ Aaron B.I. Rosen, ^{5,6} Alex C. McPherson, ^{1,7} Jake H. Shapira, ¹ Simran K. Randhawa, ¹ Lee Hedden, ¹ Tanner G. Richie, ⁸ Hallie M. Wiechman, ⁸ Mackenzie J. Bender, ¹ Ina Nemet, ^{9,10} Patrick A. Zöhrer, ^{11,12} Rachel A. Gottschalk, ^{1,5} Kathryn H. Schmitz, ¹³ Steven J. Mullett, ^{14,15} Stacy L. Gelhaus, ^{14,15} Diwakar Davar, ^{13,16} Hassane M. Zarour, ^{1,13,16} Reinhard Hinterleitner, ^{1,16,17} Thomas Mossington, ¹⁸ Jonathan H. Badger, ¹⁸ Richard R. Rodrigues, ^{18,19} John A. McCulloch, ¹⁸ Sonny T.M. Lee, ⁸ Karl-Heinz Wagner, ^{11,20} Maria G. Winter, ²¹ Sebastian E. Winter, ²¹ Jishnu Das, ^{1,5} Joseph F. Pierre, ^{3,22} Giorgio Trinchieri, ^{18,23} and Marlies Meisel ^{1,16,24,*} ¹Department of Immunology, University of Pittsburgh School of Medicine, Pittsburgh, PA, USA

SUMMARY

Exercise improves immune checkpoint inhibitor (ICI) efficacy in cancers such as melanoma; however, the mechanisms through which exercise mediates this antitumor effect remain obscure. Here, we identify that the gut microbiota plays a critical role in how exercise improves ICI efficacy in preclinical melanoma. Our study demonstrates that exercise stimulates microbial one-carbon metabolism, increasing levels of the metabolite formate, which subsequently enhances cytotoxic CD8 T cell (Tc1)-mediated ICI efficacy. We further establish that microbiota-derived formate is both sufficient and required to enhance Tc1 cell fate *in vitro* and promote tumor antigen-specific Tc1 immunity *in vivo*. Mechanistically, we identify the transcription factor nuclear factor erythroid 2-related factor 2 (Nrf2) as a crucial mediator of formate-driven Tc1 function enhancement *in vitro* and a key player in the exercise-mediated antitumor effect *in vivo*. Finally, we uncover human microbiota-derived formate as a potential biomarker of enhanced Tc1-mediated antitumor immunity, supporting its functional role in melanoma suppression.



²Graduate Program of Microbiology and Immunology, University of Pittsburgh School of Medicine, Pittsburgh, PA, USA

³Department of Nutritional Sciences, University of Wisconsin-Madison, Madison, WI, USA

⁴Tsinghua Medicine, School of Medicine, Tsinghua University, Beijing, China

⁵Center for Systems Immunology, University of Pittsburgh School of Medicine, Pittsburgh, PA, USA

⁶Joint CMU-Pitt PhD Program in Computational Biology, Carnegie Mellon–University of Pittsburgh, Pittsburgh, PA, USA

⁷Department of Infectious Diseases and Microbiology, University of Pittsburgh School of Public Health, Pittsburgh, PA, USA

⁸Division of Biology, Kansas State University, Manhattan, KS, USA

⁹Department of Cardiovascular & Metabolic Sciences, Lerner Research Institute, Cleveland Clinic, Cleveland, OH, USA

¹⁰Center for Microbiome & Human Health, Cleveland Clinic, Cleveland, OH, USA

¹¹Department of Nutritional Sciences, University of Vienna, Vienna, Austria

¹² Vienna Doctoral School of Pharmaceutical, Nutritional and Sport Sciences (PhaNuSpo), University of Vienna, Vienna, Austria

¹³Department of Medicine and UPMC Hillman Cancer Center, University of Pittsburgh, Pittsburgh, PA, USA

¹⁴Department of Pharmacology and Chemical Biology, University of Pittsburgh School of Medicine, Pittsburgh, PA, USA

¹⁵Health Sciences Mass Spectrometry Core, University of Pittsburgh, Pittsburgh, PA, USA

¹⁶Cancer Immunology and Immunotherapy Program, UPMC Hillman Cancer Center, Pittsburgh, PA, USA

¹⁷Institute of Infection, Inflammation, and Immunity, UPMC Children's Hospital of Pittsburgh, Pittsburgh, PA, USA

¹⁸Genetics and Microbiome Core, Laboratory of Integrative Cancer Immunology, Center for Cancer Research, National Cancer Institute, Bethesda, MD, USA

¹⁹Basic Science Program, Frederick National Laboratory for Cancer Research, Frederick, MD, USA

²⁰Research Platform Active Ageing, University of Vienna, Vienna, Austria

²¹Department of Internal Medicine, Division of Infectious Diseases, University of California, Davis, Davis, CA, USA

²²Department of Surgery, University of Wisconsin-Madison, Madison, WI, USA

²³Laboratory of Integrative Cancer Immunology, Center for Cancer Research, National Cancer Institute, Bethesda, MD, USA

²⁴Lead contact

^{*}Correspondence: marlies@pitt.edu https://doi.org/10.1016/j.cell.2025.06.018





INTRODUCTION

A sedentary lifestyle is a leading risk factor for cancer. Exercise reduces cancer risk, prolongs survival, and improves therapy efficacy,²⁻⁴ leading to its recommendation as standard of care treatment.⁵⁻⁷ Exercise restrains tumor growth⁵ and enhances immune checkpoint inhibitor (ICI) efficacy in various preclinical cancer models, 8-13 yet the underlying mechanisms remain poorly understood, especially in melanoma. Observational studies show exercise alters gut microbiome composition in mice¹⁴ and humans.¹⁵⁻¹⁸ Gut microbiome changes triggered by environmental factors, such as probiotics, 19,20 antibiotics (ABX),²¹ and diet,^{20,22} critically affect cancer etiopathogenesis in mice and humans. 15 However, whether exercise-induced microbiome changes play a role in the ability of exercise to promote antitumor immunity has never been tested before. Pursuing links between exercise, the microbiota, and antitumor immunity in preclinical melanoma, we discovered a mechanism of how exercise exerts its antitumor function and improves ICI efficacy via induction of a microbiota metabolite.

RESULTS

Deployment of a translationally relevant model of exercise-mediated melanoma tumor growth restraint

To interrogate the role of the microbiota in exercise-mediated antitumor effects in melanoma, we first established a treadmill running exercise regimen allowing control over distance, duration, intensity, and frequency of exercise (Figures S1A-S1C). We used a subcutaneously engrafted BRAFV600E melanoma model, which is clinically relevant and ICI resistant. 23,24 We tested the antitumor potential of our exercise regimen in specific pathogen-free (SPF) wild-type (WT) mice. In the prolonged exercise setting, the exercised cohort underwent a 1-week acclimation period, followed by 4 weeks of exercise prior to tumor cell engraftment (TCE). The exercise regimen was slightly reduced in intensity post-TCE until endpoint analysis (EPA) (Figures S1B and S1C). To control for environmental stressors, 25 sham control-treated (referred to as "sedentary") mice were placed adjacent to the treadmill, ensuring similar environmental stimuli as exercised mice (Figure S1A). Prolonged exercise significantly restrained tumor outgrowth (Figure S1D). Both an interventional exercise regimen (post-TCE) (Figure S1E) and a prophylactic regimen (pre-TCE) significantly restrained tumor growth and prolonged survival of BRAFV600E melanoma tumor bearers (Figure S1F). To control for treadmill-associated stressors, we implemented a voluntary exercise regimen using electronically monitored running wheels. Exercised mice were single-housed with wheel access, while sedentary controls were single-housed with a hut for environmental enrichment (Figure S1B). We found that voluntary wheel running significantly restrained tumor growth (Figure S1G), confirming tumor suppression was independent of treadmill-associated stress.

Consistent with previous studies highlighting the antitumor potential of exercise across distinct preclinical cancer models, ^{5,10,13,26} exercise restrained tumor growth and prolonged survival in B16-F10 melanoma compared with sedentary controls (Figure S1H). Endurance exercise did not affect body

weight (Figure S1I), implying tumor growth effects were independent of body weight changes.

In BRAF^{V600E} melanoma, exercise significantly increased programmed cell death protein 1 (PD-1)-expressing and effector cytokine-producing CD8 and CD4 T cells in tumor-draining lymph nodes (tdLNs) (Figures S2A and S2B). While exercise robustly increased interferon-γ (IFNγ) production of tumor-infiltrating CD4 T cells, it failed to elevate the total abundance of infiltrated CD8 and CD4 T cells (Figures S2C-S2E). This implied exercise functionally enhanced CD4 and CD8 T cells, particularly in tdLN, a critical location for improving ICI efficacy. 27-29 Exercise treatment failed to majorly impact Foxp3 regulatory T cells (Tregs) within either the tdLN or tumor microenvironment (TME) (Figure S2F). Exercise has been found to restrain B16 melanoma growth via natural killer (NK) cells. 13 In our model, exercise failed to impact the frequency of innate immune and other T cell populations in the tdLN and TME, including myeloid-derived suppressor cells, dendritic cells, NK cells, and $\gamma\delta$ T cells (Figures S2G and S2H). While exercise significantly affected macrophages and NK T cells (Figures S2G and S2H), its inability to restrain BRAF^{V600E} melanoma growth in Rag^{-/-} mice (Figure S2I) suggested that exercise-induced changes in innate immune cells are insufficient to independently restrain tumor growth, indicating adaptive immunity supports the exercisemediated antitumor effect. To further interrogate cellular drivers, CD4 and CD8 T cells were depleted in BRAF^{V600E} tumor-bearing exercised mice, revealing exercise still potently suppressed tumor growth in the absence of CD4 T cells, similar to isotype control-treated mice. However, exercise treatment was ineffective once CD8 T cells were depleted (Figure S2J), identifying CD8 T cells as critical mediators of exercise-induced antitumor effects. While exercise enhanced T cell responses in cancer, it did not globally enhance systemic T cell immunity during homeostasis (Figures S2K and S2L).

Taken together, we established a model of exercise-induced cytotoxic CD8 T cell (Tc1)-driven tumor growth restraint using a translationally relevant ICI-resistant melanoma model.

The gut microbiota mediates the exercise-induced antitumor effect in BRAF^{V600E} melanoma

Given evidence that exercise alters the gut microbiota ^{14–18} and the fact that the gut microbiota plays a critical role in antitumor immunity, ³⁰ we next examined whether the microbiota contributes to the exercise-induced antitumor effects in our model. We performed 16S rRNA amplicon sequencing (16S seq) on feces from non-tumor-bearing WT mice after 5 weeks of exercise or sedentary treatment (Figure 1A). Exercise significantly altered gut microbiota community composition (Figure 1B), notably expanding an unclassified *Erysipelotrichaceae* genus and *Monoglobus* (Oscillospiraceae) (Figures 1C, S3A, and S3B). Sedentary conditions showed relative increases in *Dubosiella* (*Erysipelotrichaceae*), *Bifidobacterium* (*Bifidobacteriaceae*), an unclassified *Ruminococcaceae* genus, and *Lachnospiraceae A2* (*Lachnospiraceae*) (Figures 1C, S3A, and S3B).

To establish causality, we performed fecal microbial transplantations (FMTs) into ABX-pretreated mice¹⁹ using feces from exercised (referred to as "FMT-EX") and sedentary (referred to as "FMT-SED") donors before BRAF^{V600E} TCE





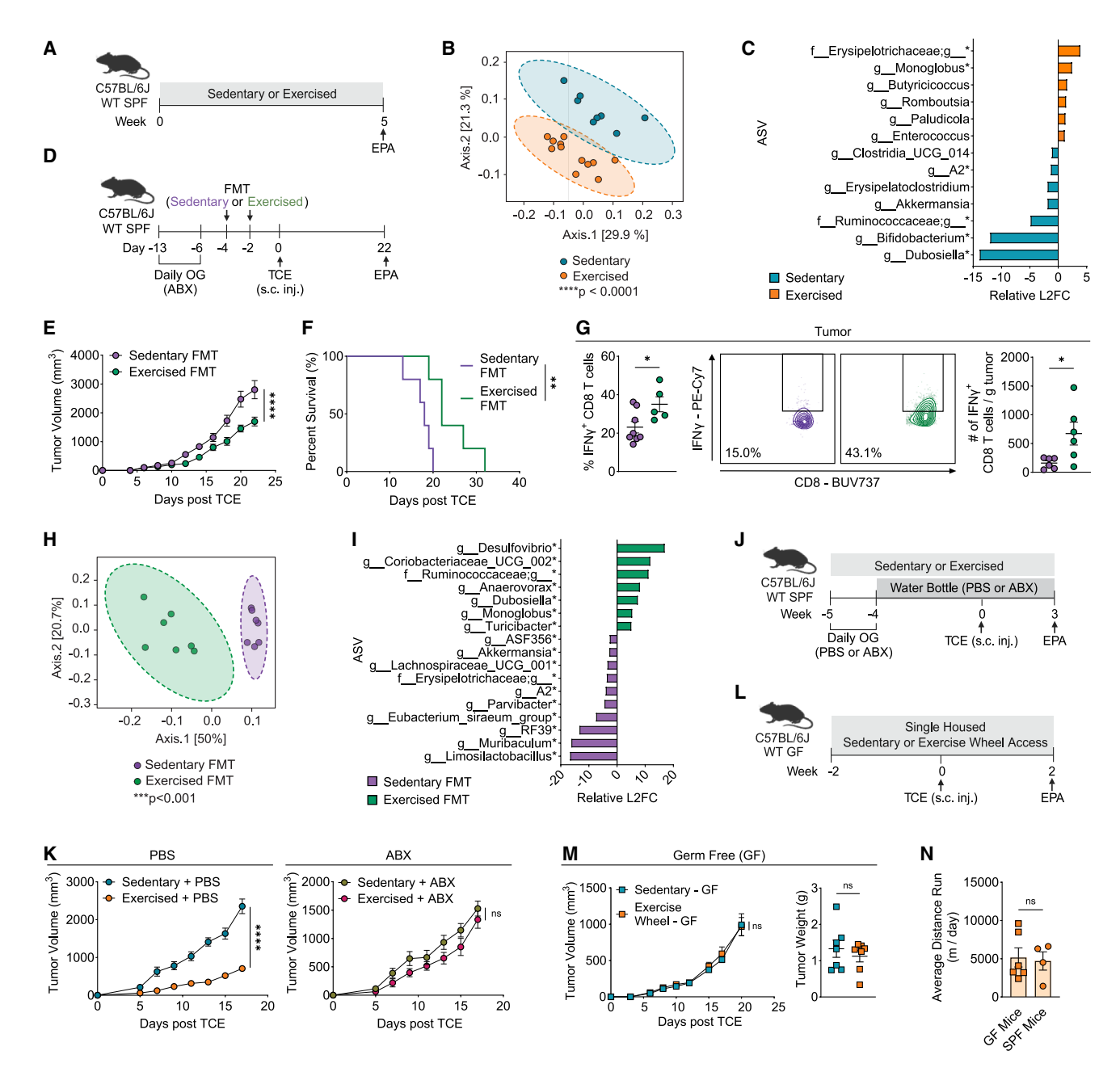


Figure 1. The gut microbiota is required and sufficient for the exercise-induced antitumor effect in BRAF^{V600E} melanoma

(A–C) 16S seq of feces (n = 8–12 mice/group). (A) Experimental outline for (B) and (C). (B) Principal-component analysis (PCA) plot. (C) Genus-level differential abundance of amplicon sequence variants (ASVs).

- (D) Experimental outline for (E)–(I). Mice received broad-spectrum antibiotics (ABX) followed by exercised or sedentary FMT and BRAF V600E TCE (n = 5-8 mice/group).
- (E) Tumor growth.
- (F) Survival.
- (G) Tumor-infiltrating IFNγ⁺ CD8 T cell frequency (left), representative plots (middle), and cells per g tumor (right).
- (H and I) 16S seq of cecum. (H) PCA plot. (I) Genus-level differential abundance of ASVs.
- (J) Experimental outline of (K). Exercised or sedentary mice were maintained on ABX before and after BRAF V600E TCE (n = 6-8 mice/group).
- (K) Tumor growth
- (L) Experimental outline for (M) and (N). Germ-free (GF) mice underwent a voluntary running regimen and BRAF^{V600E} TCE (n = 8 mice/group).
- (M) Tumor growth.

(legend continued on next page)



(Figure 1D). FMT-EX significantly suppressed tumor growth (Figure 1E), prolonged survival (Figure 1F), and enhanced tumor-intrinsic and systemic Tc1 immunity compared with FMT-SED (Figures 1G, S3C, and S3D). To assess the taxonomic stability post FMT, we performed 16S seq on cecal contents of FMT recipients 3 weeks post FMT and confirmed that FMT-EX and FMT-SED recipients retained compositionally distinct microbiomes (Figure 1H). FMT-EX recipients had relatively enriched Desulfovibrio, Coriobacteriaceae_UCG_002, Dubosiella, and Monoglobus, and reduced Limosilactobacillus, Muribaculum, Lachnospiraceae A2, and an unclassified Erysipelotrichaceae genus (Figures 1I, S3E, and S3F). Key donor taxa like Monoglobus persisted, while Lachnospiraceae A2 remained reduced post FMT.

We next utilized three independent yet complementary approaches to determine if the gut microbiome is required for the exercise-induced antitumor effects: (1) broad-spectrum ABX, (2) co-housing, and (3) germ-free (GF) mice. Mice underwent prolonged exercise or sedentary treatment and received ABX or vehicle control from 5 weeks pre-TCE until EPA (Figure 1J). As anticipated, prolonged exercise potently suppressed tumor growth in vehicle-treated mice (Figure 1K). Intriguingly, prolonged exercise failed to restrain tumor growth in ABX-treated mice (Figure 1K). ABX suppressed bacterial load (Figure S3G) but failed to impact running distance or willingness to run (Figures S3H and S3I). Accordingly, ABX significantly impaired interventional exercise-induced antitumor effects (Figure S3J). In addition, co-housed sedentary and exercised mice showed similar tumor growth, unlike non-co-housed controls (Figure S3K), further supporting the antitumor benefits of exercise-induced microbiome changes.

Finally, we evaluated the impact of exercise on melanoma progression in GF mice. Due to the incompatibility between our treadmill and GF housing, we utilized the voluntary wheel-running regimen, which was previously shown to significantly suppress BRAF^{V600E} melanoma growth in SPF mice (Figures S1B and S1G). Strikingly, in the absence of the microbiota, voluntary exercise failed to restrain BRAF^{V600E} melanoma growth (Figures 1L and 1M). Importantly, this lack of tumor restraint was not attributable to differences in physical activity, as GF mice ran distances similar to SPF mice (~5,000 m/day) (Figures 1N and S3L).

Collectively, using four independent approaches (FMT, ABX, co-housing, and GF), we demonstrated that exercise-induced microbiome changes are both sufficient and required for the antitumor effect in ICI-resistant BRAF^{V600E} melanoma.

Exercise-induced microbiota metabolites restrain melanoma growth via enhanced Tc1 immunity

The gut microbiota modulates systemic tumor immunity via cell wall components³¹ and secreted metabolites.³² To discern whether microbiota metabolites or cell wall components are critical in exercise-induced melanoma restraint, we performed

FMTs using viable or heat-killed feces from sedentary and exercised donors prior to BRAF^{V600E} TCE (Figure 2A). Viable FMT-EX robustly restrained tumor growth compared with viable FMT-SED (Figure 2B), consistent with previous findings (Figures 1E and 1F). Importantly, unlike viable FMT-EX, heat-killed FMT-EX failed to restrain tumor growth, suggesting that exercise-primed bacterial cell wall components alone are insufficient and that microbiota-derived metabolites produced by live bacteria may be essential in driving the exercise-induced antitumor effect (Figure 2B). Tumor growth rates of viable and heat-killed FMT-SED were comparable to autologous-viable FMT, suggesting that heat-killing did not affect the immunogenicity of the transplanted feces (Figure 2B).

Based on this result, we hypothesized that exercise-induced microbiota metabolites play a critical role in exercise-enhanced antitumor Tc1 immunity. Indeed, we found that sterile-filtered exercise microbiota metabolites (referred to as "EX-MM") enhanced Tc1 fate at both protein and transcriptional levels more potently than sedentary microbiota metabolites (referred to as "SED-MM") (Figures 2C-2E). To generate sufficient microbiota metabolites for in vivo treatments, we used a culturomics approach³³ and cultured feces from sedentary and exercised mice under diverse broth conditions (Figure S3M). Oral administration of cultured EX-MM significantly restrained BRAFV600E tumor growth relative to cultured SED-MM and broth control (Figure 2F). Furthermore, EX-MM-treated BRAFV600E-bearing mice showed a significantly increased frequency of IFN_γ- and Granzyme B (GzmB) double-producing CD8 T cells in tdLNs (Figure 2G), supporting the EX-MM antitumor potential.

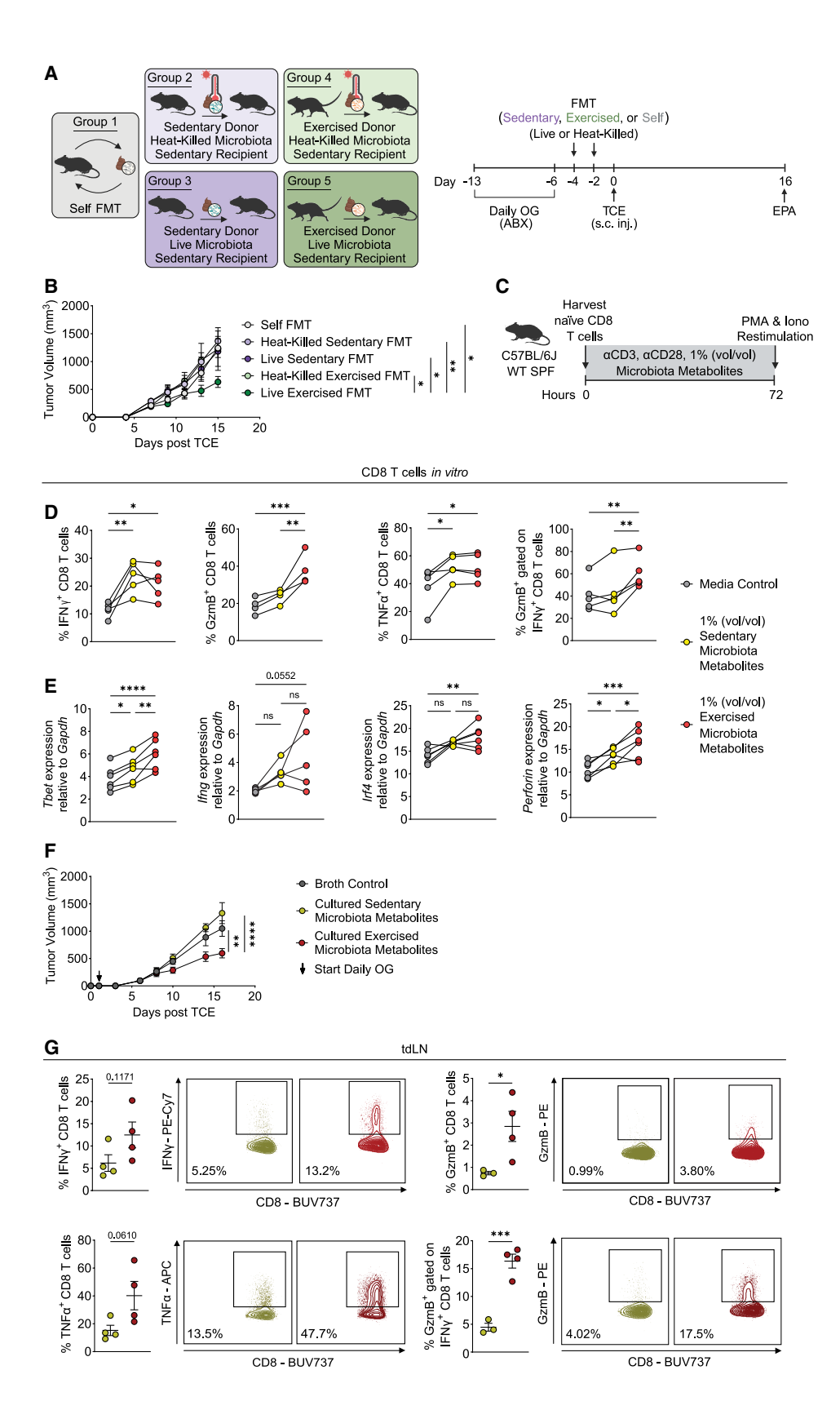
In summary, these observations pointed toward a critical antitumor role of exercise-induced microbiota metabolites.

Exercise promotes functional metabolic changes in the gut microbiome, upregulating the 1C pathway and increasing formate production

To profile exercise-induced global metabolic changes in the gut microbiota, untargeted metabolomics of fecal microbial supernatants from exercised and sedentary mice was performed using high-resolution mass spectroscopy. Analysis of these profiles using an interpretable latent factor regression-based machine learning approach, SLIDE, 34 revealed significant microbial metabolome differences (Figures 3A and 3B; Table S1) and identified four latent factors driving these changes (Figure 3B; Table S1). KEGG analysis of metabolites linked to each latent factor revealed an exercise-induced enrichment in key pathways, including amino acid metabolism, one-carbon (1C) metabolism, bile acid metabolism, folate (vitamin B9) metabolism, antioxidant and xenobiotic pathways, vitamin B metabolism, and tryptophan metabolism (Figure 3C; Table S1). Complementary analysis using the Mummichog algorithm³⁵ (BioCyc library) confirmed an enrichment in bile acid, vitamin B, and amino acid metabolism, prominently highlighting folate-dependent and -independent 1C pathways, including tetrahydrofolate salvage, pyrimidine metabolism, and

(N) Average distance run. (E, K, and M) Mean \pm SEM, two-way ANOVA with Sidak's correction for multiple comparisons. (B and H) PERMANOVA, each dot indicates individual mouse. (C and I) Significantly enriched genera identified by Spearman correlation. (F) Log-rank test. (G, M, and N) Individual mice, unpaired t test. Mean \pm SEM. *p < 0.05, **p < 0.01, ****p < 0.001, ****p < 0.001; ns, not significant. See also Figures S1, S2, and S3.









methionine, tryptophan, and asparagine degradation (Figure 3D; Table S1). 36,37

Subsequently, we rigorously examined the bile acid and the 1C pathway within gut microbiomes from sedentary and exercised animals, as both prior unbiased machine learning and pathway analyses indicated their modulation by exercise. Microbiota-derived bile acids are implicated in antitumor immunity in cancer. 38 Yet, exercise did not significantly alter the microbial abundance of any measured bile acid in our model (Figures S4A and S4B; Table S1). The folate-dependent and -independent 1C pathway supports biochemical processes that promote essential cellular functions such as cell proliferation, energy production, and DNA and protein synthesis. 39 Targeted metabolomics of 1C metabolites revealed that several precursors, predominantly of the folate-dependent 1C pathway but not the folate-independent 1C pathway, were significantly reduced in microbiomes of exercised mice (Figures 3E-3H). We identified a significant decrease in folic acid, glycine, and sarcosine and a reduction of threonine, dimethyl glycine, and histidine with exercise (Figures 3F-3H), all of which serve as substrates for formate production—a short-chain fatty acid (SCFA)36,40 and key 1C pathway product. 37,41,42 Consistent with the depletion of substrates, we found exercise significantly increased levels of cecal formate (Figure 3I). Furthermore, we found formate levels to be significantly increased in serum (Figure 3J) and slightly elevated in tumors of exercised mice (Figure S4C), suggesting that exercise-induced microbiota-derived formate reaches systemic sites. Notably, serum formate correlated inversely with tumor growth (Figure 3K) and directly with antitumor Tc1 immunity (Figure 3L), supporting the hypothesis that elevated formate levels promote antitumor Tc1 immunity and restrain tumor growth. Exercise specifically enhanced formate without globally impacting other SCFAs (Figures S4D-S4F).

These findings revealed that exercise functionally remodels the gut microbiome by promoting folate-dependent 1C metabolism and thereby increasing formate production.

Formate improves ICI efficacy by enhancing tumor antigen-specific Tc1 immunity

We next sought to test whether formate administration is sufficient to restrain tumor growth in our model. Noting potential toxicity of formate, ⁴³ we verified a 200 mg/kg oral dose yielded safe, physiological formate levels, comparable to levels in exercised and exercise-FMT-recipient mice (Figures S4G and S4H). Daily oral formate administration potently restrained established BRAF^{V600E} tumor outgrowth (Figure 4A) and prolonged survival

(Figure 4B). Formate also restrained tumor growth in B16-F10 melanoma (Figure 4C), MC-38 adenocarcinoma (Figures 4D and 4E), and EL4 lymphoma (Figure 4F) models and dramatically reduced B16-F10 lung metastases (Figure 4G). While we observed that both α PD-L1 and formate monotherapy restrained tumor growth, combinatorial α PD-L1 and formate therapy synergistically slowed B16-F10 tumor growth (Figure 4H). Demonstrating that formate requires adaptive immunity to restrict tumor growth in BRAF^{V600E} melanoma-bearing mice, we found that formate failed to inhibit tumor growth in immunodeficient $Rag^{-/-}$ mice (Figure 4I). Accordingly, formate treatment failed to impact BRAF^{V600E} melanoma cell viability *in vitro* (Figure S4I).

We next sought to determine if formate enhances tumor antigen-specific Tc1 immunity (Figure 4J). Indeed, formate induced a significant expansion of cytotoxic IFN γ - and tumor necrosis factor- α (TNF- α)-producing ovalbumin (OVA)-specific CD8 T cells relative to vehicle-treated B16-OVA tumor-bearing mice (Figure 4K). An independent model using B16-F10 engrafted mice with adoptively transferred congenically marked pmel-1 T cell receptor (TCR) transgenic CD8 T cells (Figure S4J) similarly showed that formate significantly enhanced tumor antigen-specific Tc1 immunity linked with B16 tumor growth restraint (Figures S4K and S4L).

To substantiate our hypothesis that formate acts directly on CD8 T cells to mediate its antitumor effect, we stimulated splenic naive CD8 T cells with formate to probe Tc1 fate initiation and differentiation (Figure 4L). Indeed, 24 h after formate addition, CD8 T cells displayed significantly increased expression of the Tc1 transcription factor Eomesodermin (Eomes), were highly proliferative based on Ki67 expression, and produced more antitumor cytokines relative to PBS-treated CD8 T cells (Figure 4M). Highlighting a formate-triggered enhancement of Tc1 differentiation, these effector responses were even more pronounced after 72 h (Figure 4M).

Collectively, these results demonstrated formate has potent, tumor-model-independent antitumor potential by enhancing tumor antigen-specific Tc1 immunity.

Microbiota-derived formate is essential for mediating antitumor Tc1 immunity both *in vitro* and *in vivo*

Formate is produced by microbiota and host. ^{37,44} Two key observations indicated that microbiota-derived formate mediated the exercise-induced antitumor effect. First, while voluntary exercise, comparable to treadmill exercise, significantly increased cecal formate abundance in SPF mice (Figures 3I and 5A), voluntary exercise in GF mice—which failed to

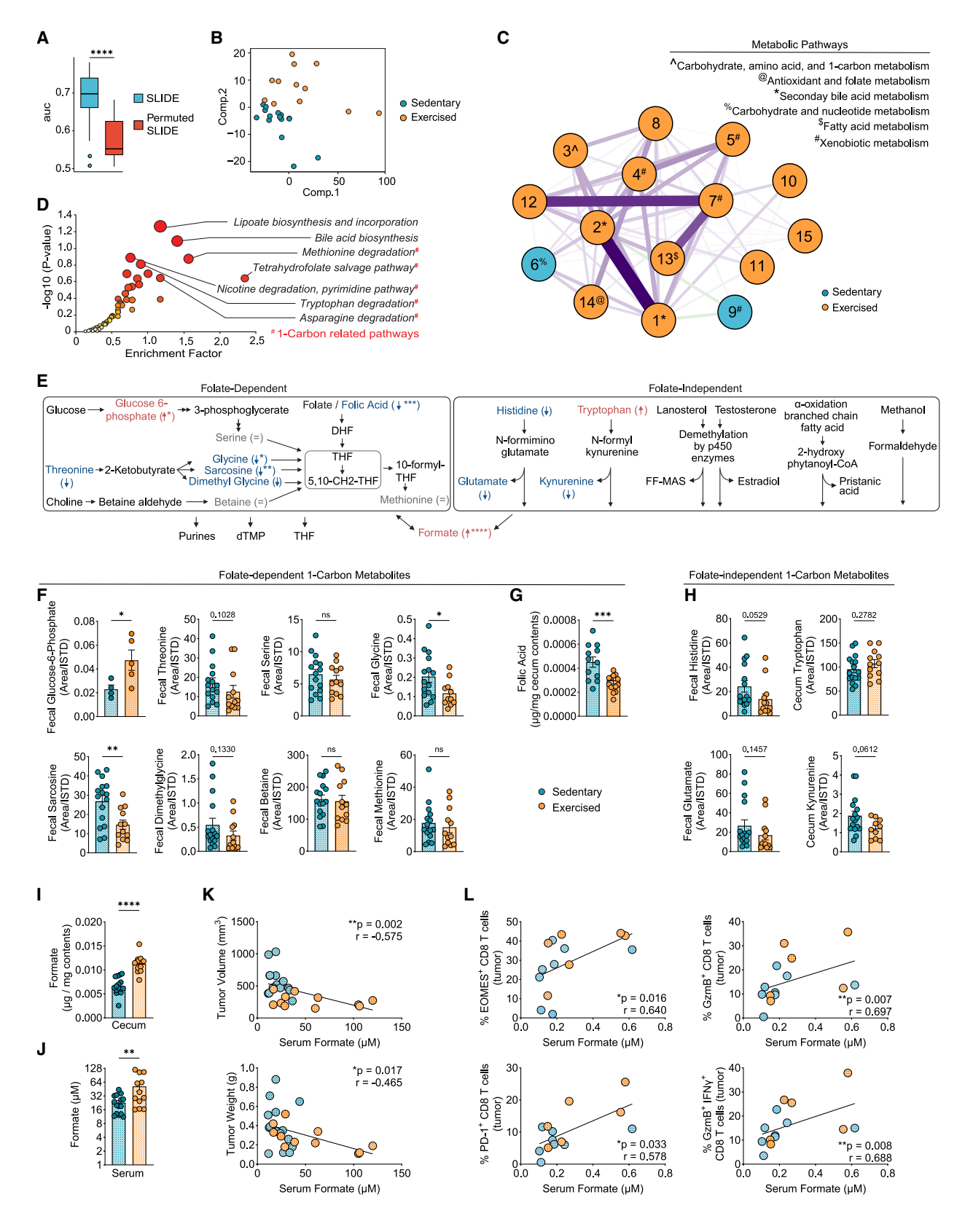
Figure 2. Exercise-induced microbiota metabolites restrain ICI-resistant melanoma tumor growth and enhance antitumor Tc1 cell immunity in vitro and in vivo

- (A) Experimental outline of (B). ABX-pretreated mice received live or heat-killed FMT followed by BRAF^{V600E} TCE (n = 5 mice/group).
- (B) Tumor growth.
- (C) Experimental outline of (D) and (E). Naive CD8 T cells stimulated with microbiota metabolites (n = 6 mice/group).
- (D) Frequencies of cytokine production.
- (E) Relative gene expression.

(F and G) Mice received cultured microbiota metabolites orally after BRAF V600E TCE (n=5 mice/group). (F) Tumor growth. (G) Frequencies and representative plots. (B and F) Mean \pm SEM, two-way ANOVA with Sidak's correction for multiple comparisons. (D and E) Individual samples/group, repeated measures one-way ANOVA. (G) Individual mice, unpaired t test. Mean \pm SEM. *p < 0.05, **p < 0.01, ****p < 0.001, *****p < 0.0001; ns, not significant. See also Figure S3.







(legend on next page)





suppress melanoma growth (Figure 1M)-did not notably alter formate levels in cecal contents or serum (Figures 5A and S5A). Second, exercise-induced functional microbiome shifts, characterized by increased formate production, persisted in EX-FMT recipients for at least 3 weeks post FMT and correlated with enhanced antitumor Tc1 immunity. Specifically, analysis of cecal 16S seq data from FMT-SED and FMT-EX mice using Phylogenetic Investigation of Communities by Reconstruction of Unobserved States 2 (PICRUSt2)⁴⁵ revealed global functional shifts (Figure 5B), with predicted enrichment of 1C metabolism pathways (Figure 5C; Table S2). Accordingly, predicted abundance of pyruvate formate lyase (pfl)-an essential enzyme for bacterial formate production⁴⁴-increased in EX-FMT recipients (Figure 5D), primarily driven by Desulfovibrio, an unclassified genus in the Erysipelotrichaceae family, and in part by Dubosiella (Erysipelotrichaceae) (Figure S5B). Consistently, EX-FMT recipients exhibited significantly elevated cecal formate levels 3 weeks post FMT (Figure 5E). Furthermore, both serum and tumor formate levels were elevated in FMT-EX mice compared with FMT-SED recipients (Figures S5C and S5D), which correlated positively with increased intratumoral Tc1 immunity (Figure S5E). Other SCFAs remained largely unaffected in FMT recipients (Figure S5F). Further underscoring the durability of these functional microbiome changes post FMT, the exercise-induced increase in pfl abundance—observed after exercise but prior to FMT-was mainly driven by Dubosiella-a member of the Erysipelotrichaceae family-and Bifidobacterium (Figures 1 and S5G) and was associated with elevated 1C metabolism (Figures 3C-3H) and formate production (Figure 3I).

Taken together, these findings suggested that exercise induced lasting functional microbiome changes, leading to enhanced formate production, which boosted antitumor Tc1 immunity and suppressed tumor growth.

To confirm the critical role of microbiota-produced formate in mediating the antitumor effect, we generated a commensal $E.\ coli$ strain that lacks $pfl\ (\Delta pfl\ E.\ coli)$. We confirmed $\Delta pfl\ E.\ coli$, unlike WT $E.\ coli$, was unable to produce formate $in\ vitro\ (Figure\ S5H)$ or increase serum formate levels $in\ vivo\ (Figure\ S5I)$. Additionally, comparable growth rates $in\ vitro\ and\ survival\ in\ vivo\ suggested\ no\ significant\ fitness\ deficit\ in\ <math>\Delta pfl\ E.\ coli\ (Figures\ S5J\ and\ S5K)$.

To examine the impact of microbiota-derived formate on its ability to promote Tc1 differentiation and effector function, we stimulated naive WT CD8 T cells with sterile-filtered supernatant derived from WT E. coli and Δpfl E. coli that we confirmed for presence and absence of formate, respectively (Figures 5F and S5H). While we found that formate-containing WT E. coli supernatant potently enhanced Tc1 differentiation and effector function, non-formate-containing Δpfl E. coli supernatant did not (Figures 5G–5I). Specifically, WT E. coli supernatant significantly enhanced IFNy and GzmB production (Figure 5G), promoted higher Eomes expression, which was linked to increased IFNy production (Figure 5H), and enhanced cytotoxic Tc1 cell proliferation compared with Δpfl E. coli supernatant (Figure 5I). This observation demonstrated that other E. coli components (e.g., lipopolysaccharide [LPS]) besides formate are insufficient to drive Tc1 fate, underscoring the critical role of microbiotaderived formate in promoting Tc1 immunity in vitro.

Finally, to assess the impact of microbiota-derived formate on BRAF^{V600E} tumor outgrowth, mice were colonized with WT *E. coli* or Δpfl *E. coli*. Excitingly, while WT *E. coli* treatment efficiently restrained tumor growth, Δpfl *E. coli* treatment, similar to vehicle-treated mice, failed to impact tumor growth (Figure 5J). In addition, WT *E. coli*, but not Δpfl *E. coli*, restrained B16-F10 tumor growth (Figure 5K), demonstrating that the microbiota-derived formate-mediated antitumor effect is not restricted to BRAF^{V600E} melanoma. Early immune responses, assessed by flow cytometry of B16-F10 tumor-infiltrating lymphocytes 2 days post-*E. coli* administration, showed WT *E. coli* treatment expanded intratumoral CD8 T cells with increased proliferation and GzmB production versus Δpfl *E. coli* treatment (Figure 5L).

Collectively, our findings demonstrate that microbiota-derived formate is required to promote Tc1 immunity *in vitro* and to mediate antitumor effects *in vivo*.

Nrf2 activation within CD8 T cells is critical for formateenhanced Tc1 immunity *in vitro* and formate-mediated antitumor effects *in vivo*

To understand the mechanism by which exercise-induced microbial metabolic alterations, including increased formate, enhance Tc1 antitumor immunity, we mined the KEGG pathway database using the *Mummichog* algorithm, analyzing all

Figure 3. Exercise promotes enrichment in microbial 1C metabolism

(A–F and H) Untargeted metabolomics analysis of feces (n = 12-16 mice/group).

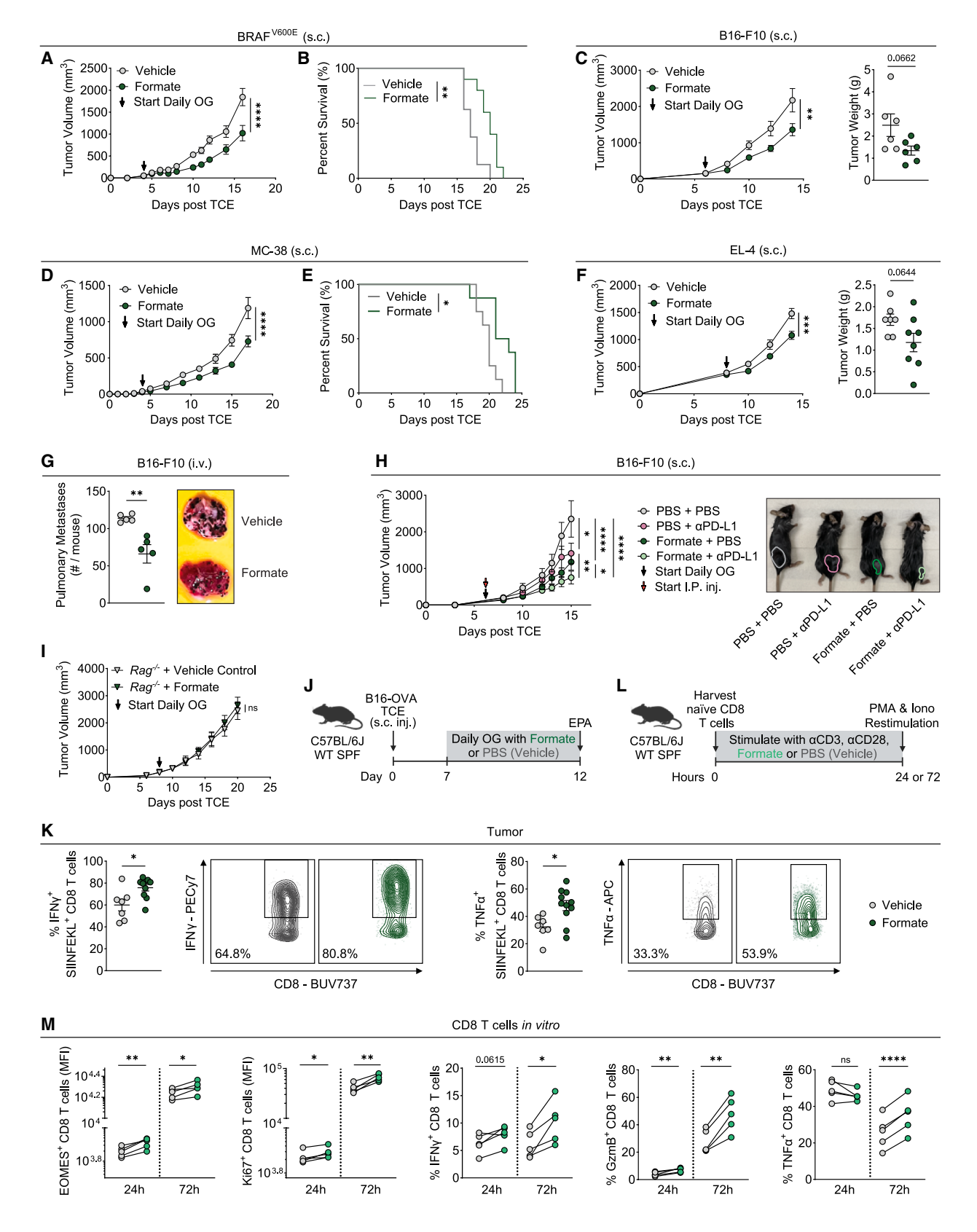
- (A) SLIDE cross-validation performance.
- (B) Score plots for each sample using the top two components from partial least squares regression, using all metabolites in SLIDE latent factors.
- (C) Correlation network for metabolites in SLIDE latent factor Z3.
- (D) Mummichog enrichment and significance for differentially expressed metabolites identified by partial least squares regression, with point size indicating $-\log_{10} p$ value.
- (E) Folate-dependent and folate-independent 1C metabolism. Metabolites identified by untargeted and targeted metabolomics (in F–H) are shown in red (increased with exercise), gray (no significant change with exercise), or blue (reduced with exercise). Statistical differences are indicated by asterisks.
- (F) Relative abundance of folate-dependent 1C metabolites.
- (G) Folic acid in cecum.
- (H) Relative abundance of folate-independent 1C metabolites.
- (I-L) Exercised or sedentary mice received BRAFV600E TCE. n = 12-16 mice/group. (I and J) Formate quantification. (K and L) Spearman correlations.

(A and F–J) Individual mice, unpaired t test. Mean \pm SEM. (K and L) Individual mice, Spearman correlation. *p < 0.05, **p < 0.01, ****p < 0.001, ****p < 0.0001; ns, not significant.

See also Figure S4.







(legend on next page)





metabolite features from exercised and sedentary mouse microbiomes (Table S1). We found several pathways to be significantly enriched, with the most statistically significant being the aryl hydrocarbon receptor (AhR) activation pathway (Figure 6A; Table S1). Prior work demonstrated that the microbial AhR agonist indole-3-aldehyde enhances Tc1 immunity, aggravating autoimmunity⁴⁶ and improving ICI efficacy.^{32,47} Although formate activated AhR (Figure S6A), both its enhancement of Tc1 effector function in vitro (Figures S6B and S6C) and the exercise-induced antitumor effect (Figure S6D) were AhR-independent. AhR ligands can also signal via nuclear factor erythroid 2-related factor 2 (Nrf2), 48-51 a pleiotropic transcription factor involved in redox homeostasis, metabolism, and immune modulation.⁵² The role of Nrf2 in cancer is poorly understood and controversial, presumably driven by cell type-specific effects.⁵³⁻⁵⁵ We first set out to assess the role of Nrf2 in the exercise-induced antitumor effect. We observed that exercise enhanced the production of microbiota-derived Nrf2-activating metabolites that may reach the periphery, as evidenced by the significantly increased Nrf2 activation potential of intestinal contents (Figure 6B) and sera (Figure 6C) from exercised mice. Next, mice with established BRAFV600E tumors were exercised or kept sedentary while receiving an Nrf2 inhibitor or vehicle to test if Nrf2 blockade affects the exercise-triggered antitumor effect. While exercise restrained tumor outgrowth in vehicle-treated mice, Nrf2 inhibition significantly impaired the exercise-induced tumor suppression (Figure 6D). Microbial Nrf2 activity directly correlated with formate levels (Figure S6E), implying that formate drives microbial Nrf2 activity. Consistently, intestinal contents from FMT-EX recipients showed increased Nrf2 activation ability compared with FMT-SED recipients (Figure S6F). In addition, we found that formate activated the Nrf2 pathway (Figure 6E) and increased Nrf2 downstream gene transcription in CD8 T cells in vitro (Figure 6F).

We next investigated whether Nrf2 activation is essential for formate to enhance Tc1 immunity. While formate, as expected, boosted Tc1 immunity in Nrf2^{+/+} CD8 T cells, it strikingly failed to promote Tc1 effector function in Nrf2^{-/-} CD8 T cells (Figure 6G). Moreover, Nrf2 inhibition prevented formate-induced Tc1 differentiation *in vitro* (Figure 6H) and limited formate-improved tumor antigen-specific OT-I tg CD8 T cell B16-OVA tumor cell killing abilities (Figure 6I). Further supporting the role of microbiota-derived formate in promoting Tc1 immu-

nity through Nrf2 activation, we found that Nrf2 blockade significantly impaired the ability of formate-containing WT *E. coli* supernatant to enhance Tc1 immunity *in vitro* (Figure 6J). Next, we generated a mouse model with selective Nrf2 depletion in CD8 T cells to assess the role of Nrf2 signaling in formate-mediated tumor suppression. As expected, formate effectively restrained tumor growth in *Nrf2*^{fl/fl} CD8 Cre⁻ littermates (Figure 6K). However, in *Nrf2*^{fl/fl} CD8 Cre⁺ mice, formate failed to suppress tumor growth, highlighting the critical role of Nrf2 signaling in CD8 T cells for formate-driven tumor growth restraint (Figure 6K).

We investigated whether other Nrf2 agonists beyond formate, such as the food additive tert-butylhydroquinone (TBHQ), possess antitumor potential. ^{56,57} After verifying TBHQ as an Nrf2 agonist (Figure S6G), we interrogated its impact on melanoma tumor growth. Oral TBHQ treatment significantly suppressed tumor growth in two melanoma models (Figures S6H and S6I). TBHQ treatment enhanced CD8 T cell, but not CD4 T cell, infiltration (Figure S6J), proliferation (Figure S6K), and the expansion of activated, cytotoxic Tc1 cells within the TME (Figure S6L). Additionally, TBHQ directly promoted Tc1 immunity *in vitro* (Figures S6M–S6O). These data suggest that the Nrf2 agonist TBHQ triggers an antitumor mechanism mirroring that of formate.

To understand how formate promotes Nrf2-dependent Tc1 differentiation, we analyzed global transcriptomic changes in naive CD8 T cells stimulated with formate. As expected, formate triggered an upregulation of differentially expressed genes (DEGs) involved in 1C metabolism, such as serine hydroxymethyltransferase 2 (Shmt2)42,58 and cystathionine gammalyase (Cth),59 as well as genes regulated by Nrf2 (e.g., Cth,60 NADH dehydrogenase 4 [mt-Nd4], 61 and transketolase [Tkt]^{62,63}) (Figure 6L; Table S3). Importantly, formate significantly increased genes associated with Tc1 activation and differentiation, such as receptor-interacting serine/threonine-protein kinase 2 (Ripk2), 64 zinc transporter ZIP8 (Slc39a8), 65 furin, 66 poly (ADP-ribose) polymerase 1 (Parp1), 67,68 ezrin (Ezr), 69 and interferon regulatory factor 8 (Irf8).70-72 Transcription factor enrichment analysis⁷³ revealed that formate-induced transcriptional changes were linked with an enrichment in transcription factors regulating proliferation and metabolism (e.g., Myc, Max, and Myb), 74 effector function (e.g., Fos, Rela, Stat1, and Cebpb), 75-77 and differentiation and epigenetic control (e.g., Ets1, Yy1, and $Pou2f2)^{/8}$ (Figure 6M).

Figure 4. 1C metabolite formate restrains growth of multiple tumor types and improves αPD-L1 efficacy

(A–F) Mice received oral formate or vehicle once tumors were palpable (n = 5–10 mice/group). BRAF^{V600E} (A and B), B16-F10 (C), MC-38 (D and E), and EL-4 (F) tumor models. (A, C, D, and F) Tumor growth. (C and F) Tumor weight. (B and E) Survival.

⁽G) Following intravenous B16-F10 administration, mice received oral formate or vehicle (n = 5 mice/group). Total number of pulmonary metastases and representative images.

⁽H) Mice received oral formate and intraperitoneal (i.p.) injection of α PD-L1 once B16-F10 tumors were palpable (n = 6 mice/group). Tumor growth and representative images.

⁽I) $Rag^{-/-}$ mice received oral formate beginning when BRAF^{V600E} tumors were palpable (n = 5-6 mice/group). Tumor growth.

⁽J) Experimental outline of (K). Mice received oral formate starting once B16-OVA tumors were palpable (n = 8-11 mice/group).

⁽K) Frequencies and representative plots of CD8 T cells.

⁽L) Experimental outline of (M). Naive CD8 T cells were stimulated with formate (n = 5 mice/group).

⁽M) Frequency and mean fluorescence intensity (MFI) of CD8 T cells.

⁽A, C, D, F, H, and I) Mean \pm SEM, two-way ANOVA with Sidak's correction for multiple comparisons. (B and E) Log-rank test. (C, F, G, and K) Individual mice, unpaired t test. Mean \pm SEM. (M) Individual samples/group, paired t test. *p < 0.05, **p < 0.01, ****p < 0.001, ****p < 0.0001; ns, not significant. See also Figure S4.





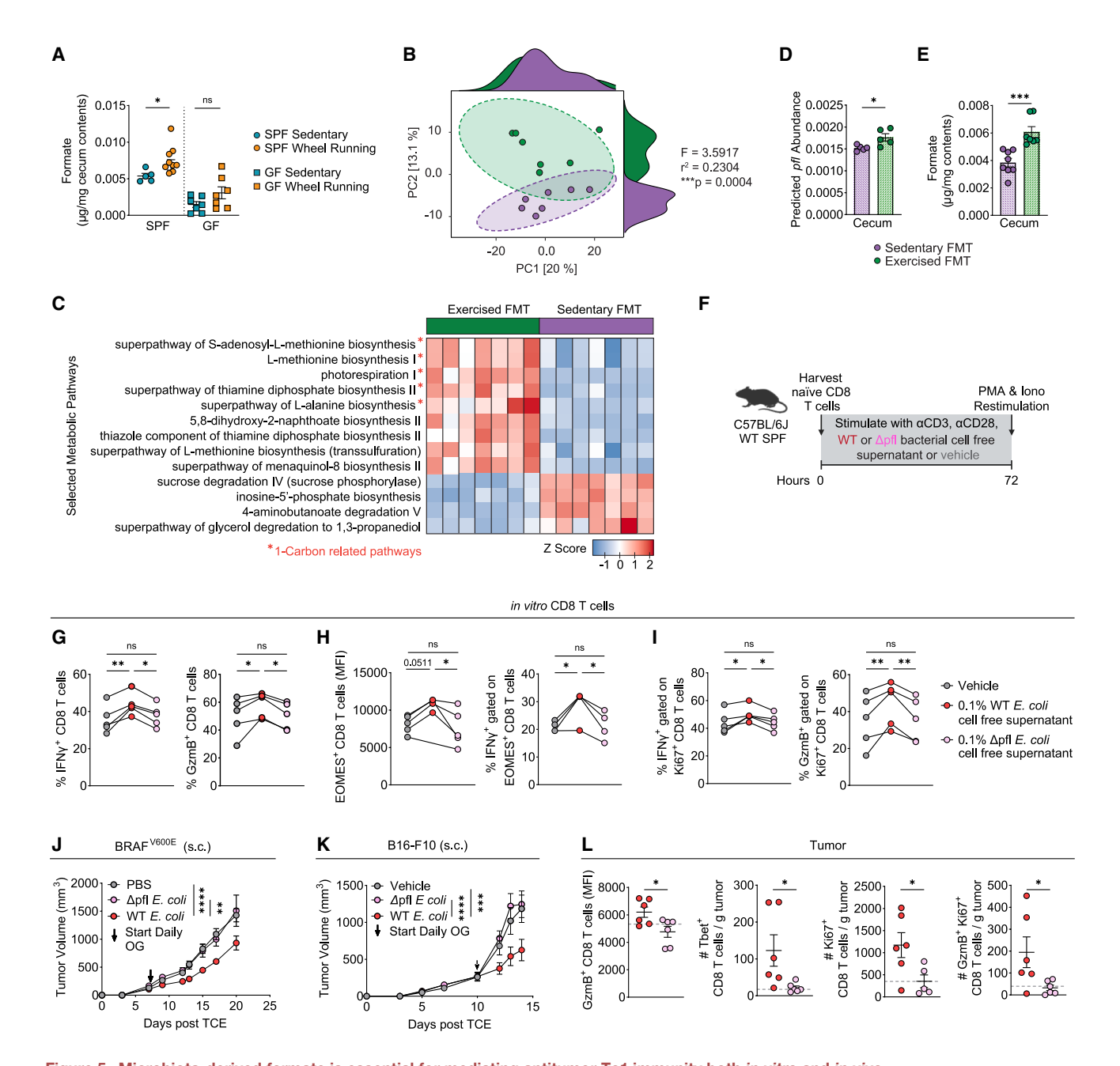


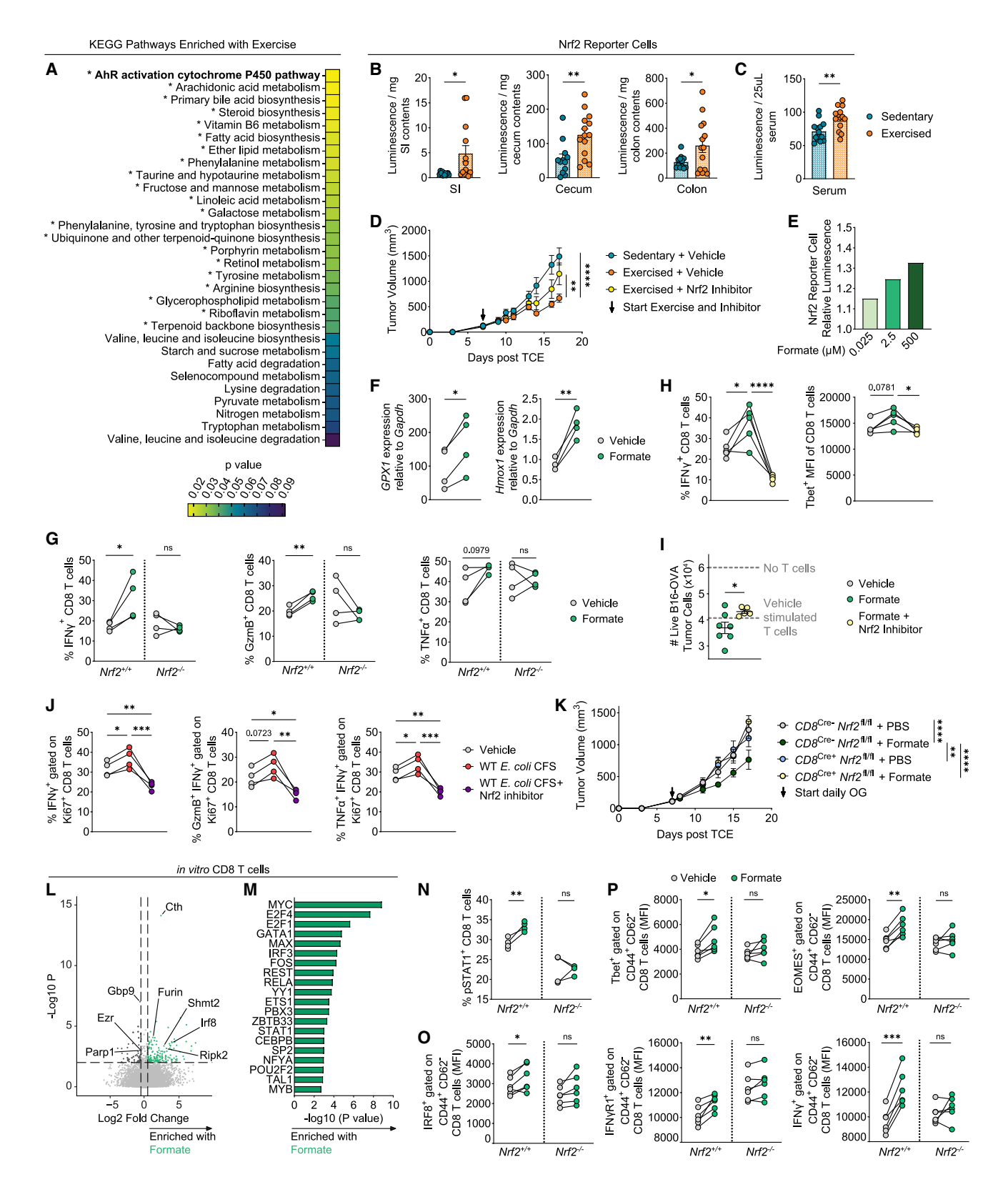
Figure 5. Microbiota-derived formate is essential for mediating antitumor Tc1 immunity both in vitro and in vivo

(A) Formate quantification.

(B–E) 16S seq and formate abundance of FMT-recipient cecum contents. (B–D) PICRUSt2 analysis between FMT groups. (B) PCA plot of MetaCyc pathways. (C) Predicted gene counts collapsed and annotated with MetaCyc pathway database. Selected pathways were significant at false discovery rate (FDR)-corrected p value < 0.05 with linear discriminant analysis (LDA) Z score > 3.9. (D) Predicted relative abundance of EC_2.3.1.54 (pfl) in cecum contents. (E) Formate quantification.

- (F) Experimental outline for (G)-(I). WT E. coli or Δpfl E. coli cell-free culture supernatant was applied to naive CD8 T cells in vitro (n = 5 mice/group).
- (G) Frequency of CD8 T cells.
- (H) Mean fluorescence intensity (MFI) and frequency of CD8 T cells.
- (I) Frequency of CD8 T cells.
- (J-L) Mice engrafted with BRAF^{V600E} (J) and B16-F10 (K) tumor cells. Tumor growth. B16-F10 tumors were analyzed in (L), and the dotted gray line indicates the mean of vehicle-treated samples.
- (A, D, E, and L) Individual mice/group, unpaired t test. Mean \pm SEM. (G–I) Individual samples/group, paired one-way ANOVA. (J and K) Mean \pm SEM, two-way ANOVA with Sidak's correction for multiple comparisons. *p < 0.05, **p < 0.01, ***p < 0.001, ****p < 0.001; ns, not significant. See also Figure S5.





(legend on next page)





We then examined if formate-induced transcriptional changes drive Nrf2-dependent functional alterations influencing Tc1 fate. We previously demonstrated the microbiota AhR agonist, indole-3-aldehyde, potently induced cAMP response elementbinding protein (CREB) phosphorylation in CD8 T cells, triggering enhanced cytotoxic cytokine production.³² CREB serves as a critical transcriptional enhancer of key type 1 effector genes⁷⁵ and induces CCAAT enhancer binding protein beta (CEBPB) expression, a potential driver of formate-induced transcriptional changes (Figure 6M). However, formate failed to enhance CREB phosphorylation in CD8 T cells (Figures S6P and S6Q). Next, we focused on evaluating the role of signal transducer and activator of transcription (STAT1), a key Tc1 immune-enhancing transcription factor⁷⁹ that we also identified as one potential driver of formate-induced transcriptional changes (Figure 6M). Intriguingly, we found that formate stimulation of CD8 T cells in vitro led to significantly increased phosphorylation of STAT1 (Figure 6N). Irf8, a transcription factor transcriptionally upregulated by formate (Figure 6L), is pivotal for Tc1 differentiation^{70–72} and regulated by STAT1.80 Consistent with the increase in STAT1 activation (Figure 6N), we found that formate significantly enhances IRF8 protein expression in activated CD44+ CD62Llo effector CD8 T cells in vitro (Figure 6O). Supporting the notion that formateinduced upstream signaling events enhance Tc1 differentiation, we found formate promotes a robust increase in the Tc1 effector profile, as evidenced by elevated expression of Tbet, Eomes, IFNyR1,81 and IFNy (Figure 6P). Importantly, formate failed to induce pSTAT1 activation and Tc1 cell effector function in Nrf2deficient CD8 T cells, demonstrating that formate promotes Tc1 effector function in an Nrf2-dependent manner (Figures 6N-6P).

Collectively, we demonstrate that exercise-induced, microbiota-derived formate enhances Tc1-mediated antitumor immunity by activating the Nrf2 pathway in CD8 T cells, which is essential for formate-driven Tc1 differentiation, effector function, and tumor suppression.

A high-formate-producing human microbiota enhances tumor suppression and promotes robust antitumor Tc1 immunity

With the goal to interrogate a possible link between formate production in the human gut microbiome and human ICI efficacy

in melanoma, we performed a meta-analysis of microbial sequencing data from nine published independent cohorts of αPD1-treated patients with melanoma. 82-87 Deploying two independent bioinformatic approaches, namely batch correction (using ConquR88) and meta-analysis using the common effects model (using Meta-Mar⁸⁹), we uncovered in each approach that an increased fecal abundance of pfl is linked with response to human ICI therapy in melanoma (Figures 7A, 7B, and S7A; Table S4). We found that the taxa driving the increase in pfl abundance in feces of human ICI responders are primarily Lachnospiraceae, as well as Erysipelotrichaceae and Oscillospiraceae (Figure S7B; Table S4). To determine whether the primary pfl drivers in human ICI responder microbiomes are similar to those induced by exercise in our model-and consequently linked to formate production-we performed metagenomic analyses of cecal contents from exercised and sedentary mice. Indeed, the exercise-induced increase in pfl gene abundance was primarily driven by metagenome-assembled genomes (MAGs) affiliated with Lachnospiraceae (MAGs: 100, 99, 150, 123, 166, and 153), Erysipelotrichaceae (MAG 10), Akkermansiaceae (MAG 12), Acutalibacteraceae (MAG 121), and Oscillospiraceae (MAG 137) (Figures S7C-S7E; Table S5). Among these, three MAGs-100, 99, and 150emerged as the top contributors to the observed increase in pfl abundance and were significantly enriched in the exercised metagenomes (Figure S7E; Table S5). Notably, MAG 100, affiliated with Lachnospiraceae, specifically genus UBA3282, exhibited the most pronounced exercise-induced increase, with a 13.4-fold enrichment in pfl gene abundance relative to sedentary controls (Figure S7E; Table S5). Importantly, pfl gene abundance in MAG 100 directly and significantly correlated with cecal formate levels (Figure S7F). Altogether, these data posit that similar pfl-expressing taxa may drive formate production in both exercised mice and human ICI responders.

Next, to assess a possible link between systemic formate levels and human ICI response, we measured serum formate levels in a new cohort of advanced melanoma patients that underwent ICI treatment. While there was no statistically significant difference between responders and non-responders (Figure 7C), stratifying patients by high or low serum formate levels revealed a significant association between higher formate levels and prolonged progression-free survival (Figure 7D).

Figure 6. Nrf2 activation within CD8 T cells is critical for formate-enhanced Tc1 immunity in vitro and formate-mediated antitumor effects in vivo

(A) KEGG pathways.

(B and C) Relative luminescence of Nrf2 reporter cells.

(D) BRAF^{V600E} tumor volume (n = 6-10 mice/group).

(E) Relative luminescence of Nrf2 reporter cells.

(F) Naive CD8 T cells stimulated with formate (n = 4 mice/group). Nrf2 downstream gene expression.

(G) $Nrf2^{+/+}$ or $Nrf2^{-/-}$ naive CD8 T cells stimulated with formate (n = 4 mice/group). Frequencies of CD8 T cells.

(H) Naive CD8 T cells stimulated with formate and Nrf2 inhibitor (ML-385) (n = 5 mice/group). Frequency and mean fluorescence intensity (MFI) of CD8 T cells.

(I) Number of viable tumor cells following application of pretreated tumor antigen-specific CD8 T cells.

(J) Naive CD8 T cells stimulated with WT E. coli cell-free supernatant (CFS) and Nrf2 inhibitor. Frequency of CD8 T cells.

(K) BRAF^{V600E} Tumor growth (n = 6-13 mice/group).

(L and M) Bulk RNA-seq of naive CD8 T cells stimulated with formate. (L) Volcano plot. (M) Transcription factor enrichment analysis of DEGs.

(N-P) Nrf2^{+/+} or Nrf2^{-/-} naive CD8 T cells stimulated with formate (n = 5 mice/group). (N) Frequency of CD8 T cells. (O and P) MFI of activated CD8 T cells.

(B, C, and I) Individual samples/group, unpaired t test. Mean \pm SEM. (D and K) Mean \pm SEM, two-way ANOVA with Sidak's correction for multiple comparisons. (F, G, and N-P) Individual samples/group, paired t test. (H and J) Individual samples/group, RM one-way ANOVA. *p < 0.05, **p < 0.01, ****p < 0.001, ****p < 0.0001; ns, not significant.

See also Figure S6.



Finally, to explore if human microbiota-derived formate is a biomarker for enhanced antitumor Tc1 immunity, we quantified absolute formate levels in stool from 26 healthy adults (Figure 7E). To assess if fecal formate correlates with antitumor effects, we transplanted human donor stool from the three highest (referred to as "Formate-HIGH") and three lowest (referred to as "Formate-LOW") formate producers into ABX-pretreated mice (Figures 7F and 7G). Of note, Formate-HIGH donor material displayed a significantly higher formate content over Formate-LOW donor material (Figure 7F). Excitingly, Formate-HIGH FMT recipients showed significantly greater BRAFV600E tumor suppression compared with both Formate-LOW FMT and self-FMT groups (Figure 7H). This was accompanied by a significantly elevated Tc1 antitumor immunity within the TME in Formate-HIGH FMT recipients when compared with Formate-LOW FMT recipients (Figure 7I). At EPA, day 19 post-TCE, a time point associated with a robust antitumor Tc1 response (Figure 7I), cecal formate levels were significantly higher in Formate-HIGH recipients, confirming that the formate-producing phenotype remained stable post-transplantation and correlated with potent Tc1 immunity (Figure 7J). While serum formate levels were elevated in Formate-HIGH recipients compared with Formate-LOW recipients, the difference was not statistically significant (Figure 7K). However, serum formate levels inversely correlated with tumor growth (Figure 7L), suggesting a systemic link between formate abundance and antitumor effects.

Taken together, our findings identify human microbiotaderived formate as a potential biomarker of enhanced Tc1-mediated antitumor immunity and support its functional role in driving melanoma tumor suppression.

DISCUSSION

Our study shows that exercise-stimulated, microbiota-derived formate enhances antitumor immunity by promoting Tc1 immunity and improving ICI efficacy. We demonstrate that exerciseinduced changes in the gut microbiota are both necessary and sufficient to restrain tumor growth in BRAFV600E melanoma, mediated by an enrichment in the folate-dependent 1C metabolic pathway. We identify formate as a key metabolite driving this effect, showing that it enhances tumor antigen-specific Tc1 immunity, improves ICI response, and restrains tumor progression across multiple cancer models. Mechanistically, we establish that formate activates Nrf2 within CD8 T cells, a critical step in promoting exercise-enhanced Tc1 effector function, which is required for antitumor effects of exercise. Finally, we provide translational evidence that a high-formate-producing human microbiota is associated with enhanced tumor suppression and robust Tc1 immunity.

Exercise exerts potent antitumor effects in both preclinical models^{5,8-13} and cancer patients.⁶ We discovered that exercise-induced microbiome changes are critical for the exercise-induced antitumor effect. Future studies should explore the mechanism(s) of how exercise triggers microbiome changes.

Our findings reveal that exercise induces lasting functional changes in the microbiome—along with taxonomic shifts—highlighted by enhanced formate production persisting for at least 3 weeks post FMT. Most consistently, we observed a sustained

increase in *pfl* expression within the *Erysipelotrichaceae* family (particularly in an unclassified genus and the genus *Dubosiella*) and the *Lachnospiraceae* family, suggesting these taxa are key contributors to exercise-induced formate production. Moreover, exercise boosted *pfl* abundance in microbial taxa regardless of whether their overall population increased or decreased in response to the exercise regimen, suggesting that both enriched and reduced taxa are key contributors to exercise-induced formate production.

In vitro formate pretreatment of human colorectal adenocarcinoma HT-29 cells accelerated tumor growth in immunocompromised mice. 90 Consistently, our findings in Rag^{-/-} mice showed that formate failed to restrain tumor growth. By contrast, our study using immunocompetent WT mice demonstrated that formate exerts potent antitumor effects by enhancing Tc1 immunity, emphasizing the critical role of immune cells, particularly CD8 T cells, in formate-mediated antitumor immunity. Formate facilitated αPD-L1 efficacy in B16-F10 melanoma that was correlated with an increase in CD8 T cell effector function⁹¹; further, methanol, which elevated serum formate levels, enhanced αPD1 efficacy in an MC38 colon cancer model. 92 These findings, together with our work, imply that the impact of formate in cancer is cell-type and context dependent, stressing the importance of studying the role of formate across various cell types and cancer models in further analyses.

We observed that the synthetic Nrf2 agonist and food additive TBHQ^{56,57} suppressed melanoma tumor growth and enhanced antitumor Tc1 immunity both *in vitro* and *in vivo*. These findings align with prior reports on the Nrf2 agonist Auranofin—a gold (I)-containing phosphine compound—which enhanced the antitumor function of human tumor-infiltrating T cells by reducing reactive oxygen species. ⁹³ Further investigation is warranted to elucidate the mechanisms by which TBHQ^{56,57} contributes to tumor suppression.

We uncovered that formate-enhanced Tc1 immunity *in vitro* is linked with an increased activation of the pSTAT1-IRF8 axis that depends on Nrf2. Future research aimed at identifying the downstream molecular mediators of formate in CD8 T cells that are critical to drive Tc1 fate could unveil therapeutic strategies to harness the antitumor benefits of exercise, enhancing cancer immunotherapy at a molecular level.

Our meta-analysis of microbial sequencing data from nine independent $\alpha PD\text{-}1\text{-treated}$ melanoma cohorts $^{82\text{-}87}$ revealed a higher abundance of pfl, a key enzyme in bacterial formate production, linked to ICI efficacy. However, further studies in larger cohorts are needed to determine whether microbiota-derived formate levels predict ICI response in melanoma and other cancers.

The observation that human high-formate-producing microbiota is associated with tumor suppression and enhanced antitumor Tc1 immunity in a preclinical melanoma model begs the question of whether human microbiota-derived formate could serve as a metabolic biomarker for identifying FMT "super-donors" to enhance human ICI efficacy. However, this hypothesis requires further investigation in both preclinical and clinical studies. Additionally, it will be crucial to identify the key microbial taxa that predominantly drive formate production in the human microbiome.





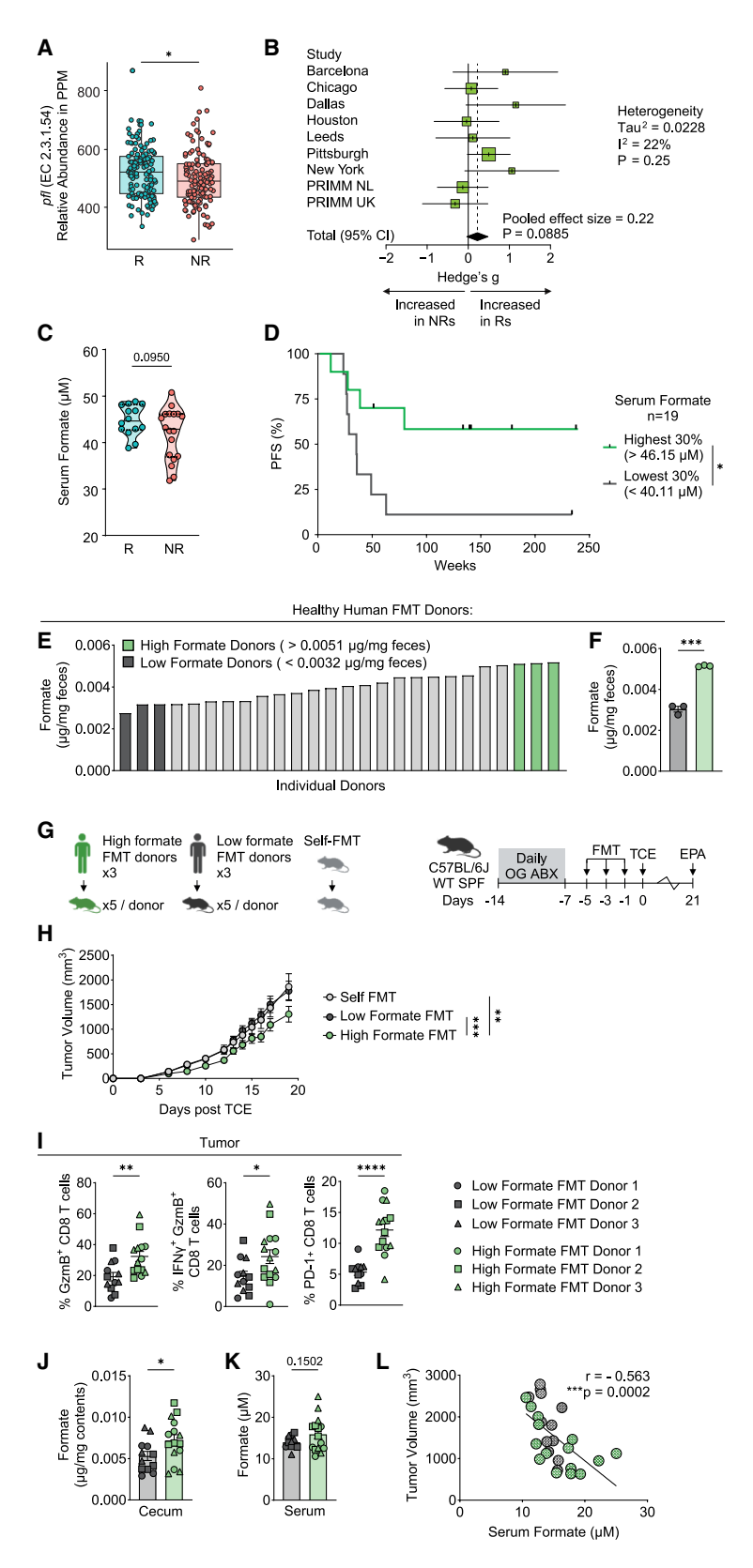


Figure 7. A high-formate-producing human microbiota enhances tumor suppression and promotes robust antitumor Tc1 immunity

(A and B) Meta-analysis of microbial sequencing data from stool samples of α PD-1-treated melanoma patients. (A) Boxplots of the batch-corrected metagenomic relative abundances in parts permillion (PPM) of genes annotated with EC_2.3.1.54 (*pfl*); NR, non-responder; R, responder. (B) Common effects model forest plot. (C and D) Melanoma patient formate in serum. (C) Formate quantification. (D) Kaplan-Meier progression-free survival (PFS) curve (n = 19 patients).

(E–L) Healthy human stool was used for FMT, followed by BRAF V600E TCE (n=15 mice/group). (E and F) Formate quantification. (G) Experimental outline for (H)–(L). (H) Tumor growth. (I) Frequency of CD8 T cells. (J and K) Quantification of formate. (L) Pearson correlation.

(A) Individual samples/group, Mann-Whitney t test. Mean \pm SEM. (C, F, and I–K) Individual samples/group, unpaired t test. Mean \pm SEM. (D) Log-rank test. (H) Two-way ANOVA with Sidak's correction for multiple comparisons.

(L) Spearman correlation, each dot representing individual mouse. $^*p < 0.05, ^{**}p < 0.01, ^{***}p < 0.001, ^{****}p < 0.0001.$ See also Figure S7.





While we demonstrated that aerobic exercise enhances ICI efficacy in preclinical melanoma models through the microbiotaderived metabolite formate, it needs to be explored whether other exercise modalities, such as anaerobic high-intensity interval training, elicit similar effects.

Future precision dietary interventions aimed at enhancing microbiota-derived formate production warrant investigation for their potential to amplify antitumor responses in melanoma and other cancer types.

Exercise influences the development of diseases like cancer, autoimmune disorders, and infections. We thus hypothesize that exercise-induced changes in the gut microbiota contribute to immunomodulatory effects in cancer and also autoimmunity and infections. However, this hypothesis requires further validation.

Our findings underscore the critical role of the microbiota in mediating exercise-driven enhancement of ICI therapy and identify formate as a promising metabolic target for improving cancer immunotherapy. Our study lays a rational mechanistic foundation for future investigations aimed at developing therapeutic strategies that combine exercise and microbial metabolites to evaluate the clinical antitumor efficacy of microbial Nrf2 agonists, such as formate, in ICI-resistant cancer patients.

Limitations of the study

Further studies are needed to identify the primary formate-producing microbes induced by exercise. Additional studies are warranted to better understand the molecular mechanisms by which formate influences Tc1 fate. Furthermore, the precise mechanism by which formate activates the Nrf2 pathway warrants further investigation in future studies. Beyond formate, other microbial factors or diverse CD8 T cell interactions may additionally contribute to the exercise-induced antitumor effect.

RESOURCE AVAILABILITY

Lead contact

Further information and requests for resources and reagents should be directed to and will be fulfilled by the lead contact, Marlies Meisel (marlies@pitt.edu).

Materials availability

Mouse lines generated in this study are available from the lead contact upon request.

Data and code availability

16S rRNA-seq (PRJNA1245478), RNA-seq (GEO: GSE294230), and metagenomic data (PRJNA1246250) are available via NCBI (SRA or GEO). Sample metadata and SRA accession numbers are in Table S4. All other supporting data are in the manuscript and supplemental information. Additional data for reanalysis are available upon request. No original code is reported.

ACKNOWLEDGMENTS

We thank the University of Pittsburgh's Unified Flow Core, Health Sciences Mass Spectrometry Core, and Gnotobiotic Core for their services. We thank the NIH Tetramer Core Facility. Schematics were created with BioRender.com. This work was supported by an Investigator Start-up Fund, Department of Immunology, University of Pittsburgh School of Medicine to M.M. and R.H.; NIH/NIDDK-R01DK130897, NIH/NCI-R01CA293654, NIH/NCI-R21CA259636, and MRA award (https://doi.org/10.48050/pc.gr.143738) 820677 and SPORE-NIH

P50CA254865 grant to M.M.; NIH-T32 CA082084 to A.C.M., A.H.L., and C.M. P.; NIH-F32CA284780 to T.D.; NIH-F31CA290756 to C.M.P.; NIH/NHLBI-R01HL160747 to I.N.; NIH-R01HL162658 to R.A.G.; NIH-T32DK007665 to N.B. W.; Vienna Doctoral School of Pharmaceutical, Nutritional, and Sport Sciences' Completion Grant of the University of Vienna to P.A.Z.; University of Vienna (Research Platform Active Ageing) and the EU program Interreg SK-AT (NutriAging) support to K.-H.W.; NIH (Al118807, DK138912, and Al188307), Burroughs Wellcome Fund (1017880), and US-Israel Binational Science Foundation (2021025) to S.E.W.; NIH-R01Al168478 and R21Al163721 and Hillman-Developmental Pilot-Award (NIH-P30CA047904) to R.H.; NIH/NIAID-DP2Al164325 to J.D.; S100D023402 and S100D032141 to S.L.G; Intramural NCI-NIH Research Program-support to T.M., J.H.B., R.R.R., J.A.M., and G.T.; K-INBRE grant P20GM103418 and Kansas State University Johnson Cancer Research Center Expansion and Innovation Award to S.T.M.L., T.G.R. and H. M.W.; and NIH R01CA253329 and U01CA272541 to J.F.P.

AUTHOR CONTRIBUTIONS

C.M.P. performed most experiments and data analyses and helped write the manuscript draft. N.B.W. processed and analyzed 16S rRNA sequences. T. D., A.H.L., Y.Z., D.M.R.J., S.P.P., C.R.L., and A.C.M. performed experiments and data analyses. A.B.I.R. and J.D. performed SLIDE analysis. S.K.R., J.H. S., L.H., and M.J.B. helped with experiments. T.G.R. and H.M.W. performed metagenomic analysis, and S.T.M.L. guided it. I.N. performed bile acid metabolomics. R.A.G. helped with lung metastasis experiments. K.H.S. provided intellectual input on exercise regimens. S.J.M. and S.L.G. performed mass spectrometry and data analyses. R.H. provided intellectual input and advice. K.-H.W. and P.A.Z. provided human fecal samples. M.G.W. and S.E.W. generated *E. coli* strains. D.D. and H.M.Z. provided melanoma patient sera. T.M., J. H.B., R.R.R., and J.A.M. performed human metagenomic fecal dataset analyses, guided by G.T. J.F.P. guided 16S rRNA analysis. M.M. conceived and designed research, guided interpretation, and wrote the manuscript.

DECLARATION OF INTERESTS

The authors declare no competing interests.

STAR*METHODS

Detailed methods are provided in the online version of this paper and include the following:

- KEY RESOURCES TABLE
- EXPERIMENTAL MODEL AND STUDY PARTICIPANT DETAILS
 - O Melanoma patient serum samples
 - Healthy human feces samples for human to mouse fecal microbiota transplant (FMT)
 - Bioinformatic meta-analysis of melanoma microbiome samples of nine independent cohorts
 - Animals
 - o Gnotobiotic animal husbandry
- METHOD DETAILS
 - o Exercise and sedentary treatment
 - o Tumor models
 - Generation and growth of the E. coli Δpfl mutant
 - o Administration of antibiotics, formate, TBHQ, and bacteria
 - o Fecal microbial transplantation (FMT)
 - Fecal microbiota metabolites (MM)
 - o Cultured fecal microbiota metabolites for in vivo treatment
 - Bacterial Cell Free Supernatants
 - O CD8/CD4 T cell depletion and anti-PDL1 mAb immunotherapy
 - $\,\circ\,$ Adoptive CD8 T cell transfer experiment
 - \circ In vivo AhR and Nrf2 inhibitor treatment
 - o Tissue harvest and cell purification
 - Flow cytometry
 - $\circ\,$ In vitro naı̈ve CD8 T cell stimulation
 - Phospho-CREB analysis
 - Phospho-STAT1 analysis





- o RNA processing and RT-PCR of CD8 T cells
- o RNAseq of CD8 T cells
- o Transcription Factor Enrichment Analysis (TFEA)
- Collection and processing of intestinal contents and serum for Nrf2 reporter cell assays
- o Nrf2 reporter cell assay
- o AhR reporter cell assay
- o DNA for 16S quantification in feces
- o Tumor cell killing assay
- o Growth curve of BRAF with CCK-8 Assay
- o 16S Analysis and sample processing
- O Untargeted high-resolution LC-HRMS
- Significant Latent Factor Interaction Discovery and Exploration (SLIDE) Analysis
- o Bile acids detection in fecal samples
- o 3NP-Short chain fatty acid (SCFA) detection
- o Enzyme-linked immunosorbent assay (ELISA) to measure folic acid
- O Recovery of WT E. coli and Δpfl E. coli from SPF Mice
- Bioinformatic meta-analysis of melanoma microbiome samples of nine independent cohorts
- Metagenomic Sequencing of mouse cecum contents
- O Human stool fecal microbial transplant (FMT) into mice
- QUANTIFICATION AND STATISTICAL ANALYSIS

SUPPLEMENTAL INFORMATION

Supplemental information can be found online at https://doi.org/10.1016/j.cell. 2025.06.018.

Received: May 23, 2024 Revised: April 25, 2025 Accepted: June 13, 2025 Published: July 9, 2025

REFERENCES

- World Health Organization. (2024). Physical activity. https://www.who. int/news-room/fact-sheets/detail/physical-activity.
- Ligibel, J.A., Bohlke, K., May, A.M., Clinton, S.K., Demark-Wahnefried, W., Gilchrist, S.C., Irwin, M.L., Late, M., Mansfield, S., Marshall, T.F., et al. (2022). Exercise, Diet, and Weight Management During Cancer Treatment: ASCO Guideline. J. Clin. Oncol. 40, 2491–2507. https://doi. org/10.1200/JCO.22.00687.
- Campbell, K.L., Winters-Stone, K.M., Wiskemann, J., May, A.M., Schwartz, A.L., Courneya, K.S., Zucker, D.S., Matthews, C.E., Ligibel, J.A., Gerber, L.H., et al. (2019). Exercise Guidelines for Cancer Survivors: Consensus Statement from International Multidisciplinary Roundtable. Med. Sci. Sports Exerc. 51, 2375–2390. https://doi.org/10.1249/MSS. 000000000000002116.
- Rock, C.L., Thomson, C.A., Sullivan, K.R., Howe, C.L., Kushi, L.H., Caan, B.J., Neuhouser, M.L., Bandera, E.V., Wang, Y., Robien, K., et al. (2022). American Cancer Society nutrition and physical activity guideline for cancer survivors. CA Cancer J. Clin. 72, 230–262. https://doi.org/10.3322/caac.21719.
- Ashcraft, K.A., Peace, R.M., Betof, A.S., Dewhirst, M.W., and Jones, L.W. (2016). Efficacy and Mechanisms of Aerobic Exercise on Cancer Initiation, Progression, and Metastasis: A Critical Systematic Review of In Vivo Preclinical Data. Cancer Res. 76, 4032–4050. https://doi.org/10.1158/0008-5472.CAN-16-0887.
- Campbell, K.L., Winters-Stone, K.M., and Schmitz, K.H. (2023). We All Seem to Agree: Exercise Is Medicine in Medical Oncology. J. Clin. Oncol. 41, 147–148. https://doi.org/10.1200/JCO.22.01448.
- Schmitz, K.H., Campbell, A.M., Stuiver, M.M., Pinto, B.M., Schwartz, A. L., Morris, G.S., Ligibel, J.A., Cheville, A., Galvão, D.A., Alfano, C.M.,

- et al. (2019). Exercise is medicine in oncology: Engaging clinicians to help patients move through cancer. CA Cancer J. Clin. 69, 468–484. https://doi.org/10.3322/caac.21579.
- Kurz, E., Hirsch, C.A., Dalton, T., Shadaloey, S.A., Khodadadi-Jamayran, A., Miller, G., Pareek, S., Rajaei, H., Mohindroo, C., Baydogan, S., et al. (2022). Exercise-induced engagement of the IL-15/IL-15Ralpha axis promotes anti-tumor immunity in pancreatic cancer. Cancer Cell 40, 720–737. https://doi.org/10.1016/j.ccell.2022.05.006.
- Aoi, W., Naito, Y., Takagi, T., Tanimura, Y., Takanami, Y., Kawai, Y., Sakuma, K., Hang, L.P., Mizushima, K., Hirai, Y., et al. (2013). A novel myokine, secreted protein acidic and rich in cysteine (SPARC), suppresses colon tumorigenesis via regular exercise. Gut 62, 882–889. https://doi. org/10.1136/gutjnl-2011-300776.
- Gomes-Santos, I.L., Amoozgar, Z., Kumar, A.S., Ho, W.W., Roh, K., Talele, N.P., Curtis, H., Kawaguchi, K., Jain, R.K., and Fukumura, D. (2021). Exercise Training Improves Tumor Control by Increasing CD8+ T-cell Infiltration via CXCR3 Signaling and Sensitizes Breast Cancer to Immune Checkpoint Blockade. Cancer Immunol. Res. 9, 765–778. https://doi.org/10.1158/2326-6066.CIR-20-0499.
- Rundqvist, H., Veliça, P., Barbieri, L., Gameiro, P.A., Bargiela, D., Gojkovic, M., Mijwel, S., Reitzner, S.M., Wulliman, D., Ahlstedt, E., et al. (2020). Cytotoxic T-cells mediate exercise-induced reductions in tumor growth. eLife 9, e59996. https://doi.org/10.7554/eLife.59996.
- Savage, H., Pareek, S., Lee, J., Ballarò, R., Conterno Minussi, D., Hayek, K., Sadullozoda, M., Lochmann, B.S., McQuade, J.L., LaVoy, E.C., et al. (2023). Aerobic Exercise Alters the Melanoma Microenvironment and Modulates ERK5 S496 Phosphorylation. Cancer Immunol. Res. 11, 1168–1183. https://doi.org/10.1158/2326-6066.CIR-22-0465.
- Pedersen, L., Idorn, M., Olofsson, G.H., Lauenborg, B., Nookaew, I., Hansen, R.H., Johannesen, H.H., Becker, J.C., Pedersen, K.S., Dethlefsen, C., et al. (2016). Voluntary Running Suppresses Tumor Growth through Epinephrine- and IL-6-Dependent NK Cell Mobilization and Redistribution. Cell Metab. 23, 554–562. https://doi.org/10.1016/j. cmet.2016.01.011.
- Okamoto, T., Morino, K., Ugi, S., Nakagawa, F., Lemecha, M., Ida, S., Ohashi, N., Sato, D., Fujita, Y., and Maegawa, H. (2019). Microbiome potentiates endurance exercise through intestinal acetate production. Am. J. Physiol. Endocrinol. Metab. 316, E956–E966. https://doi.org/10.1152/aipendo.00510.2018.
- Himbert, C., Stephens, W.Z., Gigic, B., Hardikar, S., Holowatyj, A.N., Lin, T., Ose, J., Swanson, E., Ashworth, A., Warby, C.A., et al. (2022). Differences in the gut microbiome by physical activity and BMI among colorectal cancer patients. Am. J. Cancer Res. 12, 4789–4801.
- Estaki, M., Pither, J., Baumeister, P., Little, J.P., Gill, S.K., Ghosh, S., Ahmadi-Vand, Z., Marsden, K.R., and Gibson, D.L. (2016). Cardiorespiratory fitness as a predictor of intestinal microbial diversity and distinct metagenomic functions. Microbiome 4, 42. https://doi.org/10.1186/s40168-016-0189-7.
- Munukka, E., Ahtiainen, J.P., Puigbó, P., Jalkanen, S., Pahkala, K., Keskitalo, A., Kujala, U.M., Pietilä, S., Hollmén, M., Elo, L., et al. (2018). Six-Week Endurance Exercise Alters Gut Metagenome That Is not Reflected in Systemic Metabolism in Over-weight Women. Front. Microbiol. 9, 2323. https://doi.org/10.3389/fmicb.2018.02323.
- Liu, Y., Wang, Y., Ni, Y., Cheung, C.K.Y., Lam, K.S.L., Wang, Y., Xia, Z., Ye, D., Guo, J., Tse, M.A., et al. (2020). Gut Microbiome Fermentation Determines the Efficacy of Exercise for Diabetes Prevention. Cell Metab. 31, 77–91. https://doi.org/10.1016/j.cmet.2019.11.001.
- Suez, J., Zmora, N., Zilberman-Schapira, G., Mor, U., Dori-Bachash, M., Bashiardes, S., Zur, M., Regev-Lehavi, D., Ben-Zeev Brik, R., Federici, S., et al. (2018). Post-Antibiotic Gut Mucosal Microbiome Reconstitution Is Impaired by Probiotics and Improved by Autologous FMT. Cell 174, 1406–1423. https://doi.org/10.1016/j.cell.2018.08.047.
- Spencer, C.N., McQuade, J.L., Gopalakrishnan, V., McCulloch, J.A., Vetizou, M., Cogdill, A.P., Khan, M.A.W., Zhang, X., White, M.G., Peterson,



- C.B., et al. (2021). Dietary fiber and probiotics influence the gut microbiome and melanoma immunotherapy response. Science *374*, 1632–1640. https://doi.org/10.1126/science.aaz7015.
- Routy, B., Le Chatelier, E., Derosa, L., Duong, C.P.M., Alou, M.T., Daillère, R., Fluckiger, A., Messaoudene, M., Rauber, C., Roberti, M.P., et al. (2018). Gut microbiome influences efficacy of PD-1-based immunotherapy against epithelial tumors. Science 359, 91–97. https://doi.org/10.1126/science.aan3706.
- Simpson, R.C., Shanahan, E.R., Batten, M., Reijers, I.L.M., Read, M., Silva, I.P., Versluis, J.M., Ribeiro, R., Angelatos, A.S., Tan, J., et al. (2022). Diet-driven microbial ecology underpins associations between cancer immunotherapy outcomes and the gut microbiome. Nat. Med. 28, 2344–2352. https://doi.org/10.1038/s41591-022-01965-2.
- Ho, P.C., Meeth, K.M., Tsui, Y.C., Srivastava, B., Bosenberg, M.W., and Kaech, S.M. (2014). Immune-based antitumor effects of BRAF inhibitors rely on signaling by CD40L and IFNγ. Cancer Res. 74, 3205–3217. https://doi.org/10.1158/0008-5472.CAN-13-3461.
- Wang, J., Perry, C.J., Meeth, K., Thakral, D., Damsky, W., Micevic, G., Kaech, S., Blenman, K., and Bosenberg, M. (2017). UV-induced somatic mutations elicit a functional T cell response in the YUMMER1.7 mouse melanoma model. Pigment Cell Melanoma Res. 30, 428–435. https:// doi.org/10.1111/pcmr.12591.
- Liu, C., Yang, Y., Chen, C., Li, L., Li, J., Wang, X., Chu, Q., Qiu, L., Ba, Q., Li, X., and Wang, H. (2021). Publisher Correction: Environmental eustress modulates beta-ARs/CCL2 axis to induce anti-tumor immunity and sensitize immunotherapy against liver cancer in mice. Nat. Commun. 12, 6100. https://doi.org/10.1038/s41467-021-26376-8.
- Wennerberg, E., Lhuillier, C., Rybstein, M.D., Dannenberg, K., Rudqvist, N.P., Koelwyn, G.J., Jones, L.W., and Demaria, S. (2020). Exercise reduces immune suppression and breast cancer progression in a preclinical model. Oncotarget 11, 452–461. https://doi.org/10.18632/oncotarget.27464.
- Fransen, M.F., Schoonderwoerd, M., Knopf, P., Camps, M.G., Hawinkels, L.J., Kneilling, M., van Hall, T., and Ossendorp, F. (2018). Tumordraining lymph nodes are pivotal in PD-1/PD-L1 checkpoint therapy. JCI Insight 3, e124507. https://doi.org/10.1172/jci.insight.124507.
- Dammeijer, F., van Gulijk, M., Mulder, E.E., Lukkes, M., Klaase, L., van den Bosch, T., van Nimwegen, M., Lau, S.P., Latupeirissa, K., Schetters, S., et al. (2020). The PD-1/PD-L1-Checkpoint Restrains T cell Immunity in Tumor-Draining Lymph Nodes. Cancer Cell 38, 685–700. https://doi.org/10.1016/j.ccell.2020.09.001.
- Huang, Q., Wu, X., Wang, Z., Chen, X., Wang, L., Lu, Y., Xiong, D., Liu, Q., Tian, Y., Lin, H., et al. (2022). The primordial differentiation of tumor-specific memory CD8+ T cells as bona fide responders to PD-1/PD-L1 blockade in draining lymph nodes. Cell 185, 4049–4066. https://doi.org/10.1016/j.cell.2022.09.020.
- Routy, B., Jackson, T., Mählmann, L., Baumgartner, C.K., Blaser, M., Byrd, A., Corvaia, N., Couts, K., Davar, D., Derosa, L., et al. (2024). Melanoma and microbiota: Current understanding and future directions. Cancer Cell 42, 16–34. https://doi.org/10.1016/j.ccell.2023.12.003.
- Meisel, M., Hinterleitner, R., Pacis, A., Chen, L., Earley, Z.M., Mayassi, T., Pierre, J.F., Ernest, J.D., Galipeau, H.J., Thuille, N., et al. (2018). Microbial signals drive pre-leukaemic myeloproliferation in a Tet2-deficient host. Nature 557, 580–584. https://doi.org/10.1038/s41586-018-0125-z.
- Bender, M.J., McPherson, A.C., Phelps, C.M., Pandey, S.P., Laughlin, C. R., Shapira, J.H., Medina Sanchez, L., Rana, M., Richie, T.G., Mims, T.S., et al. (2023). Dietary tryptophan metabolite released by intratumoral Lactobacillus reuteri facilitates immune checkpoint inhibitor treatment. Cell 186, 1846–1862. https://doi.org/10.1016/j.cell.2023.03.011.
- Phelps, C.M., Shapira, J.H., Laughlin, C.R., and Meisel, M. (2023). Detection of viable commensal bacteria in murine melanoma tumors by culturomics. Star Protoc. 4, 102492. https://doi.org/10.1016/j.xpro.2023. 102492.

- Rahimikollu, J., Xiao, H., Rosengart, A., Rosen, A.B.I., Tabib, T., Zdinak, P.M., He, K., Bing, X., Bunea, F., Wegkamp, M., et al. (2024). SLIDE: Significant Latent Factor Interaction Discovery and Exploration across biological domains. Nat. Methods 21, 835–845. https://doi.org/10.1038/ s41592-024-02175-z.
- Li, S., Park, Y., Duraisingham, S., Strobel, F.H., Khan, N., Soltow, Q.A., Jones, D.P., and Pulendran, B. (2013). Predicting network activity from high throughput metabolomics. PLOS Comput. Biol. 9, e1003123. https://doi.org/10.1371/journal.pcbi.1003123.
- Shetty, S., and Varshney, U. (2021). Regulation of translation by one-carbon metabolism in bacteria and eukaryotic organelles. J. Biol. Chem. 296, 100088. https://doi.org/10.1074/jbc.REV120.011985.
- Pietzke, M., Meiser, J., and Vazquez, A. (2020). Formate metabolism in health and disease. Mol. Metab. 33, 23–37. https://doi.org/10.1016/j. molmet.2019.05.012.
- Fidelle, M., Rauber, C., Alves Costa Silva, C., Tian, A.L., Lahmar, I., de La Varende, A.M., Zhao, L., Thelemaque, C., Lebhar, I., Messaoudene, M., et al. (2023). A microbiota-modulated checkpoint directs immunosuppressive intestinal T cells into cancers. Science 380, eabo2296. https:// doi.org/10.1126/science.abo2296.
- Zheng, Y., and Cantley, L.C. (2019). Toward a better understanding of folate metabolism in health and disease. J. Exp. Med. 216, 253–266. https://doi.org/10.1084/jem.20181965.
- Nogal, A., Valdes, A.M., and Menni, C. (2021). The role of short-chain fatty acids in the interplay between gut microbiota and diet in cardiometabolic health. Gut Microbes 13, 1–24. https://doi.org/10.1080/ 19490976.2021.1897212.
- Brosnan, M.E., and Brosnan, J.T. (2016). Formate: The Neglected Member of One-Carbon Metabolism. Annu. Rev. Nutr. 36, 369–388. https://doi.org/10.1146/annurev-nutr-071715-050738.
- Ducker, G.S., and Rabinowitz, J.D. (2017). One-Carbon Metabolism in Health and Disease. Cell Metab. 25, 27–42. https://doi.org/10.1016/j. compt. 2016.08.000
- Zakharov, S., Kurcova, I., Navratil, T., Salek, T., Komarc, M., and Pelclova, D. (2015). Is the measurement of serum formate concentration useful in the diagnostics of acute methanol poisoning? A prospective study of 38 patients. Basic Clin. Pharmacol. Toxicol. 116, 445–451. https://doi.org/10.1111/bcpt.12338.
- 44. Hughes, E.R., Winter, M.G., Duerkop, B.A., Spiga, L., Furtado de Carvalho, T., Zhu, W., Gillis, C.C., Büttner, L., Smoot, M.P., Behrendt, C. L., et al. (2017). Microbial Respiration and Formate Oxidation as Metabolic Signatures of Inflammation-Associated Dysbiosis. Cell Host Microbe 21, 208–219. https://doi.org/10.1016/j.chom.2017.01.005.
- Douglas, G.M., Maffei, V.J., Zaneveld, J.R., Yurgel, S.N., Brown, J.R., Taylor, C.M., Huttenhower, C., and Langille, M.G.I. (2020). PICRUSt2 for prediction of metagenome functions. Nat. Biotechnol. 38, 685–688. https://doi.org/10.1038/s41587-020-0548-6.
- Pandey, S.P., Bender, M.J., McPherson, A.C., Phelps, C.M., Sanchez, L. M., Rana, M., Hedden, L., Sangani, K.A., Chen, L., Shapira, J.H., et al. (2022). Tet2 deficiency drives liver microbiome dysbiosis triggering Tc1 cell autoimmune hepatitis. Cell Host Microbe 30, 1003–1019. https://doi.org/10.1016/j.chom.2022.05.006.
- Lee, A.H., Rodriguez Jimenez, D.M., and Meisel, M. (2025). Limosilacto-bacillus reuteri a probiotic gut commensal with contextual impact on immunity. Gut Microbes 17, 2451088. https://doi.org/10.1080/19490976.2025.2451088.
- Furue, M. (2020). Regulation of Filaggrin, Loricrin, and Involucrin by IL-4, IL-13, IL-17A, IL-22, AHR, and NRF2: Pathogenic Implications in Atopic Dermatitis. Int. J. Mol. Sci. 21, 5382. https://doi.org/10.3390/ ijms21155382.
- Saw, C.L.L., Cintrón, M., Wu, T.Y., Guo, Y., Huang, Y., Jeong, W.S., and Kong, A.N.T. (2011). Pharmacodynamics of dietary phytochemical indoles I3C and DIM: Induction of Nrf2-mediated phase II drug





- metabolizing and antioxidant genes and synergism with isothiocyanates. Biopharm. Drug Dispos. 32, 289–300. https://doi.org/10.1002/bdd.759.
- Prochaska, H.J., and Talalay, P. (1988). Regulatory mechanisms of monofunctional and bifunctional anticarcinogenic enzyme inducers in murine liver. Cancer Res. 48, 4776–4782.
- Grishanova, A.Y., and Perepechaeva, M.L. (2022). Aryl Hydrocarbon Receptor in Oxidative Stress as a Double Agent and Its Biological and Therapeutic Significance. Int. J. Mol. Sci. 23, 6719. https://doi.org/10.3390/iims23126719.
- Ohl, K., and Tenbrock, K. (2021). Oxidative Stress in SLE T Cells, Is NRF2 Really the Target to Treat? Front. Immunol. 12, 633845. https://doi.org/ 10.3389/fimmu.2021.633845.
- 53. Xu, C., Huang, M.T., Shen, G., Yuan, X., Lin, W., Khor, T.O., Conney, A.H., and Kong, A.N.T. (2006). Inhibition of 7,12-dimethylbenz(a)anthracene-induced skin tumorigenesis in C57BL/6 mice by sulforaphane is mediated by nuclear factor E2-related factor 2. Cancer Res. 66, 8293–8296. https://doi.org/10.1158/0008-5472.CAN-06-0300.
- Ramos-Gomez, M., Dolan, P.M., Itoh, K., Yamamoto, M., and Kensler, T. W. (2003). Interactive effects of nrf2 genotype and oltipraz on benzo[a] pyrene-DNA adducts and tumor yield in mice. Carcinogenesis 24, 461–467. https://doi.org/10.1093/carcin/24.3.461.
- Solis, L.M., Behrens, C., Dong, W., Suraokar, M., Ozburn, N.C., Moran, C.A., Corvalan, A.H., Biswal, S., Swisher, S.G., Bekele, B.N., et al. (2010). Nrf2 and Keap1 abnormalities in non-small cell lung carcinoma and association with clinicopathologic features. Clin. Cancer Res. 16, 3743–3753. https://doi.org/10.1158/1078-0432.CCR-09-3352.
- Gharavi, N., and El-Kadi, A.O.S. (2005). tert-Butylhydroquinone is a novel aryl hydrocarbon receptor ligand. Drug Metab. Dispos. 33, 365–372. https://doi.org/10.1124/dmd.104.002253.
- FEEDAP (2014). Additives and Products or Substances used in Animal Feed. EFSA J. 12, 3898.
- Lee, Y.L., Xu, X., Wallenstein, S., and Chen, J. (2009). Gene expression profiles of the one-carbon metabolism pathway. J. Genet. Genomics 36, 277–282. https://doi.org/10.1016/S1673-8527(08)60115-0.
- Rubini, E., Baijens, I.M.M., Horánszky, A., Schoenmakers, S., Sinclair, K. D., Zana, M., Dinnyés, A., Steegers-Theunissen, R.P.M., and Rousian, M. (2021). Maternal One-Carbon Metabolism during the Periconceptional Period and Human Foetal Brain Growth: A Systematic Review. Genes (Basel) 12, 1634. https://doi.org/10.3390/genes12101634.
- Jamaluddin, M., Haas de Mello, A., Tapryal, N., Hazra, T.K., Garofalo, R. P., and Casola, A. (2022). NRF2 Regulates Cystathionine Gamma-Lyase Expression and Activity in Primary Airway Epithelial Cells Infected with Respiratory Syncytial Virus. Antioxidants (Basel) 11, 1582. https://doi. org/10.3390/antiox11081582.
- Vellers, H.L., Cho, H.Y., Gladwell, W., Gerrish, K., Santos, J.H., Ofman, G., Miller-DeGraff, L., Mahler, T.B., and Kleeberger, S.R. (2022). NRF2 Alters Mitochondrial Gene Expression in Neonate Mice Exposed to Hyperoxia. Antioxidants (Basel) 11, 760. https://doi.org/10.3390/antiox11040760.
- Xu, I.M.J., Lai, R.K.H., Lin, S.H., Tse, A.P.W., Chiu, D.K.C., Koh, H.Y., Law, C.T., Wong, C.M., Cai, Z., Wong, C.C.L., and Ng, I.O. (2016). Transketolase counteracts oxidative stress to drive cancer development. Proc. Natl. Acad. Sci. USA 113, E725–E734. https://doi.org/10.1073/pnas. 1508779113.
- Gao, L., Kumar, V., Vellichirammal, N.N., Park, S.Y., Rudebush, T.L., Yu, L., Son, W.M., Pekas, E.J., Wafi, A.M., Hong, J., et al. (2020). Functional, proteomic and bioinformatic analyses of Nrf2- and Keap1- null skeletal muscle. J. Physiol. 598, 5427–5451. https://doi.org/10.1113/JP280176.
- Pham, A.T., Ghilardi, A.F., and Sun, L. (2023). Recent advances in the development of RIPK2 modulators for the treatment of inflammatory diseases. Front. Pharmacol. 14, 1127722. https://doi.org/10.3389/fphar. 2023.1127722.

- Aydemir, T.B., Liuzzi, J.P., McClellan, S., and Cousins, R.J. (2009). Zinc transporter ZIP8 (SLC39A8) and zinc influence IFN-gamma expression in activated human T cells. J. Leukoc. Biol. 86, 337–348. https://doi.org/10. 1189/jib.1208759.
- Ojanen, M.J.T., Caro, F.M., Aittomäki, S., Ploquin, M.J., Ortutay, Z., Pekkarinen, M., Kesseli, J., Vähätupa, M., Määttä, J., Nykter, M., et al. (2023).
 FURIN regulates cytotoxic T-lymphocyte effector function and memory cell transition in mice. Eur. J. Immunol. 53, e2250246. https://doi.org/ 10.1002/eji.202250246.
- 67. Navarro, J., Gozalbo-López, B., Méndez, A.C., Dantzer, F., Schreiber, V., Martínez, C., Arana, D.M., Farrés, J., Revilla-Nuin, B., Bueno, M.F., et al. (2017). PARP-1/PARP-2 double deficiency in mouse T cells results in faulty immune responses and T lymphomas. Sci. Rep. 7, 41962. https://doi.org/10.1038/srep41962.
- Valdor, R., Schreiber, V., Saenz, L., Martínez, T., Muñoz-Suano, A., Dominguez-Villar, M., Ramírez, P., Parrilla, P., Aguado, E., García-Cózar, F., and Yelamos, J. (2008). Regulation of NFAT by poly(ADP-ribose) polymerase activity in T cells. Mol. Immunol. 45, 1863–1871. https://doi.org/10.1016/j.molimm.2007.10.044.
- Shaffer, M.H., Dupree, R.S., Zhu, P., Saotome, I., Schmidt, R.F., McClatchey, A.I., Freedman, B.D., and Burkhardt, J.K. (2009). Ezrin and moesin function together to promote T cell activation. J. Immunol. 182, 1021–1032. https://doi.org/10.4049/jimmunol.182.2.1021.
- Miyagawa, F., Zhang, H., Terunuma, A., Ozato, K., Tagaya, Y., and Katz, S.I. (2012). Interferon regulatory factor 8 integrates T-cell receptor and cytokine-signaling pathways and drives effector differentiation of CD8 T cells. Proc. Natl. Acad. Sci. USA 109, 12123–12128. https://doi.org/ 10.1073/pnas.1201453109.
- Holtschke, T., Löhler, J., Kanno, Y., Fehr, T., Giese, N., Rosenbauer, F., Lou, J., Knobeloch, K.P., Gabriele, L., Waring, J.F., et al. (1996). Immunodeficiency and chronic myelogenous leukemia-like syndrome in mice with a targeted mutation of the ICSBP gene. Cell 87, 307–317. https:// doi.org/10.1016/s0092-8674(00)81348-3.
- McGough, J.M., Yang, D., Huang, S., Georgi, D., Hewitt, S.M., Röcken, C., Tänzer, M., Ebert, M.P.A., and Liu, K. (2008). DNA methylation represses IFN-gamma-induced and signal transducer and activator of transcription 1-mediated IFN regulatory factor 8 activation in colon carcinoma cells. Mol. Cancer Res. 6, 1841–1851. https://doi.org/10.1158/ 1541-7786.MCR-08-0280.
- Keenan, A.B., Torre, D., Lachmann, A., Leong, A.K., Wojciechowicz, M. L., Utti, V., Jagodnik, K.M., Kropiwnicki, E., Wang, Z., and Ma'ayan, A. (2019). ChEA3: transcription factor enrichment analysis by orthogonal omics integration. Nucleic Acids Res. 47, W212–W224. https://doi.org/ 10.1093/nar/gkz446.
- Wang, R., Dillon, C.P., Shi, L.Z., Milasta, S., Carter, R., Finkelstein, D., McCormick, L.L., Fitzgerald, P., Chi, H., Munger, J., and Green, D.R. (2011). The transcription factor Myc controls metabolic reprogramming upon T lymphocyte activation. Immunity 35, 871–882. https://doi.org/ 10.1016/j.immuni.2011.09.021.
- Samten, B., Howard, S.T., Weis, S.E., Wu, S., Shams, H., Townsend, J. C., Safi, H., and Barnes, P.F. (2005). Cyclic AMP response element-binding protein positively regulates production of IFN-gamma by T cells in response to a microbial pathogen. J. Immunol. 174, 6357–6363. https://doi.org/10.4049/jimmunol.174.10.6357.
- Daniels, M.A., Luera, D., and Teixeiro, E. (2023). NF_KB signaling in T cell memory. Front. Immunol. 14, 1129191. https://doi.org/10.3389/fimmu. 2023.1129191.
- Louca, S., and Doebeli, M. (2018). Efficient comparative phylogenetics on large trees. Bioinformatics 34, 1053–1055. https://doi.org/10.1093/ bioinformatics/btx701.
- Henning, A.N., Roychoudhuri, R., and Restifo, N.P. (2018). Epigenetic control of CD8+ T cell differentiation. Nat. Rev. Immunol. 18, 340–356. https://doi.org/10.1038/nri.2017.146.



- Meraz, M.A., White, J.M., Sheehan, K.C., Bach, E.A., Rodig, S.J., Dighe, A.S., Kaplan, D.H., Riley, J.K., Greenlund, A.C., Campbell, D., et al. (1996). Targeted disruption of the Stat1 gene in mice reveals unexpected physiologic specificity in the JAK-STAT signaling pathway. Cell 84, 431–442. https://doi.org/10.1016/s0092-8674(00)81288-x.
- Dimberg, A., Kårehed, K., Nilsson, K., and Oberg, F. (2006). Inhibition of monocytic differentiation by phosphorylation-deficient Stat1 is associated with impaired expression of Stat2, ICSBP/IRF8 and C/EBPepsilon. Scand. J. Immunol. 64, 271–279. https://doi.org/10.1111/j.1365-3083. 2006.01827.x.
- Whitmire, J.K., Tan, J.T., and Whitton, J.L. (2005). Interferon-gamma acts directly on CD8+ T cells to increase their abundance during virus infection. J. Exp. Med. 201, 1053–1059. https://doi.org/10.1084/jem. 20041463.
- 82. Lee, K.A., Thomas, A.M., Bolte, L.A., Björk, J.R., de Ruijter, L.K., Armanini, F., Asnicar, F., Blanco-Miguez, A., Board, R., Calbet-Llopart, N., et al. (2022). Cross-cohort gut microbiome associations with immune checkpoint inhibitor response in advanced melanoma. Nat. Med. 28, 535–544. https://doi.org/10.1038/s41591-022-01695-5.
- Matson, V., Fessler, J., Bao, R., Chongsuwat, T., Zha, Y., Alegre, M.L., Luke, J.J., and Gajewski, T.F. (2018). The commensal microbiome is associated with anti-PD-1 efficacy in metastatic melanoma patients. Science 359, 104–108. https://doi.org/10.1126/science.aao3290.
- 84. Frankel, A.E., Coughlin, L.A., Kim, J., Froehlich, T.W., Xie, Y., Frenkel, E. P., and Koh, A.Y. (2017). Metagenomic Shotgun Sequencing and Unbiased Metabolomic Profiling Identify Specific Human Gut Microbiota and Metabolites Associated with Immune Checkpoint Therapy Efficacy in Melanoma Patients. Neoplasia 19, 848–855. https://doi.org/10.1016/j.neo.2017.08.004.
- Gopalakrishnan, V., Spencer, C.N., Nezi, L., Reuben, A., Andrews, M.C., Karpinets, T.V., Prieto, P.A., Vicente, D., Hoffman, K., Wei, S.C., et al. (2018). Gut microbiome modulates response to anti-PD-1 immunotherapy in melanoma patients. Science 359, 97–103. https://doi.org/10. 1126/science.aan4236
- McCulloch, J.A., Davar, D., Rodrigues, R.R., Badger, J.H., Fang, J.R., Cole, A.M., Balaji, A.K., Vetizou, M., Prescott, S.M., Fernandes, M.R., et al. (2022). Intestinal microbiota signatures of clinical response and immune-related adverse events in melanoma patients treated with anti-PD-1. Nat. Med. 28, 545–556. https://doi.org/10.1038/s41591-022-01698-2.
- Peters, B.A., Wilson, M., Moran, U., Pavlick, A., Izsak, A., Wechter, T., Weber, J.S., Osman, I., and Ahn, J. (2019). Relating the gut metagenome and metatranscriptome to immunotherapy responses in melanoma patients. Genome Med. 11, 61. https://doi.org/10.1186/s13073-019-0672-4.
- Ling, W., Lu, J., Zhao, N., Lulla, A., Plantinga, A.M., Fu, W., Zhang, A., Liu, H., Song, H., Li, Z., et al. (2022). Batch effects removal for microbiome data via conditional quantile regression. Nat. Commun. 13, 5418. https://doi.org/10.1038/s41467-022-33071-9.
- Beheshti, A., Chavanon, M.L., and Christiansen, H. (2020). Emotion dysregulation in adults with attention deficit hyperactivity disorder: a metaanalysis. BMC Psychiatry 20, 120. https://doi.org/10.1186/s12888-020-2442-7.
- Ternes, D., Tsenkova, M., Pozdeev, V.I., Meyers, M., Koncina, E., Atatri, S., Schmitz, M., Karta, J., Schmoetten, M., Heinken, A., et al. (2023). Author Correction: The gut microbial metabolite formate exacerbates colorectal cancer progression. Nat. Metab. 5, 1638. https://doi.org/10. 1038/s42255-023-00898-5.
- Rowe, J.H., Elia, I., Shahid, O., Gaudiano, E.F., Sifnugel, N.E., Johnson, S., Reynolds, A.G., Fung, M.E., Joshi, S., LaFleur, M.W., et al. (2023). Formate Supplementation Enhances Antitumor CD8+ T-cell Fitness and Efficacy of PD-1 Blockade. Cancer Discov. 13, 2566–2583. https://doi.org/10.1158/2159-8290.CD-22-1301.
- Xu, X., Chen, Z., Bartman, C.R., Xing, X., Olszewski, K., and Rabinowitz,
 J.D. (2023). One-carbon unit supplementation fuels tumor-infiltrating

- T cells and augments checkpoint blockade. Preprint at bioRxiv, 2023. 11.01.565193. https://doi.org/10.1101/2023.11.01.565193.
- Renken, S., Nakajima, T., Magalhaes, I., Mattsson, J., Lundqvist, A., Arnér, E.S.J., Kiessling, R., and Wickström, S.L. (2022). Targeting of Nrf2 improves antitumoral responses by human NK cells, TIL and CAR T cells during oxidative stress. J. Immunother. Cancer 10, e004458. https://doi.org/10.1136/jitc-2021-004458.
- Davar, D., Wang, H., Chauvin, J.M., Pagliano, O., Fourcade, J.J., Ka, M., Menna, C., Rose, A., Sander, C., Borhani, A.A., et al. (2018). Phase Ib/II Study of Pembrolizumab and Pegylated-Interferon Alfa-2b in Advanced Melanoma. J. Clin. Oncol. 36, JCO1800632. https://doi.org/10.1200/ JCO.18.00632.
- Draxler, A., Franzke, B., Kelecevic, S., Maier, A., Pantic, J., Srienc, S., Cellnigg, K., Solomon, S.M., Zötsch, C., Aschauer, R., et al. (2023). The influence of vitamin D supplementation and strength training on health biomarkers and chromosomal damage in community-dwelling older adults. Redox Biol. 61, 102640. https://doi.org/10.1016/j.redox.2023. 102640.
- Sivan, A., Corrales, L., Hubert, N., Williams, J.B., Aquino-Michaels, K., Earley, Z.M., Benyamin, F.W., Lei, Y.M., Jabri, B., Alegre, M.L., et al. (2015). Commensal Bifidobacterium promotes antitumor immunity and facilitates anti-PD-L1 efficacy. Science 350, 1084–1089. https://doi. org/10.1126/science.aac4255.
- 97. Gillis, C.C., Hughes, E.R., Spiga, L., Winter, M.G., Zhu, W., Furtado de Carvalho, T., Chanin, R.B., Behrendt, C.L., Hooper, L.V., Santos, R.L., and Winter, S.E. (2018). Dysbiosis-Associated Change in Host Metabolism Generates Lactate to Support Salmonella Growth. Cell Host Microbe 23, 54–64. https://doi.org/10.1016/j.chom.2017.11.006.
- Pal, D., Venkova-Canova, T., Srivastava, P., and Chattoraj, D.K. (2005).
 Multipartite regulation of rctB, the replication initiator gene of Vibrio cholerae chromosome II. J. Bacteriol. 187, 7167–7175. https://doi.org/10.1128/JB.187.21.7167-7175.2005.
- Schneider, D., Faure, D., Noirclerc-Savoye, M., Barrière, A.C., Coursange, E., and Blot, M. (2000). A broad-host-range plasmid for isolating mobile genetic elements in gram-negative bacteria. Plasmid 44, 201–207. https://doi.org/10.1006/plas.2000.1483.
- 100. Eaves-Pyles, T., Allen, C.A., Taormina, J., Swidsinski, A., Tutt, C.B., Jezek, G.E., Islas-Islas, M., and Torres, A.G. (2008). Escherichia coli isolated from a Crohn's disease patient adheres, invades, and induces inflammatory responses in polarized intestinal epithelial cells. Int. J. Med. Microbiol. 298, 397–409. https://doi.org/10.1016/j.ijmm.2007.05.011.
- Bray, N.L., Pimentel, H., Melsted, P., and Pachter, L. (2016). Nearoptimal probabilistic RNA-seq quantification. Nat. Biotechnol. 34, 525–527. https://doi.org/10.1038/nbt.3519.
- Pimentel, H., Bray, N.L., Puente, S., Melsted, P., and Pachter, L. (2017).
 Differential analysis of RNA-seq incorporating quantification uncertainty.
 Nat. Methods 14, 687–690. https://doi.org/10.1038/nmeth.4324.
- 103. Bolyen, E., Rideout, J.R., Dillon, M.R., Bokulich, N.A., Abnet, C.C., Al-Ghalith, G.A., Alexander, H., Alm, E.J., Arumugam, M., Asnicar, F., et al. (2019). Reproducible, interactive, scalable and extensible microbiome data science using QIIME 2. Nat. Biotechnol. 37, 852–857. https://doi.org/10.1038/s41587-019-0209-9.
- 104. Callahan, B.J., McMurdie, P.J., Rosen, M.J., Han, A.W., Johnson, A.J.A., and Holmes, S.P. (2016). DADA2: High-resolution sample inference from Illumina amplicon data. Nat. Methods 13, 581–583. https://doi.org/10.1038/nmeth.3869.
- 105. Quast, C., Pruesse, E., Yilmaz, P., Gerken, J., Schweer, T., Yarza, P., Peplies, J., and Glöckner, F.O. (2013). The SILVA ribosomal RNA gene database project: improved data processing and web-based tools. Nucleic Acids Res. 41, D590–D596. https://doi.org/10.1093/nar/gks1219.
- 106. Price, M.N., Dehal, P.S., and Arkin, A.P. (2010). FastTree 2-approximately maximum-likelihood trees for large alignments. PLoS One 5, e9490. https://doi.org/10.1371/journal.pone.0009490.





- Barbera, P., Kozlov, A.M., Czech, L., Morel, B., Darriba, D., Flouri, T., and Stamatakis, A. (2019). EPA-ng: Massively Parallel Evolutionary Placement of Genetic Sequences. Syst. Biol. 68, 365–369. https://doi.org/ 10.1093/sysbio/syy054.
- 108. Caspi, R., Billington, R., Fulcher, C.A., Keseler, I.M., Kothari, A., Krummenacker, M., Latendresse, M., Midford, P.E., Ong, Q., Ong, W.K., et al. (2018). The MetaCyc database of metabolic pathways and enzymes. Nucleic Acids Res. 46, D633–D639. https://doi.org/10.1093/nar/gkx935.
- Dhariwal, A., Chong, J., Habib, S., King, I.L., Agellon, L.B., and Xia, J. (2017). MicrobiomeAnalyst: a web-based tool for comprehensive statistical, visual and meta-analysis of microbiome data. Nucleic Acids Res. 45, W180–W188. https://doi.org/10.1093/nar/gkx295.
- Lozupone, C.A., Hamady, M., Kelley, S.T., and Knight, R. (2007). Quantitative and qualitative beta diversity measures lead to different insights into factors that structure microbial communities. Appl. Environ. Microbiol. 73, 1576–1585. https://doi.org/10.1128/AEM.01996-06.
- Love, M.I., Huber, W., and Anders, S. (2014). Moderated estimation of fold change and dispersion for RNA-seq data with DESeq2. Genome Biol. 15. 550. https://doi.org/10.1186/s13059-014-0550-8.
- 112. Yang, C., Mai, J., Cao, X., Burberry, A., Cominelli, F., and Zhang, L. (2023). ggpicrust2: an R package for PICRUSt2 predicted functional profile analysis and visualization. Bioinformatics 39, btad470. https://doi.org/10.1093/bioinformatics/btad470.
- 113. Choucair, I., Nemet, I., Li, L., Cole, M.A., Skye, S.M., Kirsop, J.D., Fischbach, M.A., Gogonea, V., Brown, J.M., Tang, W.H.W., and Hazen, S.L. (2020). Quantification of bile acids: a mass spectrometry platform for studying gut microbe connection to metabolic diseases. J. Lipid Res. 61, 159–177. https://doi.org/10.1194/jir.RA119000311.
- 114. Bolger, A.M., Lohse, M., and Usadel, B. (2014). Trimmomatic: a flexible trimmer for Illumina sequence data. Bioinformatics 30, 2114–2120. https://doi.org/10.1093/bioinformatics/btu170.
- Langmead, B., and Salzberg, S.L. (2012). Fast gapped-read alignment with Bowtie 2. Nat. Methods 9, 357–359. https://doi.org/10.1038/ nmeth.1923.
- 116. Li, D., Luo, R., Liu, C.M., Leung, C.M., Ting, H.F., Sadakane, K., Yamashita, H., and Lam, T.W. (2016). MEGAHIT v1.0: A fast and scalable metagenome assembler driven by advanced methodologies and community practices. Methods 102, 3–11. https://doi.org/10.1016/j.ymeth.2016.02.020.
- Wood, D.E., Lu, J., and Langmead, B. (2019). Improved metagenomic analysis with Kraken 2. Genome Biol. 20, 257. https://doi.org/10.1186/ s13059-019-1891-0.
- Seemann, T. (2014). Prokka: rapid prokaryotic genome annotation. Bioinformatics 30, 2068–2069. https://doi.org/10.1093/bioinformatics/ btu153.
- 119. Truong, D.T., Franzosa, E.A., Tickle, T.L., Scholz, M., Weingart, G., Pasolli, E., Tett, A., Huttenhower, C., and Segata, N. (2015). MetaPhlAn2 for enhanced metagenomic taxonomic profiling. Nat. Methods 12, 902–903. https://doi.org/10.1038/nmeth.3589.
- Beghini, F., McIver, L.J., Blanco-Míguez, A., Dubois, L., Asnicar, F., Maharjan, S., Mailyan, A., Manghi, P., Scholz, M., Thomas, A.M., et al. (2021). Integrating taxonomic, functional, and strain-level profiling of diverse microbial communities with bioBakery 3. eLife 10, e65088. https://doi.org/10.7554/eLife.65088.
- Buchfink, B., Xie, C., and Huson, D.H. (2015). Fast and sensitive protein alignment using DIAMOND. Nat. Methods 12, 59–60. https://doi.org/10. 1038/nmeth 3176
- 122. Ye, Y., and Doak, T.G. (2009). A parsimony approach to biological pathway reconstruction/inference for genomes and metagenomes. PLoS Comput. Biol. 5, e1000465. https://doi.org/10.1371/journal.pcbi. 1000465.

- 123. Shaiber, A., Willis, A.D., Delmont, T.O., Roux, S., Chen, L.X., Schmid, A. C., Yousef, M., Watson, A.R., Lolans, K., Esen, Ö.C., et al. (2020). Functional and genetic markers of niche partitioning among enigmatic members of the human oral microbiome. Genome Biol. 21, 292. https://doi.org/10.1186/s13059-020-02195-w.
- 124. Eren, A.M., Morrison, H.G., Lescault, P.J., Reveillaud, J., Vineis, J.H., and Sogin, M.L. (2015). Minimum entropy decomposition: unsupervised oligotyping for sensitive partitioning of high-throughput marker gene sequences. ISME J. 9, 968–979. https://doi.org/10.1038/ismej.2014.195.
- 125. Eren, A.M., Kiefl, E., Shaiber, A., Veseli, I., Miller, S.E., Schechter, M.S., Fink, I., Pan, J.N., Yousef, M., Fogarty, E.C., et al. (2021). Community-led, integrated, reproducible multi-omics with anvi'o. Nat. Microbiol. 6, 3–6. https://doi.org/10.1038/s41564-020-00834-3.
- 126. Eren, A.M., Vineis, J.H., Morrison, H.G., and Sogin, M.L. (2013). A filtering method to generate high quality short reads using illumina paired-end technology. PLoS One 8, e66643. https://doi.org/10.1371/journal.pone. 0066643.
- 127. Minoche, A.E., Dohm, J.C., and Himmelbauer, H. (2011). Evaluation of genomic high-throughput sequencing data generated on Illumina HiSeq and genome analyzer systems. Genome Biol. 12, R112. https://doi.org/ 10.1186/gb-2011-12-11-r112.
- 128. Li, D., Liu, C.M., Luo, R., Sadakane, K., and Lam, T.W. (2015). MEGAHIT: an ultra-fast single-node solution for large and complex metagenomics assembly via succinct de Bruijn graph. Bioinformatics 31, 1674–1676. https://doi.org/10.1093/bioinformatics/btv033.
- 129. Hyatt, D., Chen, G.L., Locascio, P.F., Land, M.L., Larimer, F.W., and Hauser, L.J. (2010). Prodigal: prokaryotic gene recognition and translation initiation site identification. BMC Bioinformatics 11, 119. https:// doi.org/10.1186/1471-2105-11-119.
- Campbell, J.H., O'Donoghue, P., Campbell, A.G., Schwientek, P., Sczyrba, A., Woyke, T., Söll, D., and Podar, M. (2013). UGA is an additional glycine codon in uncultured SR1 bacteria from the human microbiota. Proc. Natl. Acad. Sci. USA 110, 5540–5545. https://doi.org/10.1073/pnas.1303090110.
- 131. Rinke, C., Schwientek, P., Sczyrba, A., Ivanova, N.N., Anderson, I.J., Cheng, J.F., Darling, A., Malfatti, S., Swan, B.K., Gies, E.A., et al. (2013). Insights into the phylogeny and coding potential of microbial dark matter. Nature 499, 431–437. https://doi.org/10.1038/nature12352.
- Eddy, S.R. (2011). Accelerated Profile HMM Searches. PLOS Comput. Biol. 7, e1002195. https://doi.org/10.1371/journal.pcbi.1002195.
- 133. Tatusov, R.L., Fedorova, N.D., Jackson, J.D., Jacobs, A.R., Kiryutin, B., Koonin, E.V., Krylov, D.M., Mazumder, R., Mekhedov, S.L., Nikolskaya, A.N., et al. (2003). The COG database: an updated version includes eukaryotes. BMC Bioinformatics 4, 41. https://doi.org/10.1186/1471-2105-4-41.
- 134. Aramaki, T., Blanc-Mathieu, R., Endo, H., Ohkubo, K., Kanehisa, M., Goto, S., and Ogata, H. (2020). KofamKOALA: KEGG Ortholog assignment based on profile HMM and adaptive score threshold. Bioinformatics 36, 2251–2252. https://doi.org/10.1093/bioinformatics/btz859.
- 135. Kanehisa, M., and Goto, S. (2000). KEGG: kyoto encyclopedia of genes and genomes. Nucleic Acids Res. 28, 27–30. https://doi.org/10.1093/ page/28.1.27
- Danecek, P., Bonfield, J.K., Liddle, J., Marshall, J., Ohan, V., Pollard, M. O., Whitwham, A., Keane, T., McCarthy, S.A., Davies, R.M., and Li, H. (2021). Twelve years of SAMtools and BCFtools. GigaScience 10, giab008. https://doi.org/10.1093/gigascience/giab008.
- 137. Alneberg, J., Bjarnason, B.S., de Bruijn, I., Schirmer, M., Quick, J., Ijaz, U. Z., Lahti, L., Loman, N.J., Andersson, A.F., and Quince, C. (2014). Binning metagenomic contigs by coverage and composition. Nat. Methods 11, 1144–1146. https://doi.org/10.1038/nmeth.3103.



STAR*METHODS

KEY RESOURCES TABLE

REAGENT or RESOURCE	SOURCE	IDENTIFIER
Antibodies		
anti-Mouse CD16/CD32 (Mouse BD Fc Block™, Rat, Clone 2.4G2) unconjugated	BD Biosciences	Cat # 553142; RRID: AB_394657
Anti-Mouse CD45 monoclonal antibody (Rat, Clone 30-F11), Brilliant Violet 480 conjugated	BD Biosciences	Cat # 566095; RRID: AB_2739499
Anti-mouse CD45 monoclonal antibody (Rat, Clone 30-F11), APC-Cy™7 conjugated	BD Biosciences	Cat # 557659; RRID: AB_396774
Anti-mouse CD45 monoclonal antibody (Rat, Clone 30-F11), BUV 395 conjugated	BD Biosciences	Cat # 564279; RRID: AB_2651134
Anti-mouse TCRβ monoclonal antibody (Armenian hamster, Clone H57-597), Alexa Fluor® 700 conjugated	BD Biosciences	Cat # 560705; RRID: AB_1727573
Anti-mouse TCR $_{\gamma}$ δ monoclonal antibody Armenian Hamster, Clone UC7-13D5), -ITC conjugated	BioLegend	Cat # 107504; RRID: AB_313313
Anti-mouse CD4 monoclonal antibody Rat, Clone GK1.5), BUV 395 conjugated	BD Biosciences	Cat # 563790; RRID: AB_2738426
Anti-mouse CD4 monoclonal antibody Rat, Clone GK1.5), Brilliant Violet 650 conjugated	BD Biosciences	Cat # 563232; RRID: AB_2738083
Anti-mouse CD8α monoclonal antibody (Rat, Clone 53-6.7), Brilliant Violet 570 conjugated	BioLegend	Cat # 100740; RRID: AB_2563055
Anti-Mouse CD8α monoclonal antibody (Rat, Clone 53-6.7), BUV 737 conjugated	BD Biosciences	Cat # 612759; RRID: AB_2870090
Anti-Mouse CD279 (PD-1) monoclonal antibody (Armenian Hamster, Clone J43), Brilliant Violet 786 conjugated	BD Biosciences	Cat # 744548; RRID: AB_2742319
Anti-Mouse CD90.1 (Thy-1.1) monoclonal antibody (Rat, Clone HIS51), eFluor TM 450 conjugated	Invitrogen	Cat # 48-0900-82; RRID: AB_1272254
Anti-Mouse CD90.2 (Thy-1.2) monoclonal antibody (Rat, Clone 53-2.1), BUV 563 conjugated	BD Biosciences	Cat # 741213; RRID: AB_2870768
anti-Mouse I-A/I-E (MHC II) monoclonal antibody (Rat, Clone M5/114.15.2), BUV 496 conjugated	BD Biosciences	Cat # 750281; RRID: AB_2874472
Anti-Mouse I-A/I-E (MHC II) monoclonal antibody (Rat, Clone M5/114.15.2), FITC conjugated	Thermo Fisher Scientific	Cat # 11-5321-82; RRID: AB_465232
Anti-mouse CD11c monoclonal antibody Hamster, Clone N418), FITC conjugated	BioLegend	Cat # 117306; RRID: AB_313775
Anti-mouse CD11c monoclonal antibody Armenian hamster, Clone N418), Brilliant Violet 421 conjugated	BD Biosciences	Cat # 565452; RRID: AB_2744278
Anti-mouse CD11b monoclonal antibody Rat, Clone M1/70), APC-eFluor 780 conjugated	eBioscience	Cat # 47-0112-80; RRID: AB_1603193
Anti-mouse CD11b monoclonal antibody Rat, Clone M1/70), BUV 805 conjugated	BD Biosciences	Cat # 741934; RRID: AB_2871246
Anti-mouse F4/80 monoclonal antibody Rat, Clone BM8), PE-Cyanine5 conjugated	eBioscience	Cat # 15-4801-80; RRID: AB_468798

(Continued on next page)





Continued		
REAGENT or RESOURCE	SOURCE	IDENTIFIER
Anti-Mouse Gr1 monoclonal antibody (Rat, Clone 3C7), PerCP-Cy5.5 conjugated	BD Biosciences	Cat # 552093; RRID: AB_394334
Anti-mouse NK1.1 monoclonal antibody Rat, Clone PK136), Brilliant Violet 786 conjugated	BD Biosciences	Cat # 568224; RRID: AB_2916852
Anti-mouse IFN-gamma monoclonal antibody Rat, Clone XMG1.2), Brilliant Violet 605 conjugated	BioLegend	Cat # 505839; RRID: AB_2561438
Anti-mouse IFN-gamma monoclonal antibody Rat, Clone XMG1.2), PE-Cy7 conjugated	Thermo Fisher Scientific	Cat # 25-7311-41; RRID: AB_2798432
Anti-mouse FoxP3 monoclonal antibody Rat, Clone FJK-16s), eFluor 450 conjugated	Thermo Fisher Scientific	Cat # 48-5773-82; RRID: AB_1518812
Anti-mouse Foxp3 monoclonal antibody Rat, Clone FJK-16s), FITC conjugated	eBioscience	Cat # 11-5773-82; RRID: AB_465243
Anti-mouse Granzyme B monoclonal antibody (Rat, Clone NGZB), PE conjugated	eBioscience	Cat # 12-8898-80; RRID: AB_1087078
Anti-mouse Ki67 monoclonal antibody Rat, Clone SolA15), PE-eFluor 610 conjugated	eBioscience	Cat # 61-5698-82; RRID: AB_2574620
Anti-mouse TNF-alpha monoclonal antibody (Rat, Clone MP6-XT22), APC conjugated	BioLegend	Cat # 506308; RRID: AB_315429
Anti-mouse Tbet monoclonal antibody Mouse, Clone 4B10), Brilliant Violet 421 conjugated	BioLegend	Cat # 644832; RRID: AB_2686976
Anti-mouse Eomesodermin (EOMES) monoclonal antibody (Rat, Clone Dan11mag), Alexa Fluor™ 488 conjugated	Invitrogen	Cat # 53-4875-82; RRID: AB_1085426
nVivoMAb anti-mouse CD8α (Clone 2.43)	BioXCell	Cat # BE0061; RRID: AB_1125541
nVivoMAb anti-mouse CD4 (Clone GK1.5)	BioXCell	Cat # BE0003-1; RRID: AB_1107636
nVivoMAb rat IgG2b isotype control (Clone LTF-2)	BioXCell	Cat # BE0090; RRID: AB_1107780
nVivoMAb anti-mouse PD-L1	BioXCell	Cat # BE0101; RRID: AB_10949073
Biotin anti-mouse CD45 antibody (Clone 30-F11)	BioLegend	Cat # 103104; RRID: AB_312969
Biotin anti-mouse CD8 antibody (Clone 53-6.7)	BioLegend	Cat # 100703; RRID: AB_312742
Anti-mouse CD3e monoclonal antibody Armenian hamster, Clone 145-2C11), unconjugated	BD Biosciences	Cat # 553057; RRID: AB_394590
Anti-mouse CD28 monoclonal antibody Syrian Hamster, Clone 37.51), unconjugated	BD Biosciences	Cat # 553294; RRID: AB_394763
Chemicals, peptides, and recombinant proteins		
Zombie NIR™ Fixable Viability Kit	BioLegend	Cat # 423105
Super Bright Complete Staining Buffer	eBioscience	Cat # SB-4401-75
Horseradish Peroxidase-conjugated streptavidin	Jackson Immuno Research	Cat # 016-030-084; RRID: AB_233723
Proteinase K Solution	Invitrogen	Cat # 25530049
Taq™ Universal SYBR® Green Supermix	Bio-Rad	Cat # 1725125
GolgiStop™	BD Biosciences	Cat # 554724
GolgiPlug™	BD Biosciences	Cat # 555029
Phorbol myristate acetate (PMA)	Sigma-Aldrich	Cat # P1585
onomycin calcium salt	Sigma-Aldrich	Cat # 10634
Mouse Erythrocyte Lysing Kit	R & D Systems	Cat # WL2000
Percoll TM	Thermo Fisher Scientific	Cat # 45-001-747
RPMI 1640	Thermo Fisher Scientific	Cat # MT10040CV
DMEM	Gibco TM	Cat # 11-995-065
Penicillin-Streptomycin-Glutamine	Gibco TM	Cat # 10-378-016
Non-Essential Amino Acid Solution	Sigma-Aldrich	Cat # M7145
Collagenase IV	Worthington Biochemical	Cat # LS004189

(Continued on next page)





Continued				
REAGENT or RESOURCE	SOURCE	IDENTIFIER		
Sodium Formate	Fisher Scientific	Cat # S648-500		
AHR inhibitor (CH-223191)	Sigma-Aldrich	Cat # C8124		
Fert-butylhydroquinone (TBHQ)	Sigma-Aldrich	Cat # 112941-5G		
NRF2 inhibitor (ML385)	Sigma-Aldrich	Cat # SML1833		
RNAprotect™	Qiagen	Cat # 76106		
DNase I	Roche	Cat # 10104159001		
Cooked Meat Medium	Fisher Scientific	Cat # DF0267-17-9		
Reinforced Clostridial Medium	Thermo Fisher Scientific	Cat # CM0149B		
deMann Rosa Sharpe Medium	Thermo Fisher Scientific	Cat # CM0359B		
Brain Heart Infusion Medium	Thermo Fisher Scientific	Cat # CM1135B		
BD Difco Dehydrated Culture Media: LB Broth, Miller (Luria-Bertani)	Fisher Scientific	Cat # DF0446-17-3		
Defibrinated Sheep Blood	HemoStat Laboratories	Cat # DSB050		
Gentamicin	Sigma-Aldrich	Cat # G1914-5G		
Metronidazole	Sigma-Aldrich	Cat # M3761-25G		
Colistin	Sigma-Aldrich	Cat # C4461-1G		
Kanamycin	Fisher Scientific	Cat # 11-815-024		
/ancomycin	Sigma-Aldrich	Cat # V2002		
Normocin	InvivoGen	Cat # ant-nr-1		
Zeocin	InvivoGen	Cat # ant-zn-05		
Chloramphenicol	Sigma-Aldrich	Cat # C3175		
Hygromycin B	InvivoGen	Cat # ant-hg-1		
QUANTI-Luc™	InvivoGen	Cat # rep-qlc1		
Recombinant Mouse IL-12	BioLegend	Cat # 577002		
Recombinant Human IL-2	PeproTech	Cat # 200-02		
Critical commercial assays	•			
FoxP3 Transcription Factor Staining Kit	eBioscience	Cat # 00-5523-00		
EasySep™ Mouse Naïve CD8 T cell Isolation Kit	STEMCELL	Cat # 18958		
Fast DNA Stool Mini Kit	Qiagen	Cat # 51604		
RNeasy Plus Mini Kit	Qiagen	Cat # 74136		
Script™ cDNA Synthesis Kit	Bio-Rad	Cat # 1708891		
CCK-8	ApexBio	Cat # K1018		
Mouse Folic acid.FA Elisa Kit	AFG Scientific	EK730149		
Experimental models: Cell lines				
BRAF ^{V600E} (YUMM1.7) cell line	ATCC	Cat # CRL-3362		
B16-F10 cell line	ATCC	Cat # CRL-6475		
MC-38 cell line	Kerafast	Cat # ENH204-FP		
EL-4 cell line	ATCC	Cat # TIB-39		
316-OVA cell line	Provided by M. Shlomchik	N/A		
HT29-Lucia™ AhR reporter cell line	Invivogen	Cat # ht2l-ahr		
HEK 293 ΔNRF2/ARE Nrf2 reporter cell line	Signosis	Cat # SL-0042		
Experimental models: Organisms/strains	3	7 day 11 day 12 day		
Mouse: B6.C57BL/6J	lackeon Laboratory	Stock No. 000664		
viouse: B6.C5/BL/6J Mouse: B6.Cg- <i>Rag2^{tm1.1Cgn}/J</i> (Rag ^{-/-})	Jackson Laboratory	Stock No: 000664		
viouse: B6.Ug- <i>Hag2</i> /J (Hag↑) Mouse: B6.129X1-Nfe212 ^{tm1Ywk} /J (Nrf2 ^{-/-})	Provided by M. Shlomchik Jackson Laboratory	N/A Stock No: 017000		
Wouse: B6.129X1-NIe212 /J (NI121) Mouse: B6.Cg-Thy1a/CyTg(TcraTcrb)8Rest/J (pmel+)	Jackson Laboratory Jackson Laboratory	Stock No: 017009 Stock No: 005023		
viouse. Do.Ou-111v1 /Ov1u(1018101D)0NeSt/J (DITIEI+)	Jackson Laboratory	3100k NO. 003023		

(Continued on next page)





Continued				
REAGENT or RESOURCE	SOURCE	IDENTIFIER		
Mouse: B6. <i>Ahr</i> ^{fl} CD8a Cre (B6. <i>AhR</i> ^{tm3.1Bra} /J x B6.C57BL/6J-Tg(CD8a*-cre)B8Asin/J x)	Jackson Laboratory	Stock No: 006203 x Stock No: 008766		
Mouse: B6. <i>Nrf2</i> ^{fl} CD8a Cre (B6. C57BL/6-Nfe2l2 ^{tm1.1Sred} /SbisJ x B6.C57BL/6J-Tg(CD8a*-cre)B8Asin/J x)	Jackson Laboratory	Stock No: 025433 x Stock No: 008766		
Oligonucleotides				
Primers for qRT-PCR, qPCR, 16S	Table S6	N/A		
Software and algorithms				
SLIDE	N/A	N/A		
QIIME2 (version 2023.7)	N/A	N/A		
SoftMax Pro 3.0.7 Software	SpectraMax® i3x	N/A		
X-PAD Software	Ugo Basile	N/A		
CFX Maestro	Bio-Rad	N/A		
Ingenuity Pathway Analysis (IPA)	Qiagen	N/A		
GraphPad Prism 10	GraphPad Software	N/A		
FlowJo 10.8.1	Tree Star	N/A		
Adobe Illustrator	Adobe	N/A		
BioRender	BioRender	N/A		
Actimetrics ClockLab Wireless Collection System	Lafayette Instrument	Cat # AM1-CW01		
ChEA3 TFEA tool (ENCODE-CHIP-SEQ)	N/A	N/A		
Other				
Rodent Treadmill	Ugo Basile	Cat # 47300		
Actimetrics Wireless Low-profile Running Wheel	Lafayette Instrument	Cat # ACT-557-WLP		
Actimetrics Wireless USB Gateway	Lafayette Instrument	Cat # ACT-557W-0		

EXPERIMENTAL MODEL AND STUDY PARTICIPANT DETAILS

Melanoma patient serum samples

Study design, baseline clinical and demographic (age, sex, race) characteristics, assessments and definition of endpoints of a cohort of advanced stage IV melanoma patients was recently described. Briefly, clinical data and sera of advanced stage IV melanoma patients that either responded (referred to as responders (R)) = partial response or complete response, n = 14) or failed to respond (referred to as non-responders (NR) = stable disease or progressive disease, n = 18) to combinatorial IFN α and α PD1 were used in this study (ClinialTrials.gov identifier: NCT02112032; KEYNOTE-020). Serum samples collected at baseline of treatment-naïve patients were used to analyze systemic formate by mass spectroscopy. Approval to treat patients was obtained from the University of Pittsburgh's Hillman Cancer Center Institutional Review Board (No. PRO14030075).

Healthy human feces samples for human to mouse fecal microbiota transplant (FMT)

Study design, clinical characteristics, and demographic (age, sex, race) characteristics of a cohort of aged healthy adults was recently described. 95 Stool sampling bags (labeled sterile containers with spatula, thermal bag, feces catcher (https://www.fecesvanger.nl/en_GB/), and instructions) were provided to participants and used to collect stool samples The samples were not older than 24 hours and were maintained below 4 °C until delivery. Samples were aliquoted on the same day, flash-frozen in liquid nitrogen, and stored at -80 °C until further analysis. For our analysis, we exclusively used fecal samples at baseline derived from the untreated control arm of the study.

Bioinformatic meta-analysis of melanoma microbiome samples of nine independent cohorts

Whole metagenomic shotgun sequencing data from stool samples of melanoma patients from the studies and cohorts described in Table S7 were downloaded and re-analyzed using the JAMS package (https://www.biorxiv.org/content/10.1101/2023.03.03. 531026v1) version 1.9.8 publicly available at https://github.com/johnmcculloch/JAMS_BW. Study design, baseline clinical and demographic (age, sex, race) characteristics, assessments and definition of endpoints is described in the studies and cohorts described in Table S7.



Animals

C57BL/6J wild type mice were obtained from The Jackson Laboratory. Female mice between 4-10 weeks of age were used for all experiments unless otherwise noted. Nrf2^{-/-} mice (B6.129X1-Nfe2l2^{tm1}Ywk/J, The Jackson Laboratory, 017009), and pmel-1 transgenic mice (B6.Cg-*Thy1*^a/Cy Tg(TcraTcrb)8Rest/J, The Jackson Laboratory, 005023) were obtained from The Jackson Laboratory and bred in-house. Rag2^{-/-} mice were kindly provided by Dr. M. Shlomchik, University of Pittsburgh. OT-1 transgenic mice were kindly provided by Dr. A. Joglekar, University of Pittsburgh. *Ahr*^{fl/fl} *CD8*^{Cre} mice were generated by crossing *Ahr*^{fl} (Ahr^{tm3.1Bra}/J, The Jackson Laboratory, 006203) mice with *CD8α*^{Cre} (C57BL/6-Tg(Cd8a-cre)1ltan/J, The Jackson Laboratory, 008766) mice. *Nrf2*^{fl/fl} *CD8*^{Cre} mice were generated by crossing *Nrf2*^{fl/fl} (C57BL/6-Nfe2l2^{tm1.1Sred}/SbisJ, The Jackson Laboratory, 025433) mice with *CD8α*^{Cre} (C57BL/6-Tg(Cd8a-cre)1ltan/J, The Jackson Laboratory, 008766) mice. For experiments using *Nrf2*^{fl/fl} *CD8*^{Cre} mice, both male and female mice were used in equal ratios and no sex-dependent effects were observed. Mice were housed at the University of Pittsburgh animal facilities under specific pathogen-free (SPF) conditions, where cages were changed on a weekly basis. Ventilated cages, bedding, food and non-acidified water were autoclaved before use, the ambient temperature was maintained at 23 °C, and 5% Clidox-S was used as a disinfectant. Experimental and breeding cages were randomly housed on two different racks in the vivarium, and all cages were kept on automatic 12-hour light/dark cycles. Animal care and experimentation were conducted in accordance with NIH guidelines and approved by the Institutional Animal Care and Use Committee at the University of Pittsburgh.

Gnotobiotic animal husbandry

Food, bedding, and water (non-acidified) were autoclaved before transfer into the sterile isolators. Cages within isolators were changed weekly, and all the cages in the vivarium were kept on 12 hour light/dark cycles. Microbiology testing of fecal (experimental mice) or of cecum samples (sentinel mice; aerobic and anaerobic culture, 16S qPCR) was performed every other week to confirm germ-free (GF) status.

METHOD DETAILS

Exercise and sedentary treatment

Treadmill Exercise Treatment

Mice were exercised on a rodent treadmill (Ugo Basile, 47300/47350) for 5 consecutive days per week for 1 hour per day to stimulate aerobic exercise in all experiments. Running was encouraged with an electric shock of 0.7 mA, 2 Hz dispensed through a metal grate at the rear end of the treadmill belt. All mice received 2-5 days to acclimate to treadmill running, in which they ran on the treadmill at a 5 meter per minute (5 m/min) pace and the electric shock grate was activated so that they could learn how to run successfully. Acclimation sessions lasted 15-45 minutes, with increasing duration of each session every day. Exercise training included a 5-minute 5 m/min warm-up and cool-down at the start and end of each workout, and 50 minutes of exercise at a pace of 8-14 m/min in between (see Figure S1C). Mice which received 20 electric shocks had their electric grate deactivated and were removed from the treadmill for that day, and that day was counted as a "failed session". Mice which failed > 10% of sessions were excluded from the study. Between each exercise session, the treadmill was thoroughly disinfected with 5% Clidox-S.

Treadmill Sedentary Treatment

Sedentary control mice were visually inspected and exposed to circulating vivarium air at the same time exercised mice received exercise treatment. Sedentary mice were placed in a sterile ventilated cardboard bucket directly next to the treadmill, exposing mice to the sounds, smells, and vibrations of the treadmill, similar to the exercised mice. Sedentary treatment occurred at the same frequency and duration as exercise treatment (1 hour/day, 5 consecutive days/week) (see Figures S1A–S1C).

Voluntary Exercise Treatment

Single-housed SPF and GF mice received an electronic running wheel (Lafayette Instrument, ACT-557-WLP) starting two weeks prior to tumor engraftment and continuing throughout the experiment. To ensure accurate measurement of prescribed running activity for each individual, mice were single-housed with free access to a running wheel. The wireless receiver (Lafayette Instrument, ACT-557W-0) was activated using the ClockLab Wireless Collection software program (Lafayette Instrument, AM1-CW01) and programmed to collect data from wheels every 60 seconds. Data describing the number of wheel rotations was used to calculate distance run by each mouse in meters using the formula: $distance run = 2 * \pi * r * x$; where $\pi = 3.14159$; r = radius of the running wheel 0.076325 meters (diameter 6.01 inch = 0.15265 meters / 2) and x = the number of wheel rotations. Mice that ran less than 1000 meters per day on average were excluded from the study. Control mice received a sterile plastic hut and were single-housed to control for the enrichment conditions of the voluntary exercised mice.

Tumor models

Tumor cell models used include: BRAF^{V600E} (YUMM1.7, ATCC, CRL-3362), B16-F10 (ATCC, CRL-6475), B16-OVA (kindly provided by Dr. M Shlomchik, University of Pittsburgh), MC-38 (Kerafast, ENH204-FP) and EL4 (ATCC, TIB-39). Tumor cells were grown *in vitro* under standard conditions (37 °C, stationary, 5% CO₂) in DMEM media (Gibco) supplemented with the following: 10% heat-inactivated FBS, 1x Penicillin-Streptomycin-Glutamine (Gibco), and 1% non-essential amino acids (Sigma-Aldrich) as recommended by manufacturers. *In vitro* cell cultures were kept below 20 passages. Adherent cells were lifted from tissue culture treated dishes using StemProTM AccutaseTM (Gibco) or 0.25% trypsin (Gibco) solution as recommended by manufacturers. Cells were suspended in PBS





(Gibco) and injected subcutaneously (s.c.) into the right hind flank of recipient mice at a concentration of $5 \times 10^5 - 1 \times 10^6$ cells per $100\mu L$ injection unless otherwise indicated. B16-OVA cells (1×10^6 cells per mouse) resuspended in PBS were s.c. injected into the hind flank of C57BL/6J recipient WT mice. Mice then received daily oral gavage (OG) of 200 μ l of 200 mg/kg of formate in PBS or receive a PBS control treatment once their tumors reached $\sim 300 \text{ mm}^3$ in volume until end point analysis (EPA). Tumors were digested and analyzed for CD8-MHC tetramer (K^b)-OVA-specific T cells (see "flow cytometry"). For pulmonary metastases tumor model, mice received 2×10^5 B16-F10 tumor cells by intravenous injection into the tail vein. Tumor measurements were taken using digital calipers and tumor volume was calculated according to the formula *tumor volume* = $\frac{1}{2}$ *length* x *width*, where length represents the largest tumor diameter and width represents the diameter perpendicular to length. For survival experiments, mice were euthanized when calculated tumor volume exceeded 2000 mm³ (BRAF^{V600E} and MC38 tumors) or 3000 mm³ (B16 tumors).

Generation and growth of the *E. coli* Δpfl mutant *Generation*

A mutant lacking the genes encoding the three pyruvate formate lyases (PfIB, PfID, and YbiW) as well as the bifunctional 2-oxobutanoate formate-lyase/pyruvate formate-lyase (TdcE) was created by allelic exchange. The upstream and downstream flanking regions were amplified by PCR using primers listed in Table S6. Gel-purified PCR products were inserted into SphI-digested pGP706⁹⁷ using Gibson assembly (New England Biolabs). The Gibson assembly mixture was introduced into *E. coli* DH5a λpir⁹⁸ using chemical transformation, and positive clones confirmed by Sanger sequencing of the inserts. Plasmids were moved into the conjugation-competent *E. coli* strain S17-1 λpir⁹⁹ by chemical transformation. For mutagenesis, plasmid constructs were sequentially introduced into the *E. coli* strain NRG857c¹⁰⁰ by conjugation. Strains with a single cross-over event were selected on agar plates containing Kanamycin (50 mg/L) and Carbenicillin (100 mg/L), cultured in Luria-Bertani (LB) overnight, and strains with a second cross-over event were selected by sucrose selection (8 g/L nutrient broth base, 5% sucrose, 15 g/L agar). Deletion of the target gene was verified by PCR (see Table S6). This process was repeated to create a NRG857c ΔpfIB ΔpfID ΔybiW ΔtdcE mutant (ΔpfI). NRG857c is naturally resistant to Carbenicillin (100 mg/mI), Chloramphenicol (15 mg/mI) and Tetracycline (20 mg/mI).

Culture Conditions

Both strains, that carry a chloramphenicol resistance gene, were grown from frozen stock in LB broth overnight (37 °C, 200 rpm). The overnight culture was then used to seed new broth cultures at a 1:1000 dilution the following morning. Strains were grown to the desired optical density, then pelleted by centrifugation (10 minutes, 4800 rpm) and resuspended at the desired concentration.

Administration of antibiotics, formate, TBHQ, and bacteria

Mice receiving a daily oral gavage with broad-spectrum antibiotic cocktail received the following compounds at indicated concentrations suspended in 100μ L sterile PBS: metronidazole (2.15 mg/mL) (Sigma-Aldrich, M3761-25G), kanamycin (4 mg/mL) (Gibco, 11815024), colistin (17010 IU/mL) (Sigma-Aldrich, C4461), gentamicin (0.35 mg/mL) (Sigma, G1914-5G), and vancomycin (0.45 mg/mL) (Sigma, V2002-5G). In experiments where mice were maintained on antibiotics-supplemented water bottles, water bottles were refreshed weekly and included the following compounds at indicated concentrations suspended in sterile water: metronidazole (0.043 mg/mL), kanamycin (0.08 mg/mL), colistin (170 IU/mL), gentamicin (0.007 mg/mL), and vancomycin (0.45 mg/mL). Mice receiving oral gavage with formate (200 mg/kg bodyweight (b.w.)) (Fisher Chemical, S648-500) were treated daily beginning once tumors were palpable (\sim 150 mm³) and continuing until end-point analysis (EPA) unless otherwise indicated. Formate oral gavage was suspended in 200 μ L sterile PBS. Mice receiving daily oral gavage with tert-butylhydroquinone (TBHQ) were treated daily with the indicated concentrations resuspended in 200 μ L sterile PBS each day starting when tumors became palpable unless indicated otherwise.

Fecal microbial transplantation (FMT) Preparation

Donor feces were collected from exercised or sedentary mice after 5 weeks of exercise or sedentary treatment and weighed. Similar bacterial load between groups was confirmed by 16S seq. Donor feces were submerged in sterile PBS (0.2 mg feces/mL) for 30 min, then manually homogenized with a sterile serological pipette. The fecal homogenate was centrifuged to pellet large fibers and debris (300 g for 10 minutes). Supernatant was gently removed using a sterile serological pipette and passed through a 0.45 μ m filter into a new conical tube to further eliminate large debris. To heat-kill FMT solutions as done in Figures 2A and 2B, FMT solutions were heated at 90 °C for 2 hours.

Administration

FMT homogenate was created as described above. Mice received 7 consecutive days of oral gavage with a broad-spectrum antibiotic cocktail (see "administration of antibiotics, formate, TBHQ, and bacteria") followed by a 24-hour washout period. Mice then received two FMTs by oral gavage 2 days apart. Each FMT was derived from 40 mg of feces and administered in 200 μ L of PBS. After 48 hours, mice were engrafted with tumor cells as described above.





Fecal microbiota metabolites (MM)

Preparation

FMT solutions prepared as described above were centrifuged to pellet bacteria (4800 rpm, 10 min). Supernatant was gently removed and passed through a 0.22 μm filter.

Administration

Naïve CD8 T cells were stimulated in the presence of a 1% vol/vol solution of the fecal microbiota metabolites derived from either sedentary or exercised FMT or vehicle control for 72 hours (see "in vitro naïve CD8 T cell stimulation").

Cultured fecal microbiota metabolites for in vivo treatment

Preparation

Equal volumes of exercised- or sedentary-FMT suspension, prepared as described above, were aliquoted into four different broth media: Cooked Meat Medium (BD DifcoTM, DF0267-17-9), Reinforced Clostridial Medium (OxoidTM, CM0149B), De Man Rogasa Sharpe (MRS) Medium (OxoidTM, CM0359), and Brain-Heart Infusion Medium (OxoidTM, CM1135B) with a 5% vol/vol defibrinated sheep's blood supplement (HemoStat Laboratories, DSB050). Degassed broth cultures were incubated anaerobically for 48 hours at 37 °C. Cultures were then pelleted by centrifugation (4800 rpm, 10 min) and supernatant was removed and transferred to a new tube. Supernatant was pelleted a second time (4800 rpm, 10 min) to ensure removal of debris. Supernatant was then passed through a 0.22 μM filter and supernatants of exercised-FMT cultures were pooled together to create cultured exercised microbiota metabolites (EX-MM) and supernatants of sedentary-FMT cultures were pooled together to create cultured sedentary microbiota metabolites (SED-MM).

Administration

MM solution was created as described above. Starting one day after TCE, mice received daily oral gavage with 200 μ L of either EX-MM, SED-MM, or broth control. Daily oral gavage continued until EPA.

Bacterial Cell Free Supernatants

1 x 10*8 CFU WT and Δpfl E. coli were inoculated in LB broth and grown for 18 hours (37 °C, 200 rpm). Cultures were pelleted by centrifugation (10 minutes, 4800 rpm) and resulting supernatant was sterile-filtered using a 0.22 μ m filter. Levels of formate were determined by mass spectroscopy (see Figure S5H) and sterile filtered supernatant used in murine *in vitro* naïve CD8 T cell cultures.

CD8/CD4 T cell depletion and anti-PDL1 mAb immunotherapy

For depletion of CD8/CD4 T cells, mice received weekly intraperitoneal injections with 250 μg *InVivoMAb* anti-mouse CD8α (BioXCell, BE0061), *InVivoMAb* anti-mouse CD4 (BioXCell, BE0003-1), or isotype control (BioXCell, BE0090) starting 4 days prior to TCE and continuing weekly until EPA, for a total of 3 treatments.³² For anti-PDL1 immunotherapy treatment,³² mice received intraperitoneal injections on days 6, 8, 10, and 13 post TCE with either 100 μg *InVivoMAb* anti-mouse PDL1 (BioXCell, BE0101) or an equivalent volume of PBS.

Adoptive CD8 T cell transfer experiment

C57BL/6J WT recipient mice received 10⁶ B16-F10 tumor cells subcutaneously (s.c.). Two days later, magnetically purified bulk congenically marked (Thy1.1⁺) CD8 T cells were obtained from spleen and inguinal and axillary lymph nodes of pmel-1 transgenic (tg) mice as previously described.³² 5 x 10⁶ CD8 T cells were then adoptively transferred by intraperitoneal injection into WT recipient mice. 24 hours later, mice began receiving daily oral gavage with formate (200 mg/kg b.w.) or vehicle (PBS) which continued until EPA. Congenically marked Thy1.1 pmel-1 tg CD8 T cells were analyzed by flow cytometry at EPA.

In vivo AhR and Nrf2 inhibitor treatment

BRAF V600E tumor-bearing mice underwent interventional exercise or sedentary treatment alongside treatment with vehicle (corn oil), AhR inhibitor (CH223191; 300 μ g/mouse), or Nrf2 inhibitor (ML385; 100 μ g/mouse) via intraperitoneal injection (volume: 200 μ L). Treatment was performed five consecutive days/week until EPA.

Tissue harvest and cell purification

Tumors, tumor-draining lymph nodes (tdLNs), and spleens were harvested using autoclaved dissection tools under sterile conditions and tumor weight was recorded. Spleens and tdLNs were mashed and underwent erythrocyte lysis using the Mouse Erythrocyte Lysing Kit (R&D Systems, WL2000). Remaining splenocytes and tdLN cells were used for flow cytometry analysis. Tumor-intrinsic lymphocytes were isolated by collagenase type 4 digest (Worthington, LS004189), followed by purification of mononuclear cells using a 40% Percoll centrifugation (Cytiva, 17089101), an erythrocyte lysis using the previously mentioned kit, and enrichment of CD45⁺ cells as follows: cells were incubated on ice with rat serum and Fc block (BD Biosciences, 553142) for 5 min, then incubated on ice with biotinylated anti-CD45 antibody (Biolegend, 103104) for another 15 min. Cells were washed and incubated with streptavidin beads (BD Biosciences, 557812) for 30 min, followed by a 5 min incubation in an EasySep magnet (STEMCELL, 18000). Cells poured out of the magnet were discarded, and cells remaining were used for flow cytometric analysis.





Flow cytometry

Single cell suspensions were prepared as described above and stimulated in RPMI containing PMA (0.1 µg/mL), ionomycin (1 µg/mL), Golgi Stop (GS) (1.95 μM), and Golgi Plug (GP) (1 μg/mL). After 3 hours of stimulation, cells were washed and resuspended in FACS buffer (PBS, 2% FBS) for immunostaining and subsequent FACS analysis. Cell suspensions were incubated with Fc Block (BD Biosciences, 553142), followed with an optional tetramer stain (SIINFEKL-APC MHC I Tetramer, provided by NIH Tetramer Core Facility) for 30 min at room temperature. Then, cells received a surface marker antibody (Ab) stain for 20 min at 4 °C. Surface Abs were used as follows: anti-CD45 (BV480, BD Biosciences, 566095; BUV395, BD Biosciences, 564279; APC-Cy7, BD Biosciences, 557659), anti-TCRβ (Alexa Fluor 700, BD Biosciences, 560705), anti-TCRγδ (FITC, BioLegend, 107504), anti-CD4 (BUV395, BD Biosciences, 563790; BV650, BD Biosciences, 563232), anti-CD8α (BV570, BioLegend, 100740; BUV737, BioLegend, 612759), anti-CD279 (PD-1) (BV786, BD Biosciences, 744548), anti-CD90.1 (Thy-1.1) (eFluor 450, BD Biosciences, 741213), anti-CD90.2 (Thy-1.2) (BUV563, Invitrogen, 48-0900-82), anti-I-A/I-E (MHC II) (BUV496, BD Biosciences, 750281; FITC, Thermo Fisher Scientific, 11-5321-82), anti-CD11c (FITC, BioLegend, 117306; BV421, BD Biosciences, 565452), anti-CD11b (APC-eFluor 780, eBioscience, 47-0112-80; BUV805, BD Biosciences, 741934), anti-F4/80 (PE-Cyanine5, eBioscience, 15-4801-80), anti-Gr1 (PerCP-Cy5.5, BD Biosciences, 552093), anti-NK1.1 (BV421, BD Biosciences, 568224), anti-CD44 (PECy5, BD Pharmingen, 553135), anti-CD62L (Percp-Cy5.5, MFR, BD Pharmingen, 560513), and anti-IFNyR1 (PE, ThermoFisher, 12-1191-82). For dead cell exclusion, cells were stained with Zombie NIR Fixable Viability Kit (BioLegend, 423105) for 10 min at 4 °C and washed in FACS buffer. For intracellular cytokine and transcription factor staining, surface Ab-stained cells were first fixed and permeabilized using the FoxP3 Transcription Factor Staining Buffer kit (eBioscience, 00-5523-00) following manufacturer's instructions. Cells were further stained with Abs against intracellular proteins for 30 min at 4 °C. Intracelluar Abs were used as follows: anti-IFNγ (BV605, BioLegend, 505839; PE-Cy7, Fisher Tonbo Biosciences, 50-105-4909), anti-FoxP3 (FITC, eBioscience, 11-5773-82; efluor 450, Thermo Fisher Scientific, 50-163-74), anti-Granzyme B (PE, eBioscience, 12-8898-80), anti-Ki67 (PE-eFluor 610, eBioscience, 61-5698-82), anti-TNFα (APC, BioLegend, 506308), anti-Tbet (BV421, BioLegend, 644832), and anti-Eomesodermin (EOMES) (Alexa Fluor 488, Invitrogen, 53-4875-82). Samples were gated on FSC-A/SSC-A to exclude debris and gated to exclude dead cells. Samples were collected using a Cytek Aurora flow cytometer and analyzed with FlowJo 10 Software (Tree Star). Flow cytometry of tumor draining lymph node and tumor of sedentary and exercised mice displayed in Figures S2A-S2H was performed at day 13 post TCE (pTCE).

T Cell Gating Strategies: Lymphocytes (FSC-H vs SSC-H), Single Cells (FSC-H vs FSC-A), Live CD45+ cells (Zombie NIR- and CD45+), T cells (TCR β + or TCR $\gamma\delta$ +); CD8 T cells (CD8 α +, CD4- gated on TCR β + cells); CD4 T cells (CD8 α -, CD4+ gated on TCR β + cells); TNF α -producing CD8 T cells (TNF α + gated on CD8 T cells); TNF α -producing CD4 T cells (TNF α + gated on CD4 T cells); Proliferating CD8 T cells (Ki67+ gated on CD8 T cells); Proliferating CD4 T cells (Ki67+ gated on CD4 T cells); Cytokine-producing proliferating CD8 T cells (IFNγ+, GzmB+, or TNF α + gated on Proliferating CD8 T cells); Cytokine-producing proliferating CD4 T cells (IFN γ +, GzmB+, or TNF α + gated on Proliferating CD4 T cells); Activated CD8 T cells (PD-1+ gated on CD8 T cells); Activated CD4 T cells (PD-1+ gated on CD4 T cells); Cytokine-producing activated CD8 T cells (IFNγ+, GzmB+, or TNFα+ gated on Activated CD8 T cells); Cytokine-producing proliferating CD4 T cells (IFNγ+, GzmB+, or TNFα+ gated on Activated CD4 T cells); EOMES+ CD8 T cells (EOMES+ gated on CD8 T cells); Tbet+ CD8 T cells (Tbet+ gated on CD8 T cells); Th1 cells (IFNγ+ gated on CD4 T cells); Tc1 cells (IFNγ+ gated on CD8 T cells); GzmB-producing Th1 cells (GzmB+ gated on Th1 cells); GzmB-producing Tc1 cells (GzmB+ gated on Tc1 cells); IFNy GzmB double-producing CD8 T cells (IFNy+ GzmB+ gated on CD8 T cells); IFNy GzmB double-producing CD4 T cells (IFNy+ GzmB+ gated on CD4 T cells); OVA-antigen specific CD8 T cells (SIINFEKL+ gated on CD8 T cells); OVA-antigen specific Tc1 cells (IFNγ+ gated on OVA-antigen specific CD8 T cells); TNF α -producing OVA-antigen specific CD8 T cells (TNF α + gated on OVA-antigen specific CD8 T cells) Treg cells (Foxp3+ gated on CD4 T cells); γδ T cells (TCRγδ +, TCRβ- gated on Live CD45+ cells); Effector Tc1 cells (CD44+CD62- gated on CD8T cells), IRF8+ CD8T cells (IRF8+ gated on CD8T cells), pSTAT1+ CD8T cell (pSTAT+ gated on CD8T cells) and pCreb+ CD8T cells (pCreb+ gated on CD8T cells). Gating Strategies for Figures S2G and S2H: Lymphocytes (FSC-H vs SSC-H), Single Cells (FSC-H vs FSC-A), Live CD45+ cells (Zombie NIR- and CD45+); DCs (MHC-II+, CD11c+ gated on Live CD45+ cells); Macrophages (CD11b+, F4-80+ gated on Live CD45+ cells); MDSCs (CD11b+, Gr-1+ gated on Live CD45+ cells); NK cells (NK1.1+, CD11b- gated on Live CD45+, CD8aand CD4- cells); NK T cells (NK1.1+, CD11b- gated on CD8a+ T cells and CD4+ T cells).

In vitro naïve CD8 T cell stimulation

Naïve CD8 T cells derived from spleen, axial and inguinal lymph nodes of WT mice were purified with EasySepTM Mouse Naïve CD8 T Cell Isolation Kit (Stem cell Technologies, 19858). Purity test by flow cytometry revealed 95%–98% enriched TCRb+ NK1.1- TCRgd-MHCII- CD44- CD25- CD62L+ cells (data not shown). 2-5 x 10⁵ naïve CD8 T cells were stimulated in complete RPMI-1640 culture medium in a plate precoated with αCD3 (BD Biosciences, 553057) and soluble αCD28 (BD Biosciences, 553294) (both 1 μg/mL) in the presence of experimental stimulants as follows: Microbial metabolites (MM): 1% (vol./vol.) EX-MM, SED-MM, or vehicle control (PBS) for 72 hours followed by re-stimulation with PMA/ionomycin in presence of GS and GP for 3h and flow cytometry (see "flow cytometry"). Formate: 2mM formate or vehicle control (PBS) for 24 or 72 hours followed by re-stimulation with PMA/ionomycin in presence of GS and GP for 3 hours and flow cytometry (see "flow cytometry"). WT or Δ*pfl E. coli* cell free supernatant: 0.1% (vol./vol.) of bacterial cell-free culture supernatant or equivalent volume sterile PBS was added to naïve CD8 T cell cultures for 72 hours, followed by re-stimulation with PMA/ionomycin in presence of GS and GP for 3 hours and flow cytometry (see "flow cytometry"). TBHQ: 1 nM TBHQ or vehicle control (PBS) was added to naïve CD8 T cell cultures for 72 hours, followed by re-stimulation with PMA/ionomycin in presence of GS and GP for 3 hours and flow cytometry"). Nrf2 Inhibitor ML385:





 $10 \mu M$ Inhibitor or equivalent volume vehicle (DMSO) control. Cells were analyzed for cytokine production by flow cytometry or lysed for analysis of gene expression by qPCR using the RNA processing method as described in "RNA processing and RT-PCR of CD8 T cells".

Phospho-CREB analysis

Naïve CD8 T cells were purified from splenocytes and lymph nodes of WT mice using a naive CD8 T cell purification Kit (Stem cell Technologies). Phospho-CREB analysis in murine naïve CD8 T cells followed our previously published protocol. Briefly, cells were treated with vehicle (PBS) or 2.5 μM Sodium Formate (Fisher) for 72 hours and followed by additional stimulation with PMA (0.1 μg/mL) and ionomycin (1 μg/mL) for 30 min. Cells were then fixed with BD Phosflow Lyse/Fix Buffer (BD Biosciences, 558049) for 15 min at 37 °C. Fixable live/dead viability stain (Zombie NIR, BioLegend, 423105) was added 15 min prior to fixation. Samples were then permeabilized with ice-cold pre-chilled True-Phos Perm Buffer (BioLegend, 425401) and incubated at -20 °C for 2 hours. After wash, cells were incubated with Abs against CD45 (BV480), CD4 (BV605), CD8 (BV570), CD44 (PECy5), CD62L (Percp5.5), TCRβ (Alexa Fluor® 700), and phospho-CREB (PE, Cell Signaling Technology, 14228S) in FACS buffer for 30 min at RT. Samples were acquired on an Aurora (Cytek) flow cytometer and analyzed with FlowJo 10.

Phospho-STAT1 analysis

Naïve CD8 T cells were purified from splenocytes and lymph nodes of Nrf2 $^{+/+}$ and Nrf2 $^{-/-}$ mice using a naïve CD8 T cell purification Kit (Stem cell Technologies). Phospho-STAT1 analysis in murine naïve CD8 T cells (density: $5x10^5$ cells in 96 well plate) followed the previously published protocol. He Briefly, CD8 T cells were activated with α CD3 and soluble α CD28 (each 1 μ g/mL) in presence of vehicle (PBS) or 2.5 μ M Sodium Formate (Fisher) for 12 hours before fixed with Lyse/Fix Buffer (BD Biosciences, 558049) for 15 min at 37 °C. Fixable live/dead viability stain (Zombie NIR, BioLegend, 423105) was added 15 min prior to fixation. Samples were then permeabilized with ice-cold pre-chilled True-Phos Perm Buffer (BioLegend, 425401) and incubated at -20 °C for 2 hours. After wash, cells were incubated with Abs against CD45 (BV480), CD4 (BV605), CD8 (BV570), CD44 (PECy5), CD62L (Percp5.5), TCR β (Alexa Fluor® 700), and phospho-STAT1 (PE, Biolegend, 686404) in FACS buffer for 30 min at RT. Samples were acquired on an Aurora (Cytek) flow cytometer and analyzed with FlowJo 10.

RNA processing and RT-PCR of CD8 T cells

Lymphocytes were isolated from the spleen and peripheral lymph nodes of naïve mice. Naïve CD8 ⁺ T cells were purified by naïve CD8 T cell purification Kit (Stem cell Technologies) and purity test was performed (data not shown, purity >98%). Naïve CD8 ⁺ T cells were then cultured in complete RPMI-1640 culture medium with 10 ng/ml recombinant mouse IL-12 (BioLegend) in a plate pre-coated with α CD3 (1 μ g/mL) and α CD28 (1 μ g/mL) for 18 hours. Activated CD8 T cells were subsequently treated with vehicle control (PBS) or 2 mM Formate (Fisher Scientific) for additional 24 hours. Following *in vitro* stimulation, CD8 T cells were collected and stored in RLT buffer (Qiagen) supplemented with 1% vol/vol β -mercaptoethanol. RNA was extracted using the RNeasy Mini Kit (Qiagen). cDNA synthesis was performed using iScript cDNA Synthesis Kit (Bio-Rad) according to manufacturer's instructions. Expression analysis was performed in duplicate via real-time PCR on a BioRad CFX384 Touch Real-Time PCR Detection System using iTaq Universal SYBR (Bio-Rad). Expression levels were quantified and normalized to *Gapdh* expression. Primer sequences see Table S6. These cells were used for RNAseq analysis displayed in Figures 5L and 5M.

RNAseq of CD8 T cells

After initial QC and adapter trimming, the sequenced data was quantified using Kallisto¹⁰¹ to obtain transcript level abundances using *mm10* (UCSC) as reference. Post quantification differentially expressed genes (DEGs) and transcripts between the PBS and 2mM formate treated CD8 T cells were identified using Sleuth.¹⁰² Significant differentially expressed transcripts were defined using a q-value (Benjamini-Hochberg adjusted p-value) threshold of <0.2.

Transcription Factor Enrichment Analysis (TFEA)

We used the web-based ChEA3 TFEA tool (ENCODE-CHIP-SEQ)⁷³ to identify the transcription factors responsible for observed changes in gene expression when comparing PBS and formate treated CD8 T cells (Using all DEGs padj < 0.2; Table S3).

Collection and processing of intestinal contents and serum for Nrf2 reporter cell assays

Luminal intestinal contents (small intestine, cecum, and colon) were weighed and homogenized in sterile PBS. Luminal intestinal content homogenate was centrifuged (5000 rpm, 10 min) and pelleted debris and bacteria were discarded, supernatant was transferred to a new tube and saved. Serum was diluted 1:1 with sterile PBS. Colon, cecum, and small intestinal content supernatant was added to reporter cells at a 1:4 dilution (vol/vol). Serum was added to reporter cells at a 1:10 dilution (vol/vol).

Nrf2 reporter cell assay

Luciferase-expressing HEK 293 Δ NRF2/ARE cells (referred to as "Nrf2 reporter cells") were purchased from Signosis (SL-0042). Cells were cultured in DMEM media supplemented with 10% Δ FBS, penicillin/streptomycin, and hygromycin B (50 μ g/mL) (InvivoGen, anthg-1). 96-well tissue culture plates pre-treated with gelatin were seeded with 3 x 10⁴ Nrf2 reporter cells and incubated overnight





(37 °C). Cells were then exposed to experimental treatments and controls at the indicated concentration. Tert-butylhydroguinone (TBHQ) was used as a positive control to induce Nrf2 signaling. Reporter cells were incubated with experimental treatments for 24 hours and then plates were washed with PBS. Cells were lysed and then lysate was transferred to a 96-Well Clear Bottom Black Microplate (Corning) and combined with luciferase substrate. Luminosity was immediately recorded using a Spectral Max i3x 96-well plate reader with SoftMax Pro 3.0.7 Software under the following settings: read type endpoint at all wavelengths, integration time 10 s, read height 2 mm. Nrf2 activity in intestinal contents and serum of sedentary and exercised mice was performed at day 13 pTCE (Figures 6B and 6C).

AhR reporter cell assay

Luciferase-expressing HT29-LuciaTM AhR reporter cells under the control of Cyp1a1 gene promoter (referred to as "AhR reporter cells") were purchased from InvivoGen (ht2l-ahr). Cells were cultured in DMEM (Gibco) supplemented with 10% FBS, 1x Penicillin-Streptomycin-Glutamine (Gibco), 100 μg/mL Normocin (InvivoGen), and 100 μg/mL selective antibiotic Zeocin (InvivoGen). Briefly, 20 µL of sample was incubated with approximately 50,000 AhR reporter cells for 24 h. Following incubation, 20 µL of supernatant was transferred into a 96-Well Clear Bottom Black Microplate (Corning) and 50 µL QUANTI-Luc™ (InvivoGen) was added. Samples were immediately assessed for luminescence using a SpectraMax® i3x plate reader with SoftMax Pro 3.0.7 Software under the following settings: read type endpoint at all wavelengths, integration time 100 ms, read height 2 mm.

DNA for 16S quantification in feces

The Fast DNA Stool Mini Kit (Qiagen, 51604) was used to extract DNA from feces for fecal 16S quantification in Figure S3G. Quantitative PCR (qPCR) was performed as recently described. 31,32,46 Briefly, qPCR was performed on a Bio-Rad CFX384 TouchTM Real-Time PCR Detection System using iTaq™ Universal SYBR (Bio-Rad, 1725125) and the following universal 16S rRNA-encoding gene primers: (340For, 5'-ACTCCTACGGGAGGCAGCAGT-3' and 514Rev, 5'-ATTACCGCGGCTGCTGGC-3'). Reactions were run at 95 °C for 3 min, followed by 40 cycles of 95 °C for 15 min and 63 °C for 60 seconds. Purified genomic DNA from Blautia producta (Prevot) (ATCC, 27340D-5) was used as a standard. Standards ranging in concentration from 10⁰ – 10⁸ plasmid copies per μL were run in parallel with our fecal samples during each qPCR run. Using those results, a standard curve was generated to quantify the copy numbers within the samples. To determine the bacterial load in the feces samples, the results were normalized to fecal weight.

Tumor cell killing assay

Spleens were harvested from OT-1 transgenic C57BL/6J mice and bulk CD8 T cells were isolated using magnetic purification. CD8 T cells were stimulated and incubated at 37 °C and 5% CO₂ for 72 hours in an αCD3 (Fisher Scientific) coated 96-well flat-bottomed plate containing DMEM with 2 μg/mL αCD28 (Fisher Scientific), 100 units/mL IL-2 (Peprotech), and 10 ng/mL IL-12 (BioLegend). Additionally, samples were stimulated with either formate (2 mM), formate and Nrf2 inhibitor (ML385) (10 μM), or an equal volume of vehicle control media. After 72 hours, CD8 T cells were isolated and 3,000 live stimulated OT-1 CD8 T cells were then cocultured with 15,000 B16-OVA-GFP tumor cells per well in a 96 well flat-bottomed plate for 24 hours. After 24 hours, cocultures were transferred to a 96 well v-bottom plate for viability analysis by flow cytometry, with GFP as a B16-OVA marker and Zombie NIR (BioLegend) as a viability marker. Samples from each spleen were run in duplicate and final absolute numbers were averaged together for sample readout.

Growth curve of BRAFV600E with CCK-8 Assay

Cell viability was assessed using the Cell Counting Kit-8 (CCK-8, APExBIO, Catalog No. K1018). BRAFV600E cells were seeded in 96-well plates at a density of 2,000 cells per well in 100 µL of complete medium supplemented with 2 mM Formate or PBS. Cell viability was measured at four different time points: day 1, day 3, day 5, and day 7. At each time point, 5 μL of CCK-8 solution was added to each well, and the plates were incubated for 2 hours at 37 °C. After incubation, the absorbance was measured at 450 nm using a microplate reader (Tecan, SPARK). The absorbance values were directly proportional to the number of viable cells.

16S Analysis and sample processing

Samples were homogenized in 1 mL of extraction buffer [50 mM Tris (pH 7.4), 100 mM EDTA (pH 8.0), 400 mM NaCl, 0.5% SDS] with 20 μL of proteinase K (20 mg/mL) in a 1.5 mL microcentrifuge tube. Silica beads (0.1 mm diameter) were added to the homogenate and tubes were loaded onto a Mini-Beadbeater-8 cell disrupter (BioSpec Products, Bartlesville, OK) for 2 x 1-min cycles to lyse cells. Tubes were incubated at 55 °C overnight on a shaker before genomic DNA was extracted via phenol:choloroform:isoamyl alcohol and precipitated with ethanol. The isolated DNA was dissolved in nuclease-free water and analyzed for concentration (Nanodrop, ThermoFisher) prior to sequencing. Library preparation and bioinformatics: Extracted DNA samples were submitted to the University of Wisconsin Biotechnology Center for amplification and sequencing of the V3-V4 region of the 16S rRNA gene (forward: 341 Fwd: 5'-CCTACG-GGNGGCWGCAG-3' and reverse: 805 Rev: 5'-GACTACHVGG-GTATCTAATCC-3') on an Illumina MiSeq platform (Illumina Inc., San Diego, CA, USA). The resulting sequences were demultiplexed and forward and reverse reads were paired in QIIME2 (version 2023.7). 103 Paired-end reads were passed to DADA2 for trimming, dereplication, denoising, and filtering. 104 Quality threshold was set at 30 and chimeric sequences were removed. A total of 1,511 sequences were detected and average sequence





length was 419 bp. A total of 4,542,990 reads were generated with a median of 148,438 reads per sample. Taxonomy was assigned with a naïve-Bayes classifier, trained with the 341F/805R amplicons against the Silva 138.1 nr99 SSU database. 105 Phylogenetic tree was generated with the fasttree QIIME2 plugin. 106 Predicted metagenomic function was assessed with PICRUSt2, 45 using EPA-NG for phylogenetic read placement, ¹⁰⁷ and castor for hidden state predictions. ⁷⁷ Predicted pathways were annotated with the MetaCyc pathway database, ¹⁰⁸ and specific Enzyme Commission (EC) numbers were further compared between groups. The relative contribution to predicted pfl (EC: 2.3.1.54 - pyruvate formate lyase) expression (referred to as "predicted pfl abundance") was calculated by dividing the predicted counts attributed to each taxa within each group to that group's total predicted pfl count. Statistics & Analyses: The phylogenetic tree, taxonomy, and feature table were uploaded to the MicrobiomeAnalyst portal maintained by the Xia laboratory at McGill University for analyses. 109 Low-count filter was set at counts = 4 with prevalence of 20% while low-variance filter was set at 10% interquartile range. No rarefaction was used for these analyses as all samples had sufficient read depth. Beta diversity was quantified with weighted and unweighted UniFrac¹¹⁰ and groups were compared with PERMANOVA, while alpha diversity was quantified by CHAO1 counts and Shannon Diversity index and statistical differences were assessed with Student's T-test or one-way ANOVA. Untargeted differential abundance analyses were conducted with DESeq2111 R package to quantify relative differences in abundance between groups. PICRUSt2 data were analyzed and plotted with the ggpicrust2 R package. 112

Untargeted high-resolution LC-HRMS

Metabolic quenching and polar metabolite pool extraction was performed on stool samples by adding ice cold 80% aqueous methanol containing deuterated D₃-creatinine and D₃-alanine, D₄-taurine and D₃-lactate (Sigma-Aldrich) at a final concentration of 10μM. After 3 minutes of vortexing, samples were homogenized using a FastPrep-24 system (MP-Bio), with Matrix D at 60 Hz for 30 s, before being cleared of protein by centrifugation at 16,000xq. Cleared supernatant (2 µL) was subjected to online LC-MS analysis. LC-HRMS Method Analyses were performed by untargeted LC-HRMS. Briefly, Samples were injected via a Thermo Vanquish UHPLC and separated over a reversed phase Thermo HyperCarb porous graphite column (2.1×100 mm, 3 μm particle size) maintained at 55 °C. For the 20-minute LC gradient, the mobile phase consisted of the following: solvent A (water / 0.1% formic acid) and solvent B (acetonitrile / 0.1% formic acid). The gradient was the following: 0-1 min 1% B, increase to 15 %B over 5 minutes, continue increasing to 98% B over 5 minutes, hold at 98% B for five minutes, reequillibrate at 1% B for five minutes. The Thermo IDX tribrid mass spectrometer was operated in both positive and negative ion mode, scanning in Data Dependent MS2 (ddMS2) mode (2 µscans) from m/z 70 to 800 at 120,000 resolution with an AGC target of 2 x 10⁵ for full scan, 2 x 10⁴ for MS2 scans using higher energy collisional dissociation (HCD) fragmentation at stepped 15, 35, and 50 eV collision energies. Source ionization setting was 3.0 and 2.4 kV spray voltage respectively for positive and negative mode. Source gas parameters were 35 sheath gas, 12 auxiliary gas at 320 °C, and 8 sweep gas. Calibration was performed prior to analysis using the PierceTM FlexMix Ion Calibration Solutions (Thermo Fisher Scientific). Integrated peak areas were then extracted manually using Quan Browser (Thermo Fisher Xcalibur ver. 2.7). Untargeted differential comparisons were performed using Compound Discoverer 3.3 (Thermo Fisher) to generate a ranked list of significant compounds with tentative identifications from BioCyc, KEGG, and internal compound databases. Purified standards were then purchased and compared in retention time, m/z, along with MS2 fragmentation patterns to validate the identity of significant hits.

Significant Latent Factor Interaction Discovery and Exploration (SLIDE) Analysis

Of the 6000 spectral features measured in total (see untargeted high-resolution LC-HRMS), 3200 of which have putative compound identifications obtained by searching six compound databases (Predicted Compositions, mzCloud, mzVault, Metabolika, ChemSpider, MassList). Unannotated measurements represent spectral features for which no chemical structure can be uniquely assigned. These 3200 annotated spectral features corresponded to a total of 1700 unique compounds. For compounds with measurements from multiple annotated spectral features, we used the average. For downstream analyses, we then focused on the top 75% of compounds in terms of variance. Variance in an unsupervised fashion to avoid signal leakage. This pre-filtering unsupervised step removes compounds that do not vary meaningfully across the samples. We then applied Significant Latent Factor Interaction Discovery and Exploration (SLIDE) on these compounds and built a multivariate machine learning model to determine context-specific metabolites which can differentiate between exercise or sedentary metabolomes.³⁴ Model performance was evaluated using true class labels (SLIDE) and against shuffled labels (Permuted SLIDE). SLIDE identified 4 significant latent factors (context-specific co-abundant metabolite modules) (Z3 (effect size 0.46) displayed in Figure 3C and Table S1; Z9 (effect size 0.36); Z5 effect size 0.35); Z7 (effect size 0.19)) from 9 latent factors total using the following parameters for 1000 iterations: delta = 0.275, lambda = 0.5, spec = 0.1. Classification performance for significant latent factors was then evaluated using k-fold cross validation with permutation testing for 25 replicates and k = 5. Functional analysis was performed using Metaboanalyst and Mummichog³⁵ using the top 20 univariate predictive and top 20 by latent factor loading metabolites from each significant latent factor. We visualize correlations between compounds associated with relevant pathways using a network diagram, where for node colors we use orange to indicate compounds that are predictors for exercise and light blue for predictors for sedentary metabolomes; edge colors we use purple for positive correlations and green for negative correlations, and edge thickness is proportional to correlation strength. Metabolites with highest univariate AUC or latent factor loading are visualized. Pathway associations for each metabolite are indicated. Putative metabolites of each latent factor were linked to metabolic pathways by searching KEGG for associated pathway modules (see Table S1).





Bile acids detection in fecal samples

Bile acids were quantified by a previously published stable-isotope-dilution liquid chromatography mass spectrometry (LC-MS/MS) method¹¹³ with some modifications. Briefly, ultrapure ice-cold water was added to weighted colon contents (150 µL) and vortexed followed by the addition of ice-cold methanol (500 μL) with additional vortexing. Colonic extracts were centrifuged (14,000xg, 20 min, 4 °C) and ice-cold methanolic internal standard solution containing D₄-chenodeoxycholic acid (D₄-CDCA), D₄-cholic acid (D₄-CA), D₄-deoxycholic acid (D₄-DCA), D₄-lithocholic acid (D₄-LCA), D₄-glycochenodeoxycholic acid (D₄-GCDCA), D₄-glycocholic acid (D₄-GCA), D₄-glycodeoxycholic acid (D₄-GDCA), D₄-glycolithocholic acid (D₄-GLCA), D₄-glycoursodeoxycholic acid (D₄-GUDCA), D₄-taurocholic acid (D₄-TCA), D₄-taurodeoxycholic acid (D₄-TDCA) and D₄-taurochenodeoxycholic acid (D4-TCDCA) (20 μL) was mixed with the supernatant (80 μL) and transferred to glass HPLC vials with micro-inserts and subjected to LC-MS/MS analysis. Calibration standards were prepared in methanol and quality control samples were prepared from pulled mouse colon content samples and processed identically as samples.

LC-MS/MS analysis was performed on a chromatographic system consisting of two Shimadzu LC-30 AD pumps (Nexera X2), a CTO 20AC oven operating at 40 °C, and a SIL-30 AC-MP autosampler in tandem with 8050 triple quadruple mass spectrometer (Shimadzu Scientific Instruments, Inc). An ACE Excel C18-Amide column (75 mm × 2.1 mm; 1.7 μm) (Cat# EXL-1712-7502U, Avantor) was used for chromatographic separation. A gradient of solvent A (0.1% acetic acid in water) and B (0.1% acetic acid in acetonitrile: methanol 50:50; v/v) was used for chromatographic separation with a flow rate of 0.4 mL/min and a 1 µL injection volume. Electrospray ionization in negative ion mode was used with the following multiple reaction monitoring (MRM) conditions: m/z 373.3⇒373.3 for cholenic acid and 3-keto-cholanic acid; m/z 375.3 ⇒ 375.0 for iso-LCA, LCA, allo-iso-LCA, and allo-LCA; m/z 377.3 ⇒ 377.3 nor-DCA; m/z 387.3⇒387.3 for 3,7-diketocholanic acid, 3,6-diketocholanic acid and 12-keto-9,5-cholenic acid; m/z 389.3⇒389.3 for 3-keto-DCA, 6-keto-LCA, 7-keto-LCA, 12-keto-LCA, apo-CA, 3-keto-CDCA; m/z 391.3⇒391.3 for DCA, hyodeoxycholic acid (HDCA), CDCA, UDCA, iso-UDCA, 7-iso-DCA, iso-DCA and muro-DCA; m/z 401.2⇒331.1 for triketocholanic acid; m/z $403.3 \Rightarrow 403.3$ for 7,12-diketo-LCA, 7-keto-DCA and takeda ketol; m/z 407.2 \Rightarrow 407.2 for CA, α-muricholic acid (α-MCA), β-MCA, ω-MCA, hyocholic acid (HCA), ursocholic acid (UCA) and allo-CA; m/z 432.3⇒73.9 for GLCA; m/z 448.3⇒73.9 for GCDCA, GHDCA, GUDCA and GDCA; *m/z* 455.2⇒96.9 for LCA-SO₄; *m/z* 458.2⇒73.9 for G-dehydroCA; *m/z* 464.3⇒73.9 for GCA, GHCA; m/z 482.2⇒123.9 for TLCA; m/z 487.2⇒96.9 for CA-7-SO₄; m/z 498.2⇒123.9 for THDCA, TCDCA, TDCA and TUDCA; m/z 514.2⇒123.9 for TCA, THCA, T-α-MCA, T-β-MCA and T-ω-MCA; m/z 379.3⇒379.3 for D₄-LCA; m/z 395.3⇒395.3 for D₄-CDCA and D₄-DCA; m/z 411.2 \Rightarrow 411.2 for D₄-CA; m/z 436.2 \Rightarrow 73.9 for D₄-GLCA; m/z 452.3 \Rightarrow 73.9 for D₄-GCDCA, D₄-GDCA and D₄-GCDCA GUDCA; m/z 468.2 \Rightarrow 73.9 for D₄-GCA; m/z 502.2 \Rightarrow 127.9 for D₄-TDCA and D₄-TCDCA; m/z 518.2 \Rightarrow 127.9 for D₄-TCA. The following ion source parameters were applied: nebulizing gas flow, 3 L/min; heating gas flow, 10 L/min; interface temperature, 300 °C; desolvation line temperature, 250 °C; heat block temperature, 400 °C; and drying gas flow, 10 L/min. For data analysis software Lab Solution Version 5.89 (Shimadzu) was used. All 51 bile acids were measured, and the ones detected in colon contents are displayed in Figures S4A and S4B (see Table S1). Bile acid analysis in colon contents of sedentary and exercised mice was performed at day 13 pTCE (Figures S4A and S4B).

3NP-Short chain fatty acid (SCFA) detection

Sample Preparation: Cecum and tumor samples were homogenized with 50% aqueous acetonitrile at a ratio of 1:15 vol:wt. Serum metabolites were extracted with 4 volumes of 1:1 methanol: ethanol, both extraction types were spiked with 5 μg/mL deuterated internal standards: D₂-formate, D₄-acetate, D₅-butyrate, D₆-propionate, D₂-valerate and D₄-hexanoate (CDN Isotopes, Quebec, Canada). Samples were homogenized using a FastPrep-24 system (MP-Bio), with Matrix D at 60 Hz for 30 s, before being cleared of protein by centrifugation at 16,000xg. Cleared supernatants (60 µL) were collected and derivatized using 3-nitrophenylhydrazine. Each sample was mixed with 20 µL of 200 mM 3-nitrophenylhydrazine in 50% aqueous acetonitrile and 20 µL of 120 mM N-(3-dimethylaminopropyl)-N'-ethylcarbodiimide -6% pyridine solution in 50% aqueous acetonitrile. The mixture was reacted at 50 °C or 40 min and the reaction was stopped with 0.45 mL of 50% acetonitrile. LC-MS Analysis: Derivatized samples were injected (50 µL) via a Thermo Vanquish UHPLC and separated over a reversed phase Phenomenex Kinetex 150 mm x 2.1mm 1.7 μM particle C₁₈ maintained at 55 °C. For the 20 min LC gradient, the mobile phase consisted of the following: solvent A (water / 0.1% formic acid) and solvent B (acetonitrile / 0.1% formic acid). The gradient was the following: 0-2min 15% B, increase to 60%B over 10 min, continue increasing to 100% B over 1 min, hold at 100% B for 3 min, reequillibrate at 15% B for 4 min. The Thermo IDX tribrid mass spectrometer was operated in positive ion mode, scanning in ddMS2 mode (2 μscans) from m/z 75 to 1000 at 120,000 resolution with an AGC target of 2x10⁵ for full scan, 2x10⁴ for MS2 scans using HCD at stepped 15, 35, and 50 eV collision energies. Source ionization setting was 3.0 kV spray voltage respectively for positive mode. Source gas parameters were 45 sheath gas, 12 auxiliary gas at 320 °C, and 3 sweep gas. Calibration was performed prior to analysis using the PierceTM FlexMix Ion Calibration Solutions (Thermo Fisher Scientific). Integrated peak areas were then extracted manually using Quan Browser (Thermo Fisher Xcalibur ver. 2.7). SCFA are reported as area ratio of SCFA to the internal standard. SCFA analysis in cecum, serum and tumor of sedentary and exercised mice was performed at day 13 pTCE (Figures 3I, 3J, and S4C-S4F). The perturbations (exercise, exercise-FMT, formate oral gavage) used in our study to increase systemic formate levels by formate oral gavage, exercise and exercise-FMT induce comparable levels of formate in serum: In mammalian organisms, circulating (blood serum) formate levels are found in the range between 10 and 100 μM.³⁷ In our C57BL/6 WT mouse colony we screened n = 40 independent healthy mice and describe the following formate levels in serum: average = 39.55 μM; range [min - max] = 9.93 μM - 141.5 μM (see Figure S4G). In Figure S4H: Serum formate levels in exercised





mice: We found that in our model exercise leads to a ~2.3 fold* increase of formate serum levels relative to sedentary mice (*calculation: average exercise 52.0 μM / average sedentary 22.8 μM; averages derived from Figure 3J). Serum formate levels of exercised-FMT recipient mice: We found that in our model exercised-FMT leads to a ~3.5 fold* increase of formate serum levels relative to sedentary-FMT mice; (*calculation: average exercised-FMT = 45.3 μM / average sedentary-FMT = 12.8 μM; averages derived from Figure S5C). Serum formate levels in formate treated mice: In Figure S4G we quantified the average increase in serum formate levels following a single oral gavage of formate at a dose of 200 mg/kg b.w. Using a total of 20 independent mice (4 groups of 5 mice each), we measured serum formate concentrations at multiple time points between 2 and 12 hours post-gavage. The average serum formate concentration was 72.7 µM. Notably, the 24-hour time point was excluded from this calculation, as formate levels had returned to baseline by that time. Our analysis revealed that formate gavage resulted in an approximately 1.84-fold* increase serum formate levels compared to healthy control mice (*calculation: 72.7 μM / 39.55 μM (= average baseline formate level)).

Enzyme-linked immunosorbent assay (ELISA) to measure folic acid

Cecal folic acid concentrations were diluted in PBS and quantified using a folic acid ELISA kit (Cell Biolabs, Inc., San Diego, CA, USA) as per the manufacturer's instructions. Absorbance was measured immediately after sample preparation at 450 nm using SpectraMax i3x Multi-Mode Microplate Reader (Molecular Devices, San Jose, CA, USA).

Recovery of WT E. coli and Δ pfl E. coli from SPF Mice

Following daily oral gavage with 1 x 10*9 CFU WT or Δpfl E. coli, intestinal contents of mice were collected and homogenized in sterile PBS. Intestinal content homogenate was serially diluted in sterile PBS and serial dilutions were spot-plated on LB agar supplemented with 100 μg/mL chloramphenicol to selectively recover the exogenously administered WT and Δpfl E. coli strains. CFU were calculated and normalized to weight of intestinal contents used. In Figures S5I and S5K: Cecum contents at EPA were prepared as described above and cultured on chloramphenicol treated LB agar plates to allow exclusive growth of exogenously administered WT and $\Delta pfl E. coli$ growth. In Figure S5I serum formate values were normalized to corresponding E. coli strain abundance recovered in cecum of treated mice.

Bioinformatic meta-analysis of melanoma microbiome samples of nine independent cohorts

Whole metagenomic shotgun sequencing data from stool samples of melanoma patients from the studies and cohorts described on the Table 1 below were downloaded and re-analyzed using the JAMS package (https://www.biorxiv.org/content/10.1101/2023.03. 03.531026v1) version 1.9.8 publicly available at https://github.com/johnmcculloch/JAMS_BW.

The paired FASTQ sequencing reads for each individual sample was put through the JAMSalpha pipeline. Briefly, reads are trimmed using Trimmomatic 0.36, 114 then aligned to the Homo sapiens genome using Bowtie2 v2.3.2115 to deplete host-associated reads. Unaligned reads are then assembled into contigs using MEGAHIT v1.2.9. 116 Contigs larger than 500bp are then classified taxonomically using Kraken2117 via a custom-built Kraken2 database built using the JAMSbuildk2db tool of the JAMS package, which in turn uses as input all draft and complete genomes of all bacteria, archaea, fungi, viruses, and protozoa available in NCBI GenBank in December 2022, plus the human and mouse genomes. This JAMS-compatible kraken2 database is available for download through the URL https://hpc.nih.gov/~mccullochja/JAMSdb202212.tar.gz.

Contigs were then annotated using Prokka v1.14.6118 yielding the predicted proteome for each metagenomic sample. The sequencing depth of each contig was computed by alignment of reads used for assembly back to contigs and number of bases covering each contig and each feature was tallied. Taxonomy was expressed as the last known taxon (LKT), being the taxonomically lowest unambiguous classification determined for each query sequence, using Kraken's confidence scoring threshold of 5e-06 (using the -confidence parameter). The relative abundance, expressed in parts-per-million (PPM) for each LKT within each sample was calculated by dividing the number of bp covering all contigs and pertaining to that LKT by the total number of non-host base pairs sequenced for that sample.

The JAMSalpha outputs for each individual sample was then paired with metadata (Table S4) and put through the JAMSbeta script of the JAMS package, yielding.

SummarizedExperiment objects (Martin Morgan, Valerie Obenchain, Jim Hester and Hervé Pagès (2021). SummarizedExperiment: SummarizedExperiment container. R package, version 1.24.0. https://bioconductor.org/packages/SummarizedExperiment) containing not only feature-by-sample counts, but also sparse matrices with information regarding the stratification of each functional feature into the number of bases contributed by individual LKTs for each given feature.

Ordination plots were made by reducing dimensionality with applying the t-distributed stochastic neighbor embedding (t-SNE) algorithm using the uwot package in R (https://github.com/jlmelville/uwot) and plotting with the ggplot2 library. Permanova values were obtained using the adonis function of the vegan package, with 10000 permutations and pairwise distances calculated using Bray-Curtis distance.

Boxplots were obtained using the plot_relabund_features (https://github.com/johnmcculloch/JAMS_BW/blob/master/R/plot_ relabund_features.R) function of the JAMS package on the ECNumber analysis space JAMS-compatible SummarizedExperiment object obtained through JAMSbeta. For each feature, with p-values being calculated using the Mann-Whitney-Wilcoxon U-test on PPM relative abundances for each feature in samples within each group. The total relative abundance of enzyme EC_2.3.1.54 in each sample within each immunotherapy response group was broken down into the relative abundance of each contributing LKT





for that sample for only that enzyme via the retrieve_features_by_taxa function (https://github.com/johnmcculloch/JAMS_BW/blob/ master/R/retrieve_features_by_taxa.R) which is called through the plot_relabund_features function. Base pair counts covering EC_2.3.1.54 within each LKT containing that enzyme were aggregated into family level and then plot using ggplot2, also via the plot relabund features function of JAMS.

Batch correction in order to reduce the effects of comparing different cohorts while preserving the clinical response signal was performed using ConQuR.88 ConQuR differs from traditional batch correction methods designed for gene expression data in that it does not assume continuous normally distributed outcomes and is more suited for the kind of count data found in microbiome studies. ConQuR was run on the microbiome data in this study by using the cohort as the batch variable, the Dallas cohort as the reference batch, and using the clinical response variable as a covariate in order to preserve this information. Batch correction was performed both on the taxonomic counts as well as the functional data derived from it.

Batch-corrected data using ConquR was analyzed using the JAMS package by exporting the raw (non-normalized) counts of each feature within each sample for each JAMS analysis space (LKT - taxonomy, ECNumber and Product) and batch correcting these matrices using ConquR. The batch corrected raw counts were then used to build an analogous batch-corrected JAMS-compatible SummarizedExperiment object for each analysis space, which was then used exactly as aforementioned with the JAMS plotting functions plot_Ordination to obtain PERMANOVA values and ordination plots. Common effects model: The sample size, mean and standard deviation per group per cohort was calculated in R. The common-effects model meta-analysis was calculated using Meta-Mar with Hedges' g (bias corrected standardized mean difference, using exact formulae). Test of heterogeneity p-value threshold was 0.05.

Metagenomic Sequencing of mouse cecum contents Bioinformatic workflow of gene-centric metagenomic analyses

Taxonomic profiling was performed via MetaPhlAn v.4.1.1¹¹⁹ with the CHOCOPhlAn v3.0.14 database. ¹²⁰ For functional profiling, we used HUMAnN3 v.3.9 pipeline 120 with MetaPhlAn v.4.1.1, Bowtie2 version 2.2.6, 115 DIAMOND v 2.0.15, 121 and MinPath v.1.5.122 The HUMAnN3 pipeline was performed with the default parameters.

Bioinformatic workflow of metagenome-assembled genomes (MAGs) assembly and genome-centric metagenomic analysis

We used automated metagenomics bioinformatics workflows implemented by the programs 'anvi-run-workflow' 123 in anvi'o. 124,125 We used 'iu-filer-quality-minoche' to process the short metagenomic reads, implemented in illumina-utils v2.11, 126 and removed low-quality reads according to the criteria outlined in Minoche et al. 127 We used MEGAHIT v1.2.9128 to co-assemble (2 experimental groups - Exercise and Sedentary) quality-filtered short reads into longer contiguous sequences (contigs). We then used the following strategies to process contigs: 'anvi-gen-contigs-database on contigs to compute k-mer frequencies, and identify open reading frames (ORFs) using Prodigal v2.6.3¹²⁹; 'anvi-run-hmms' to identify sets of bacterial¹³⁰ and archaeal¹³¹ single-copy core genes using HMMER v.3.2.1¹³²; 'anvi-run-ncbi-cogs' to annotate ORFs with functions from the NCBI's Clusters of Orthologous Groups (COGs), 133 and 'anvi-run-kegg-kofams' to annotate ORFs from KOfam HMM databases of KEGG orthologs. 134,135 We recruited metagenomic short reads to contigs using Bowtie2 v2.3.5,115 and converted the resulting SAM files to BAM files using samtools v1.9.136 We used 'anvi-cluster-contigs' to group contigs into initial bins using CONCOCT v1.1.0, 137 and used 'anvi-refine' to manually curate the bins based on tetranucleotide frequency and different coverage across the samples. We marked bins that were more than 70% complete and less than 10% redundant as MAG. We used the "detection metric" to assess the presence of MAGs in a given sample, and considered a MAG as detected in a metagenome if the detection value was > 0.25, which is an appropriate cutoff to eliminate false-positive signals in read recruitment results, for its genome.

Human stool fecal microbial transplant (FMT) into mice Preparation

De-identified stool samples were aliquoted on ice in an anaerobic chamber. After quantifying the absolute amount of formate within stool samples of the healthy subjects by mass spectrometry, we transplanted the 3 highest (> 0.0051 µg formate/mg feces) and 3 lowest (<0.0032 μg/mg feces) formate-producing human microbiomes into sedentary recipient mice. FMT suspension of each selected donor was transplanted into 5 recipient mice. Another group of mice received a self FMT, in which their own feces were collected and processed for FMT and delivered back to each mouse, to control for the potential immunogenicity of a cross-species FMT, as described in "fecal microbial transplantation (FMT)".

All recipient mice were treated with a broad-spectrum ABX cocktail for 7 days (see "administration of antibiotics, formate, TBHQ, and bacteria") followed by a 24h wash out period. Mice then received 3 doses of human FMT delivered by oral gavage with one rest day between each dose. FMTs consisted of 40 mg fecal material suspended in 200 µL PBS, prepared as described in "fecal microbial transplantation (FMT)".



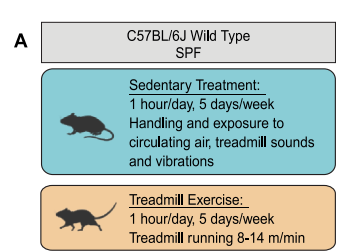


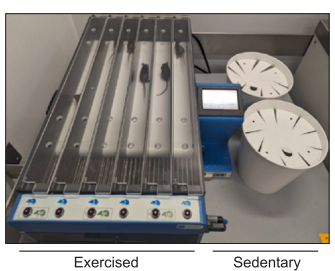
QUANTIFICATION AND STATISTICAL ANALYSIS

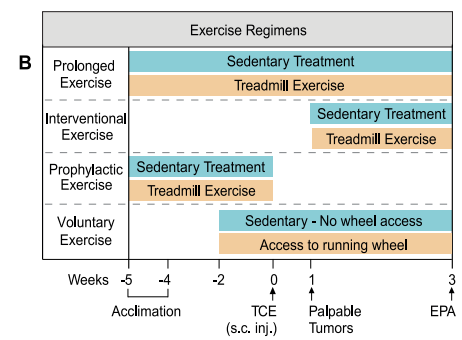
The majority of experiments were repeated at least two times to obtain data for indicated statistical analyses. Mice were allocated to experimental groups on the basis of their genotype and randomized within the given sex- and age-matched group. Given that our mice were inbred and matched for age and sex, we assumed similar variance between the different experimental groups. Statistically significant outliers were excluded from analysis. We did not perform a priori sample size estimation but always used as many mice per group as possible to minimize type I and type II errors. Except mass spectroscopical (LC-HRMS) analysis, investigators were not blinded during experiments and outcome assessment. All experimental and control animals were littermates and none were excluded from the analysis at the time of harvest. All quantitative data are presented as mean ± standard error of the mean (SEM), unless otherwise indicated. Data was analyzed using an unpaired two-tailed Student's t-test for single comparisons, a paired t-test for repeated measurements between independent samples, and one-way or 2-way ANOVA for multiple comparisons. ANOVA analysis was followed by a Sidak's post-hoc test. Data for repeated measures between individual samples was analyzed using a repeated measures (RM) one-way ANOVA, followed by a Sidak's post-hoc test. Survival data was analyzed by log-rank test. Correlations were calculated using the Spearman correlation. Figures and statistical analysis were generated using GraphPad Prism 10 (GraphPad Software). The statistical test used and p values are indicated in each figure legend. p values of < 0.05 were considered statistically significant. *p < 0.05, **p <0.01, ***p <0.001 and ****p <0.0001.



Supplemental figures







	V 77									
	Prole	Intervention	nal Ex	ercise Regimen	Prophylactic Exercise Regimen					
Stage of Regimen	Acclimation period	pre TCE	post TCE	Acclimation period	pre TCE	post TCE	Acclimation period	pre TCE	post TCE	
Length of Stage	1 week	4 weeks	Variable - 2-3 weeks	3 days	n/a	Variable - 2-3 weeks	1 week	4 weeks	n/a	
Frequency	1x / day, 5 consecutive days / week	1x / day, 5 consecutive days / week	1x / day, 5 consecutive days / week	1x / day, 3 consecutive days	n/a	1x / day, 5 consecutive days / week	1x / day, 5 consecutive days / week	1x / day, 5 consecutive days / week	n/a	
Duration / session	Day 1 & 2: 15 min; Day 3: 30 min; Day 4 & 5: 55 min	60 min	60 min	Day 1 & 2: 15 min; Day 3: 30 min		60 min	Day 1 & 2:15 min; Day 3: 30 min; Day 4 & 5: 55 min	60 min	n/a	
Average m ran / session	Day 1 & 2: 100m; Day 3: 200m; Day 4 & 5: 400m		450m	Day 1 & 2: 100m; Day 3: 200m	n/a	550m	Day 1 & 2: 100m; Day 3: 200m; Day 4 & 5: 400m	550m	n/a	
Average Speed (m/min)	7	9	7.5	7	n/a	9	7	9	n/a	
Elevation (degrees)	0°	0°	0°	0°	n/a	0°	0°	0°	n/a	

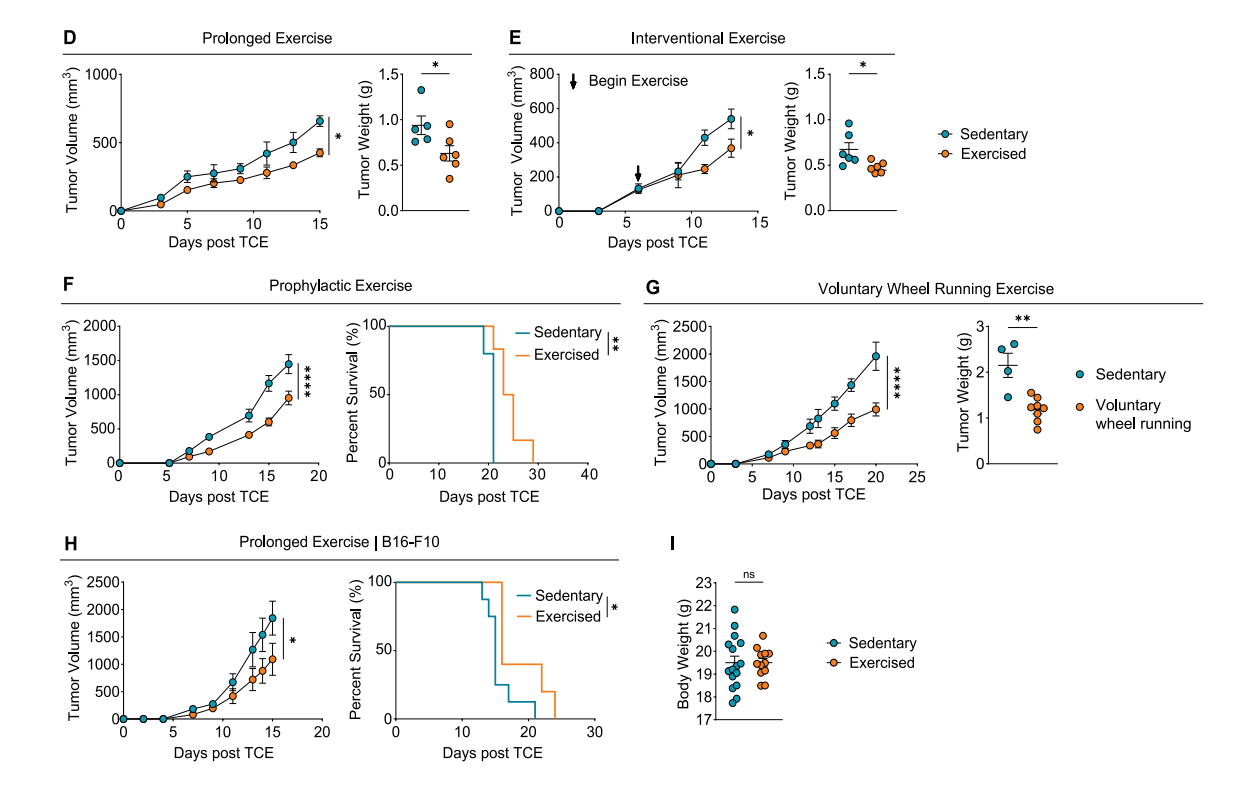






Figure S1. Prolonged, interventional, and prophylactic exercise restrains preclinical melanoma tumor growth, related to Figure 1

- (A–C) Exercise and sedentary treatment regimens description. (A) Exercise and sedentary treatment regimen overview and representative images. (B) Experimental timelines for prolonged, interventional, and prophylactic exercise modalities. (C) Exercise regimen details.
- (D) Wild-type (WT) mice underwent prolonged exercise or sedentary treatment and BRAF V600E tumor cell engraftment (TCE) as described in (B) (n = 5–6 mice/group). Tumor growth and weight are shown.
- (E) WT mice underwent interventional exercise or sedentary treatment and BRAF^{V600E} TCE as described in (B) (n = 6 mice/group). Tumor growth and weight are shown.
- (F) WT mice underwent prophylactic exercise or sedentary treatment and BRAF V600E TCE as described in (B) (n = 6-8 mice/group). Tumor growth and survival are shown.
- (G) Mice underwent voluntary wheel-running exercise or sedentary treatment as described in (B), including BRAF V600E TCE (n = 5-8 mice/group). Tumor growth and weight shown.
- (H) WT mice underwent prolonged exercise or sedentary treatment and B16-F10 TCE as described in (B) (n = 6-8 mice/group). Tumor growth and survival are shown.
- (I) WT mice received sedentary or exercise treatment for 5 weeks, after which body weight was recorded (n = 14–16 mice/group).
- (D–H) Represent mean \pm SEM analyzed by two-way ANOVA with Sidak's correction for multiple comparisons. (D, E, G, and I) Represent individual mice analyzed by unpaired t test. (F and H) Represent survival curves analyzed by log-rank test. Mean \pm SEM shown. *p < 0.05, **p < 0.01, *****p < 0.001; ns, not significant.



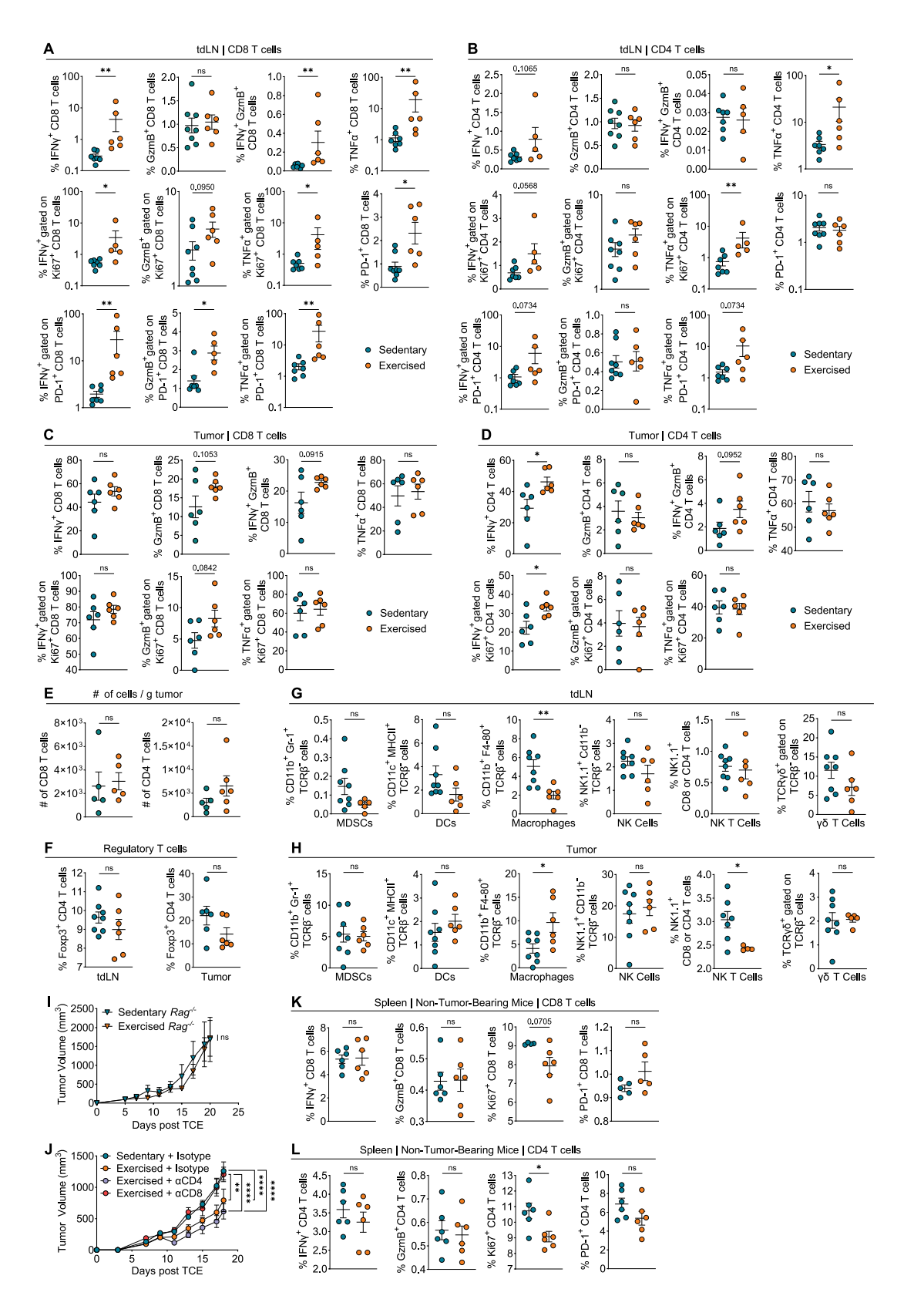






Figure S2. Exercise-induced tumor restraint requires adaptive immunity, specifically CD8 T cells, and induces minimal changes to T cell activation during homeostasis, related to Figure 1

(A–F) BRAF^{V600E} tumor-bearing WT mice underwent prolonged exercise or sedentary treatment. Tumor-draining lymph nodes (tdLNs) and tumors were harvested to detect CD8 and CD4 T cell effector function by flow cytometry at EPA (13 days post-TCE) (n = 6-8 mice/group). Frequencies of cytokines and surface markers present on tdLN CD8 T cells (A), tdLN CD4 T cells (B), tumor-infiltrating CD8 T cells (C), and tumor-infiltrating CD4 T cells (D). (E) Number of CD8 (left) or CD4 (right) T cells/g tumor. (F) Frequency of Foxp3+ regulatory T cells in tdLN (left) or tumor (right).

(G and H) BRAF^{V600E} tumor-bearing WT mice received interventional exercise or sedentary treatment. Tumors and tdLNs were collected at EPA (n = 6-8 mice/group). Frequencies of myeloid-derived suppressor cells (MDSCs), dendritic cells (DCs), macrophages, natural killer (NK) cells, NK T cells, and $\gamma\delta$ T cells present in the tdLN (G) and tumor (H) are shown.

(I) $Rag^{-/-}$ mice received prolonged exercise or sedentary treatment (n = 5 mice/group). Tumor growth shown.

(J) WT mice underwent prolonged sedentary or exercise treatment and received BRAF^{V600E} TCE. Once tumors were palpable, mice received CD4-depletion antibody, CD8-depletion antibody, or isotype control by i.p. injection once per week until EPA (n = 8–6 mice/group). Tumor growth shown.

(K and L) WT mice underwent 5 weeks of sedentary or exercise treatment, and splenic lymphocytes were isolated to assess activation in the presence of exercise but absence of tumor (n = 6 mice/group). Frequencies of splenic IFN γ^+ , GzmB $^+$, Ki67 $^+$, and PD-1 $^+$ CD8 (K) or CD4 (L) T cells shown.

(A–H, K, and L) Represent individual mice analyzed by unpaired t test. Mean \pm SEM shown. (I and J) Represent mean \pm SEM analyzed by two-way ANOVA with Sidak's correction for multiple comparisons. Mean \pm SEM shown. *p < 0.05, **p < 0.01, ****p < 0.001; ns, not significant.



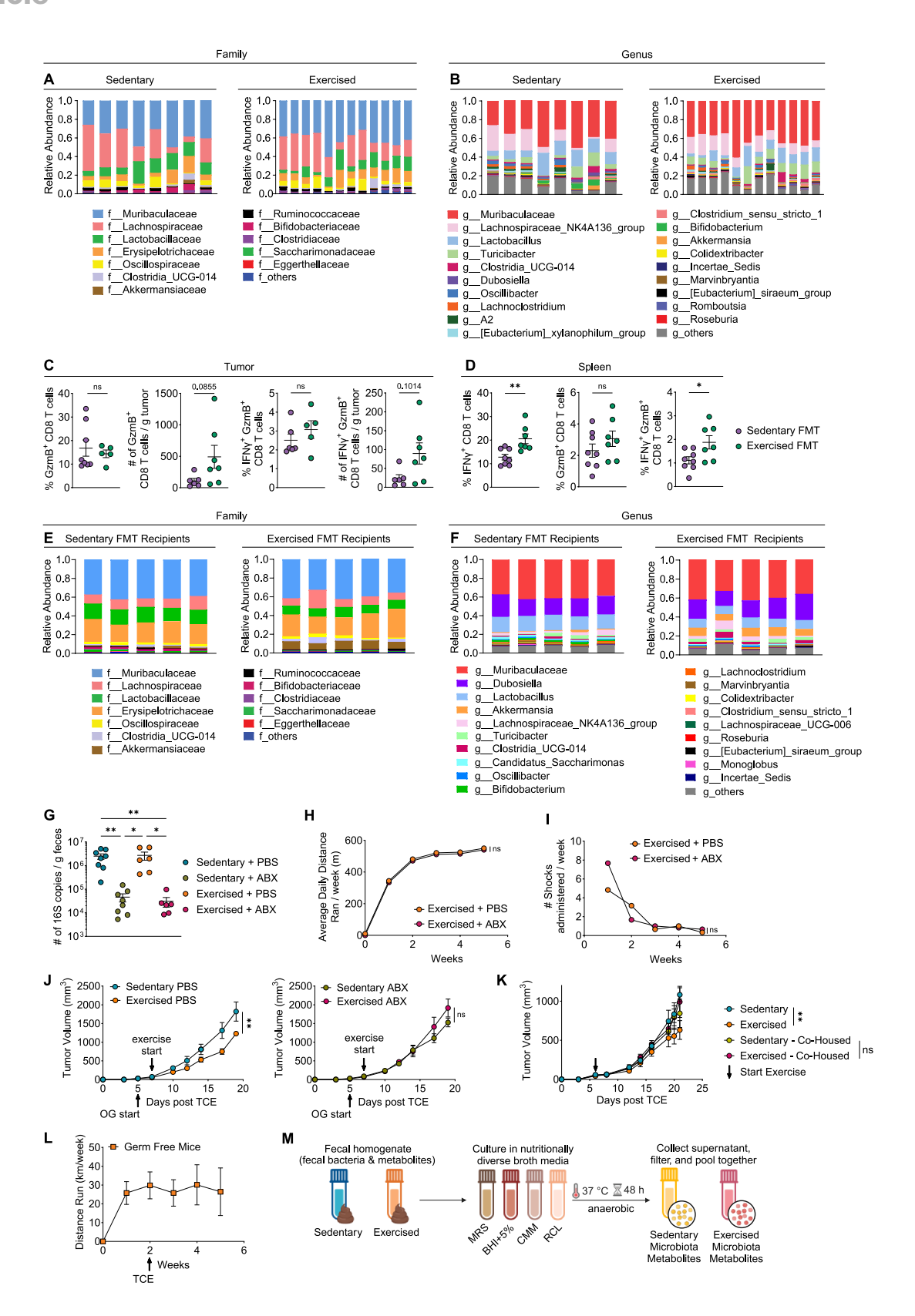






Figure S3. Exercise induces gut microbiome changes that enhance antitumor Tc1 immunity, related to Figures 1 and 2

(A and B) WT mice received exercise or sedentary treatment for 5 weeks, at which point feces were collected and taxonomy was assessed by 16S seq (n = 14–16 mice/group). Bacterial ASVs classified with Silva 138.1 database collapsed to the family (A) or genus (B) level shown.

(C–F) WT mice received an exercised fecal microbiota transplant (EX-FMT) or sedentary fecal microbiota transplant (SED-FMT) followed by BRAF V600E TCE as described in Figure 1F (n = 7-8 mice/group). (C) Frequency (left) and cells/g tumor (right) of cytokine-producing tumor-infiltrating CD8 T cells shown. (D) Frequency of splenic effector-cytokine-secreting CD8 T cells shown. Cecum contents were collected at EPA for 16S seq and ASVs at the family (E) or genus (F) level shown.

(G) Fecal 16S abundance of mice shown in Figure 1K (n = 6-8 mice/group).

(H and I) Average daily distance ran (H) and electric shocks received to incentivize running (I) by exercised mice shown in Figure 1K (n = 6–8 mice/group).

(J) WT mice received BRAF^{V600E} subcutaneous (s.c.) tumor engraftment and underwent interventional exercise regimen or sedentary treatment alongside oral gavage with antibiotics or vehicle (PBS) as indicated (*n* = 6–8 mice/group). Tumor growth shown.

(K) WT mice received BRAF V600E s.c. tumor engraftment and underwent interventional exercise regimen or sedentary treatment. Mice were co-housed either within matched or mismatched groups (n = 4-6 mice/group). Tumor growth shown.

(L) Distance run every week by GF mice shown in Figure 1M (n = 8 mice/group).

(M) Schematic showing preparation of cultured microbiota metabolites.

FMT solution derived from sedentary or exercised donor mouse feces was aliquoted into four different broth cultures. Broth cultures were grown anaerobically (37°C) for 48 h. Bacterial cultures were then pelleted by centrifugation, and supernatant was removed from each culture. Supernatant was vacuum filtered $(0.22~\mu\text{m})$ to remove any remaining bacteria or debris. Exercised culture supernatants were pooled together, and sedentary culture supernatants were pooled. (C and D) Represent individual mice analyzed by unpaired t test. Mean \pm SEM shown. (G) Represents individual mice analyzed by one-way ANOVA with multiple comparisons. Mean \pm SEM shown. (H–K) Represent mean \pm SEM analyzed by two-way ANOVA with Sidak's correction for multiple comparisons. Mean \pm SEM shown. *p < 0.05, **p < 0.01; ns, not significant.



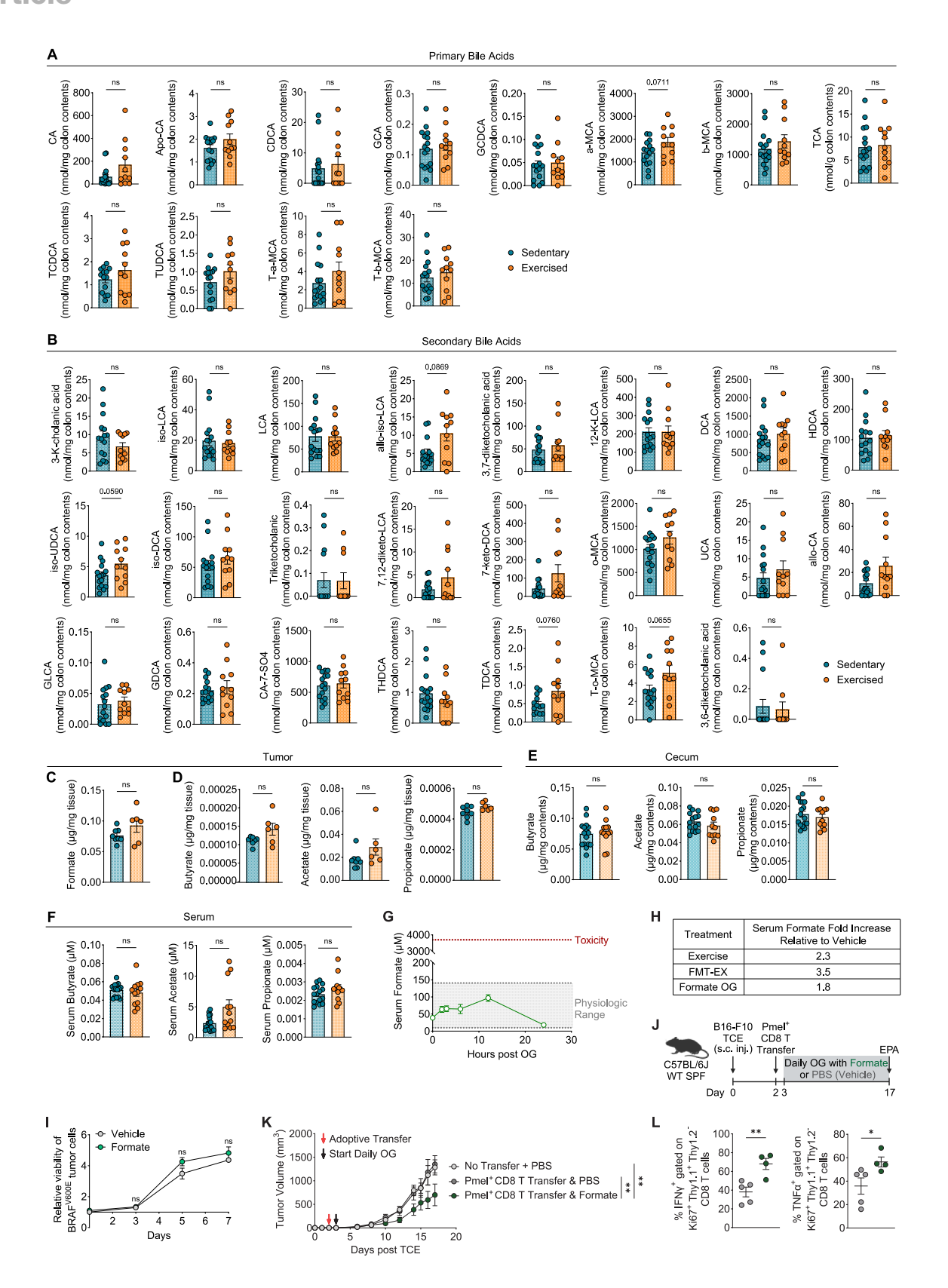






Figure S4. Exercise does not induce significant changes to bile acid abundance or SCFAs butyrate, acetate, and propionate, related to Figures 3 and 4

(A and B) WT mice underwent prolonged exercise or sedentary treatment and received BRAF^{V600E} TCE. Colon contents were collected at EPA, and the absolute abundance of bile acids was quantified (*n* = 12–16 mice/group). Absolute abundance of primary bile acids (A) and secondary bile acids (B) shown as nmol/mg colon contents. Definitions of bile acid abbreviations are shown in Table S1.

(C–F) WT mice underwent prolonged exercise or sedentary treatment, including BRAF V600E TCE. Tumors, serum, and intestinal contents were harvested at EPA, and SCFAs were quantified by mass spectrometry (n = 6-16 mice/group). (C and D) Absolute abundance of formate (C) and acetate, propionate, and butyrate (D) in tumor. (E and F) Absolute abundance of acetate, propionate, and butyrate in cecum (E) and serum (F) is shown.

- (G) Serum formate concentration over time following 200 mg formate/kg body weight oral gavage (OG).
- (H) Serum formate fold increase relative to vehicle treatment for multiple experimental treatments.
- (I) Relative viability of BRAF^{V600E} tumor cells exposed to formate *in vitro*.

(J-L) 2 days post-TCE of B16-F10 melanoma, WT mice received an adoptive transfer of tumor antigen-specific pmel⁺ CD8 T cells or a vehicle control. 1 day later, mice began receiving daily OG of formate or vehicle (PBS) until EPA (n = 5 mice/group). (J) Experimental outline. (K) Tumor growth. (L) Frequency of tumor-infiltrating proliferating Ki67⁺ CD8 T cells that produce IFN γ (left) or TNF- α (right).

(A–F and L) Represent individual mice analyzed by unpaired t test. Mean \pm SEM shown. (I and K) Represent mean \pm SEM analyzed by two-way ANOVA with Sidak's correction for multiple comparisons. *p < 0.05, **p < 0.01; ns, not significant.



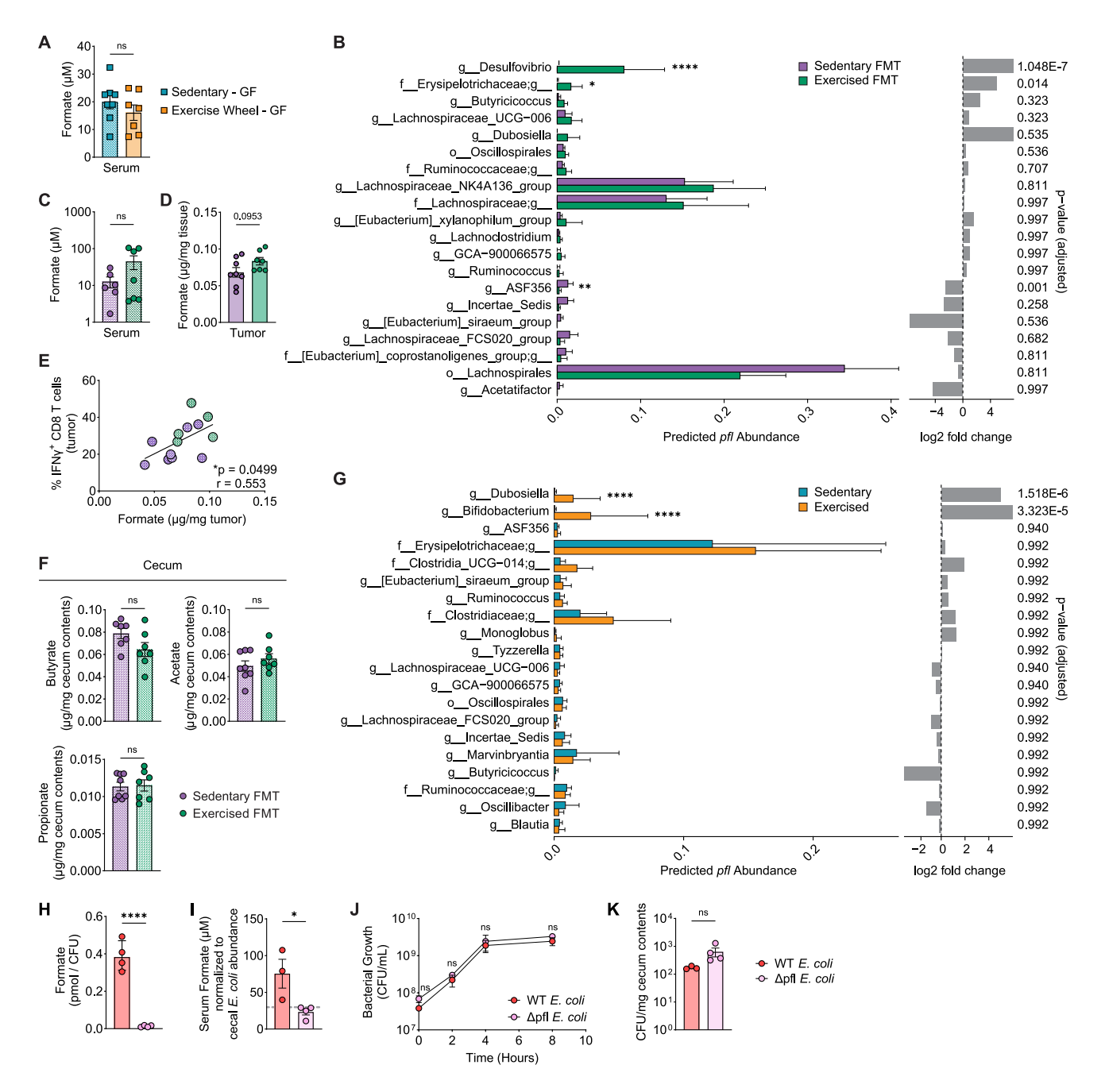


Figure S5. Microbiota-derived formate is required for tumor restraint, and Δpfl *E. coli* displays no growth defects *in vivo* or *in vitro*, related to Figure 5

(A) GF WT mice received voluntary running wheel regimen, including BRAF V600E s.c. tumor injection (n = 8 mice/group). Absolute abundance of formate in serum at EPA is shown.

(B–F) WT mice received exercised or sedentary FMT and BRAF V600E TCE. At EPA, intestinal contents, serum, and tumor were collected for SCFAs quantification and 16S seq (n=8 mice/group). (B) Stratified results from PICRUSt2 reveal the taxa contributing to predicted pfl expression within each group. Genus raw counts were normalized to total pfl counts per FMT group (predicted pfl abundance), and LDA calculated Log₂ fold change and adjusted ppl values between groups. (C and D) Absolute abundance of formate in serum (C) and tumor (D). (E) Spearman correlation between intratumoral Tc1 frequency and tumor formate. (F) Absolute abundance of butyrate, acetate, and propionate in cecum contents.

(G) Stratified results from PICRUSt2 reveal the taxa contributing to predicted pfl expression within each group. Genus raw counts were normalized to total pfl counts per FMT group (predicted pfl abundance), and LDA calculated Log₂ fold change and adjusted p values between groups.

(H) Absolute abundance of formate in culture supernatants of WT and Δpfl E. coli detected by mass spectrometry.





(I) WT mice were colonized with a single OG of WT or Δ pfl *E. coli*. 12 h later, serum was collected, and the absolute abundance of formate was quantified by mass spectrometry. Cecum contents were also collected and used to quantify colony-forming unit (CFU) of WT and Δ pfl *E. coli* on selective antibiotics agar. Serum formate normalized to CFU of WT and Δ pfl *E. coli* shown (n = 3-4 mice/group).

⁽J) Bacterial growth in vitro shown.

⁽K) CFU of WT and Δ pfl *E. coli* recovered from colonized mice shown in Figure 5K (n = 3-4 mice/group).



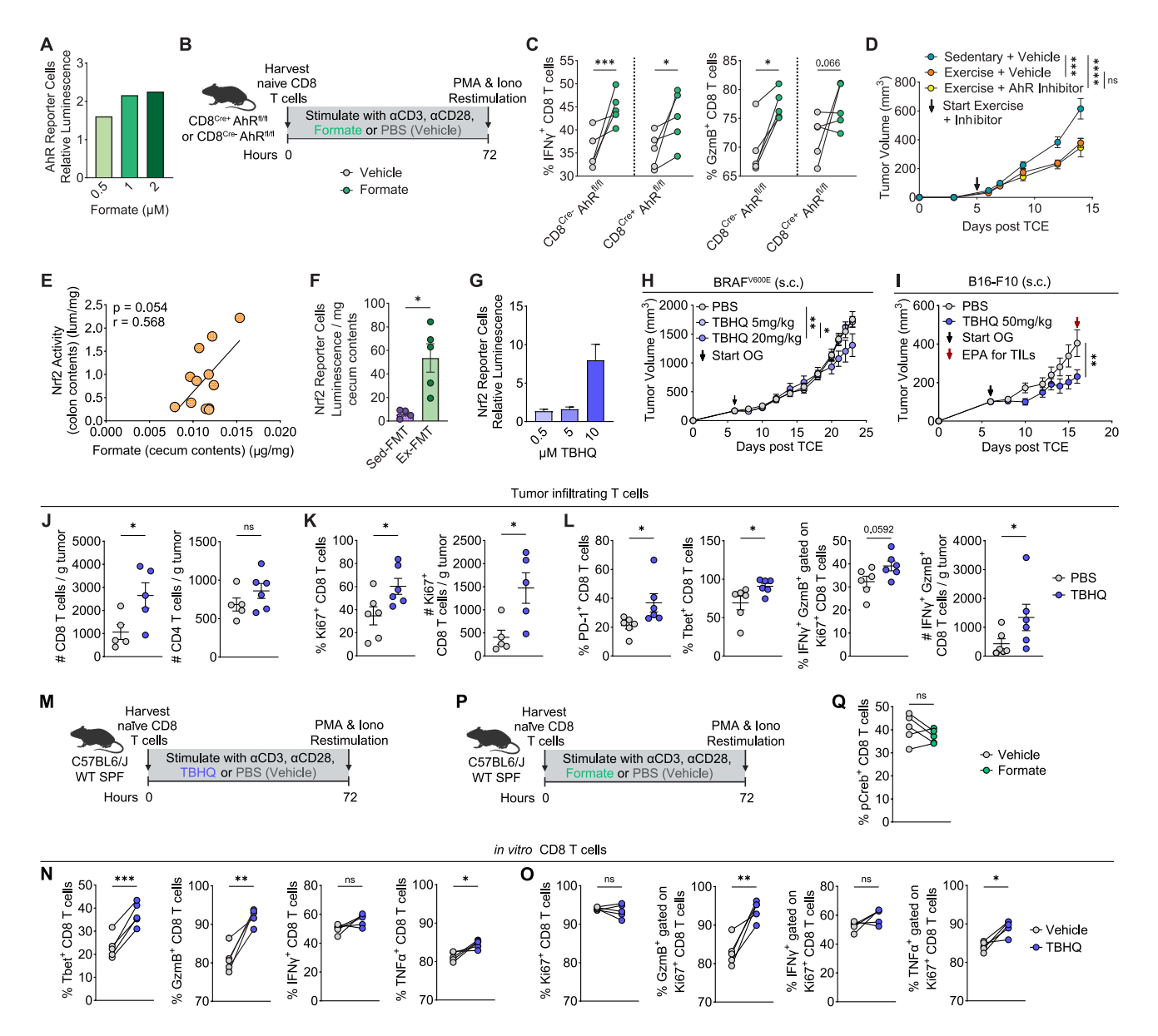


Figure S6. Formate enhances Tc1 immunity both *in vitro* and *in vivo* through Nrf2 signaling, independent of the AhR pathway; Nrf2 agonist TBHQ promotes Tc1 immunity, related to Figure 6

(A) AhR-induced luminescence was measured using an AhR reporter cell line cultured with multiple concentrations of formate for 24 h. Luminescence is shown as average fold change relative to vehicle control.

(B and C) Naive CD8 T cells were isolated from peripheral lymph nodes and spleen of CD8 Cre $^+$ $AhR^{fl/fl}$ or CD8 Cre $^ AhR^{fl/fl}$ mice. CD8 T cells were then cultured in the presence of α CD3, α CD28, and formate (2 mM) or vehicle control (PBS). (B) Experimental timeline. (C) Frequency of IFN γ^+ and GzmB $^+$ CD8 T cells shown. (D) BRAF^{V600E} tumor-bearing WT mice underwent interventional exercise or sedentary treatment. Concurrently, mice received AhR inhibitor or vehicle by i.p. injection 5 days/week beginning when tumors were palpable (\sim 150 mm 3) and continuing until EPA (n = 6–8 mice/group). Tumor growth shown.

(E) WT mice underwent prolonged exercise or sedentary treatment and BRAF^{V600E} tumor engraftment. At EPA, intestinal contents were collected and tested for absolute quantification of formate by mass spectrometry and Nrf2 stimulatory activity by luminescent reporter cells. Spearman correlation shown.

(F and G) Nrf2-induced luminescence measured using an Nrf2 reporter cell line cultured with cecum contents of SED- and EX-FMT recipients (F) and tert-butylhydroguinone (TBHQ) (G).

(H–L) WT mice were engrafted with BRAF^{V600E} (H) or B16-F10 (I) tumors and received OG with TBHQ as indicated (*n* = 5 mice/group). Tumor growth shown. (J–L) Tumors of mice in (I) were assessed for CD8 T cell effector function by flow cytometry. Absolute number of CD8 and CD4 T cells/g tumor (J), frequency and absolute number of proliferating Ki67⁺ cells/g tumor (K), and frequency and count of activated CD8 T cells in tumor shown (L).

(M–O) Naive CD8 T cells were isolated from spleen and peripheral lymph nodes of WT mice and stimulated with αCD3, αCD28, and TBHQ (1 nM) or vehicle for 72 h. (M) Experimental outline. (N and O) Frequency of Tbet⁺ and effector cytokine-producing CD8 T cells (N) and proliferating Ki67⁺ effector cytokine-producing CD8 T cells (O).



⁽C, N, O, and Q) Represent individual samples per group analyzed by paired t test. (D, H, and I) Represent mean \pm SEM analyzed by two-way ANOVA with Sidak's correction for multiple comparisons. (E) Represents a Spearman correlation analysis in which each dot represents a single mouse. (F and J–L) Represent individual mice analyzed by unpaired t test. Mean \pm SEM shown. *p < 0.05, **p < 0.01, ***p < 0.001, ****p < 0.001; ns, not significant.





	Experimental			Control		Std. Mean Difference		•	
Study	Mean SD To		Total	Mean	SD	Total	Weight	IV, Fixed, 95% CI	
Barcelona	8.61	0.1248	5	8.42	0.2335	6	4.1%	0.90 [-0.37; 2.18]	
Chicago	8.59	0.2264	15	8.57	0.2095	24	15.8%	0.07 [-0.57; 0.72]	
Dallas	8.92	0.1673	6	8.58	0.3383	7	4.5%	1.16 [-0.06; 2.37]	Heterogeneity:
Houston	8.42	0.2773	14	8.44	0.4612	11	10.6%	-0.04 [-0.83; 0.75]	$Tau^2 = 0.0228$;
Leeds	8.91	0.1590	10	8.88	0.4185	9	8.1%	0.11 [-0.79; 1.01]	$Chi^2 = 10.25$, $df = 8 (P = 0.25)$
Pittsburgh	8.90	0.3165	37	8.75	0.2885	24	24.2%	0.50 [-0.02; 1.02]	$I^2 = 22\%$
New_York	8.88	0.2157	7	8.70	0.0909	7	5.0%	1.06 [-0.08; 2.20]	
PRIMM-NL	8.77	0.3550	25	8.83	0.5194	17	17.3%	-0.13 [-0.75; 0.48]	
PRIMM-UK	8.85	0.1937	14	8.92	0.2559	11	10.4%	-0.32 [-1.11; 0.48]	
Total (95% CI)			133			116	100.0%	0.22 [-0.03: 0.48]	

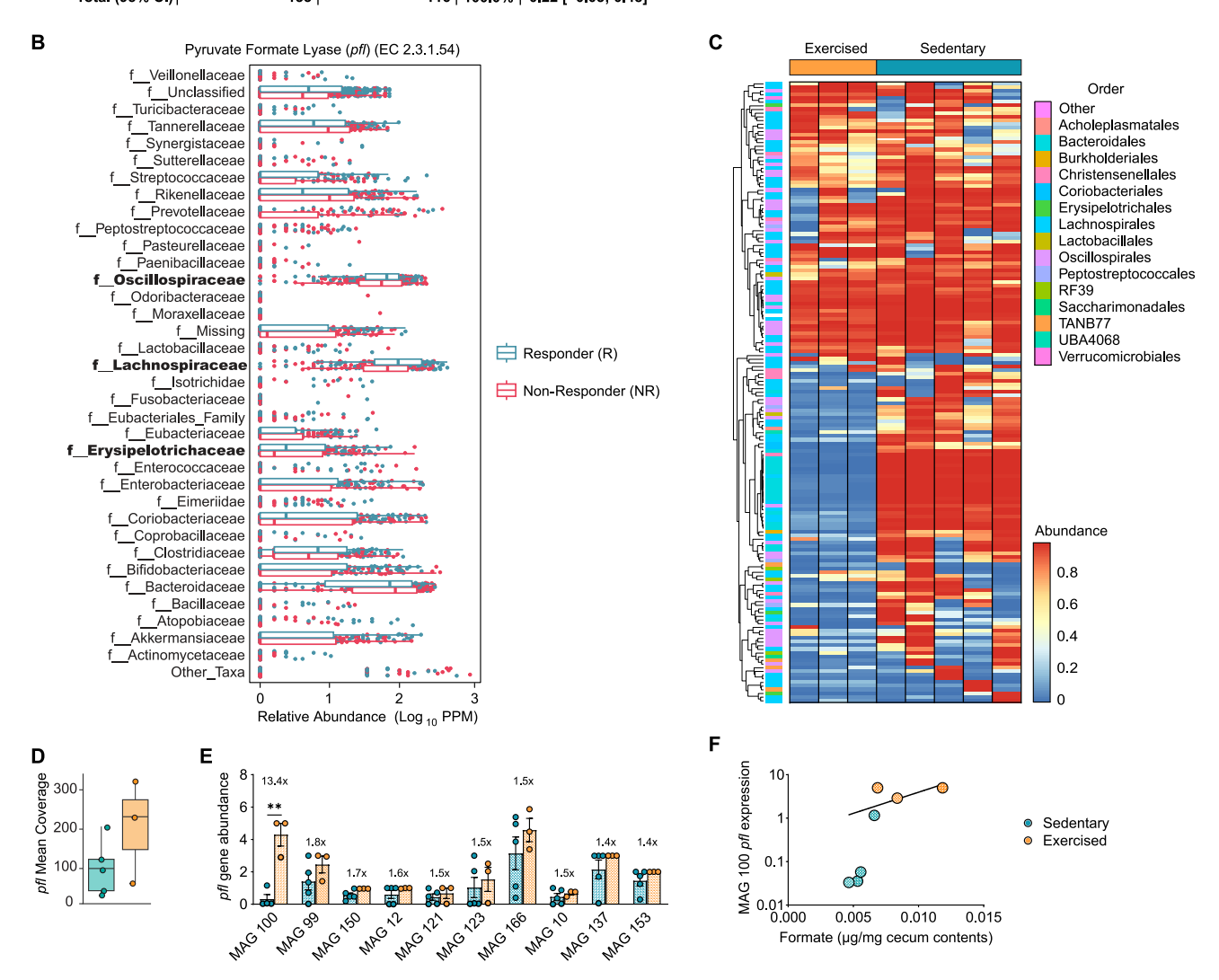


Figure S7. High-formate-producing gut microbiota taxa in mice mirror formate-producing taxa in melanoma patients, related to Figure 7 (A and B) Meta-analysis of microbial sequencing data from stool samples of nine published independent cohorts of anti-PD-1-treated patients. (A) Additional information regarding common effects model shown in forest plot Figure 7B (B) EC_2.3.1.54 (pfl) gene number present by each bacterial family, which bears 512 genes for this enzyme in non-responders and responders to ICI therapy.

(C–E) Metagenomic analyses from cecum samples at EPA of mice that underwent voluntary exercise or sedentary treatment, including BRAF V600E tumor engraftment (n = 3–5 mice/group). (C) Heatmap showing metagenomic taxonomic changes at the order level. Rows representing metagenome-assembled genomes (MAGs) clustered according to their detection level in the samples. Scale bar denotes detection level. (D) Pfl expression, mean coverage level in the metagenomes, in sedentary and exercised groups. (E) Pfl gene abundance in sedentary and exercised conditions of MAGs is shown. Fold change of pfl expression by each MAG under exercised treatment relative to sedentary treatment shown above.

(F) Spearman correlation between MAG 100 pfl expression and formate in cecum contents shown.

(D and E) Represent unpaired t tests in which each dot represents an individual mouse. (F) Represents a Spearman correlation in which each dot represents an individual mouse. *p < 0.05, **p < 0.01; ns, not significant.